Simulating High Flux Solar Radiation and Assessing its Influence on a Sooty Flame

Xue Dong

BEng

Thesis submitted for the degree of Doctor of Philosophy

School of Chemical Engineering

Faculty of Engineering, Computer & Mathematical Sciences

The University of Adelaide, Australia

September 2015

<u>Table of Contents</u>

ABSTRACT

Integrating concentrated solar thermal energy into fossil-fuels for the production of power/clean fuels is receiving growing attention as the combination of the two energy sources can provide lower emissions of carbon and other pollutants, lower cost, and continuous supply. Various types of hybrid concepts have been proposed. However, all of these concepts employ stand-alone solar receivers and standalone combustors. The University of Adelaide has developed an alternative approach with which to fully integrate a combustor into a solar cavity receiver. This offers the potential for significant savings from reduced infrastructure investment and reduced start-up and shut-down losses. In addition, this hybrid also results in the direct interaction between concentrated solar radiation and a flame, which is theoretically known to be coupled. However, the influence of concentrated solar radiation (CSR) on the flame has not been experimentally investigated. Hence this thesis aims at filling this gap.

High flux solar simulators, comprising an array of high-intensity-discharge lamps coupled with elliptical reflectors, have been widely employed to study concentrated solar thermal energy systems. The use of electrical solar simulators holds the advantage over natural solar radiation in providing repeatable performance without the variability of the solar resource. Reliable models which predict the heat flux generated by a solar simulator are desirable because they enable efficient and systematic optimization of the system to meet the required trade-off between cost and performance. To this end, a concentric multilayer model of the light source is developed in this study to accurately predict the spatial distribution of the heat flux at the focus using a commercial Monte Carlo ray-tracing code. These simulations were validated with measurements of both the radiant intensity of the light source and the distribution of the concentrated heat flux. Further to that, on the experimentally validated ray tracing model, the geometry and surface reflectance of the additional concentrators were also assessed of two high flux solar simulators: one employs a single lamp, the other uses a seven-lamp array. In addition, the time-resolved spectra of solar simulators employing a metal halide and a xenon arc lamp are also measured, which provides the first

experimental results of this kind that acquired from the same spectrometer to allow for direct comparison.

This thesis also reports the first set of measurements of the influence of concentrated solar radiation on the soot volume fraction and temperature in a laminar sooty flame. Detailed laser diagnostics was performed on a laminar sooty flame with and without the irradiance of CSR, because laser diagnostics are demonstrated to hold the advantages of being non-intrusive, lower interferences and of being applicable to environments with high flux radiation. The current measurement using laser induced incandescence shows that the soot volume within the laminar flame was increased by 55% by CSR. In addition, the measurement of temperature using two-line atomic fluorescence shows that the flame temperature was increased by around 8% under CSR.

In addition to the detailed laser diagnostics, an assessment of the influence of soot volume fraction on the global performance of the flames was also performed through a systematic study of flames using fuels of different soot propensities, which is achieved by blending hydrogen into hydrocarbon fuels, with hydrogen volume fraction ranging from 0 to 100%. Results show that flames with higher soot volume fraction have higher radiant fraction and lower NOx emissions.

The principle contribution of the thesis is that the first measurement of the influence of concentrated solar radiation on the soot volume fraction and temperature of a flame was performed, which pushed forward the existing understanding of the interaction between broadband solar radiation and combustion. Its second major contribution is establishing an experimentally validated ray-tracing model that accurately predicts the concentrated heat flux from the solar simulator, and on this model, new design and optimization of solar simulators were performed. While this ray-tracing model is developed for metal halide lamps, the methodology is applicable more generally to solar simulators employing other types of discharge arc lamps.

DECLARATION

I certify that this work contains no material which has been accepted for the award of any other degree or diploma in my name, in any university or other tertiary institution and, to the best of my knowledge and belief, contains no material previously published or written by another person, except where due reference has been made in the text. In addition, I certify that no part of this work will, in the future, be used in a submission in my name, for any other degree or diploma in any university or other tertiary institution without the prior approval of the University of Adelaide and where applicable, any partner institution responsible for the joint award of this degree.

I give consent to this copy of my thesis when deposited in the University Library, being made available for loan and photocopying, subject to the provisions of the Copyright Act 1968. The author acknowledges that copyright of published works contained within this thesis resides with the copyright holder(s) of those works. I also give permission for the digital version of my thesis to be made available on the web, via the University's digital research repository, the Library Search and also through web search engines, unless permission has been granted by the University to restrict access for a period of time

<div style="text-align: right;">16/01/2016</div>

Xue Dong   DATE

ACKNOWLEDGEMENT

<u>PREFACE</u>

This thesis is submitted as portfolio of publications according to the "Specifications for Thesis 2014" of the University of Adelaide. The journals of which the papers were published or submitted are highly ranked journals in the research field of Chemical Engineering. Data on the impact factors of the journals are listed below:

Journal Title	5-year Impact Factor
Combustion and Flame	3.557
Solar Energy	4.452
Journal of Solar Energy Engineering	1.934

The main body of work contained in this thesis consists of the following five journal papers:

1) **X. Dong;** G. J. Nathan; Z. W. Sun; D. H. Gu; P. J. Ashman, "Concentric multilayer model of the arc in high intensity discharge lamps for solar simulators with experimental validation", Solar Energy, (2015), acceptted.

2) **X. Dong;** Z. W. Sun; G. J. Nathan; P. J. Ashman; D. H. Gu, "Time-resolved spectra of solar simulators employing metal halide and xenon arc lamps", Solar Energy 115 (2015) 613-620.

3) **X. Dong;** G. J. Nathan; Z. Sun; D. Gu; P. J. Ashman; Z. Alwahabi; B. Dally, "The influence of high flux broadband irradiation on soot concentration and temperature of a sooty flame", manusctript under prepartion for Combustion and Flame.

4) **X. Dong;** G. J. Nathan; S. Mahmoud; P. J. Ashman; D. Gu; B. B. Dally, "Global characteritics of non-premixed jet flames of hydrogen-hydrocarbon blended fuels", Combustion and Flame 162 (4) (2015) 1326-1335.

5) **X. Dong;** G. J. Nathan; Z. W. Sun; P. J. Ashman; D. H. Gu, "Secondary concentrators to achieve high flux radiation with methal halide solar simulators", Journal of Solar Energy Engineering, (2015), submitted.

Some additional aspects of this work were published in peer-reviewed conference papers. These are included as appendices.

A) **X. Dong**, Ashman, P.J., Nathan. G.J. "A high-flux solar simulator system for investigating the influence of concentrated solar radiation on turbulent reacting flows", Proceedings of Solar 2012, Australian Solar Council, Melbourne, 2012.

B) **X. Dong**; G. J. Nathan; Z. Sun; D. Gu; P. J. Ashman; Z. Alwahabi; B. Dally, "Influence of simulated solar radiation on the soot volume fraction in laminar sooty flames ", Proceedings of the10th Asia-Pacific Conference on Combustion, Beijing, China, 2015.

C) **X. Dong**; P. Ashman; G. Nathan "Global characteristics of hydrogen-hydrocarbon blended fuels turbulent diffusion flames", Proceedings of the Australian Combustion Symposium, Novermber 6-8, 2013, Western Australia.

CHAPTER 1

INTRODUCTION

1.1 Background

Combustion of fossil fuels provides approximately 80% of world energy consumption and is expected to still be a major energy source (around 75 percent) by 2035 [1]. At the same time, increasing effort on the mitigation of CO_2 emission will drive the development of techniques using renewables, which is expected to improve the share of renewable energy to 14.5% of the total energy market by 2040 [2]. In the renewable sector, the solar energy has the biggest share of 45%, with 24% for solar photovoltaics (PV) and 21% for solar thermal energy, respectively [3]. Comparing the two types of solar utilization, photovoltaics and solar thermal energy, the former has the advantage of being flexible in scale and initial cost, while the latter has more potential to be the dominant source of sustainable energy in the long term, due to its relatively easier storage method for large-scale production [4]. However the capital and operating costs for solar thermal utilization are still much higher than that of fossil fuels, which is a critical factor that restricts the use of solar thermal energy [5].

To this end, hybrid systems were proposed. In a hybrid system, the concentrated solar thermal energy is integrated into existing facilities using fossil fuels. Such technologies are receiving growing attention as the combination of the two energy sources can provide lower emissions of carbon and other pollutants, lower cost, and continuous supply [6, 7]. Various types of hybrid concepts have been assessed, e.g. preheating the feed water with the low grade solar energy [8], regenerating CO_2 solvents for the carbon capture and storage process [9], preheating the combustion air in a Brayton cycle [10-12], and combining oxy-fuel combustion with solar thermal in a power cycle [13]. However, all of these concepts employ stand-alone solar receivers and stand-alone combustors. The economic benefit of employing shared infrastructure e.g., condenser and turbine, was first identified by Kolb [14]. Further to that, Mehos et al. [15] proposed one approach with which to better integrate these systems by mounting a combustor to the back of a solar

receiver. More recently, Nathan *et al.* [7, 16, 17] have been developing an alternative approach with which to fully integrate a combustor into a solar cavity receiver into a single device. This offers the potential for significant savings from reduced infrastructure investment [7] and reduced start-up and shut-down losses [7]. In addition, this hybrid also results in the direct interaction between concentrated solar radiation and a flame, which is theoretically known to be coupled, although relative strength of these interactions depend on the spectral characteristics of the fuel and oxidant [18].

While the experimental investigation of solar-combustion hybridizing dates back to at least the 18th century, when Antoine Lavoisier studied combustion and ignition processes under concentrated solar irradiation obtained in his solar furnace consisting of two concentric lenses [19], no detailed diagnostics have been performed of the influence of concentrated solar radiation on combustion prior to Medwell *et al.'s* [20] work. They demonstrated that CO_2 laser radiation at 10.6 μm with a fluence of 4 MW/m^2 can approximately double the peak concentration of soot in an ethylene flame, and translate the soot layer towards the oxidizing side of the flame [20]. However, the previous investigation was undertaken with a single excitation wavelength on a small area of the flame (5mm in diameter), while the CSR is broadband and can irradiate the whole flame in practical solar receiver/combustors. Therefore, the influence of broadband radiation of relevance to CSR on the soot volume fraction of the whole flame is yet to be studied.

For the experimental work to be undertaken, high flux solar simulators, comprising an array of high-intensity-discharge lamps coupled with elliptical reflectors, have been widely employed to study concentrated solar thermal energy systems. The design of these simulators has continued to evolve with the ongoing assessments of the trade-offs between spectrum, safety, cost and concentration ratio. Reliable models of the heat flux from a solar simulator are desirable because they enable efficient and systematic optimization of the system to meet the required trade-off between cost and performance, especially for solar simulators consisting of multiple lamps.

This, in turn, requires not only a model that accurately simulates the light source, but also sufficient experimental validation of the heat flux calculated with the ray tracing model. Furthermore, electrical solar simulators suffer from the disadvantages that their spectra differ somewhat from that of the real solar resource. Nevertheless, while this trend is known, no detailed assessment of their spectral differences has been reported previously.

The principle objective of this thesis is therefore to improve the understanding of the influence of the concentrated Solar Radiation (CSR) on combustion. These understandings are necessary for collecting the thermal energy from the solar and combustion sources in a single device, in contrast to established approaches that collect them from separate components. Another objective of this thesis is to develop a ray tracing model that accurately predicts the concentrated heat flux generated by the solar simulator, thus allowing the design and optimization of the solar simulators to be achieved in an efficient and cost-effective way.

1.2 Scope and structure of thesis

Chapter 2 provides a brief and critical review of the design of a high flux solar simulator and the influence of high flux solar radiation on combustion. The emphasis of this chapter is on the performance of solar simulators both on heat flux distribution and on the spectral property, together with the influence of high flux radiation of different wavebands on the species in a flame. Additionally, the global performances of turbulent diffusion flames of different soot propensity using hydrogen-hydrocarbon blended fuels are also reviewed.

Chapter 3 forms the framework for both the experimental setup and modelling work of this thesis. This paper presents a concentric multilayer model of the light source of the solar simulator that is developed to accurately predict the spatial distribution of the heat flux at the focus using a commercial Monte Carlo ray-tracing. These simulations were validated with measurements of both the radiant intensity of the light source and the distribution of the concentrated heat flux.

Chapter 4 reports the time-resolved spectra of the irradiation emitted from the high flux solar simulators employing the two types of high-intensity discharge arc lamps that are commonly used in solar simulators, i.e. metal halide and xenon arc lamps. In addition, the time-averaged spectra of these two types of lamps are also compared with that of the sun, which provides the first experimental results of this kind that acquired from the same spectrometer to allow for direct comparison.

Chapter 5 reports the first set of measurements of the influence of concentrated solar radiation on the soot volume fraction and temperature in a laminar sooty flame. Laser diagnostics are demonstrated to hold the advantages of being non-intrusive, lower interferences and of being applicable to environments with high flux radiation. The current measurement of soot volume fraction using laser induced incandescence shows that the soot volume within the laminar flame was increased by 55% by CSR. In addition, the measurement of temperature using two-line atomic fluorescence shows that the flame temperature was increased by around 50K under CSR.

Chapter 6 reports the global characteristics of flames of different soot propensities. This is achieved by blending hydrogen into hydrocarbon fuels to assess the influence, with hydrogen volume fraction ranging from 0 to 100%. Measurements were performed of flame dimensions, radiant fraction, and emission indices of NO_x and CO.

Chapter 7 is the follow-up work described in Chapter 3, this work adds secondary and tertiary conical concentrators to the solar simulator system to increase the concentration ratio. The geometry and surface reflectance of the additional concentrators was assessed of two high flux solar simulators: one employs a single lamp, the other uses a seven-lamp array.

Chapter 8 presents conclusions from the body of the work along with recommendations for future work in this area of research.

The Appendices provide peer-reviewed conference papers that are relevant to this study. Appendix A is a precursor of the journal publications on the design of high flux solar simulators. Appendix B is a short version of the work reported in the paper of the influence of concentrated solar radiation on a sooty flame. Appendix C is a pilot version of the journal paper about the global characteristics of flames using hydrogen-hydrocarbon blended fuels.

Reference

1.   B. Metz; O. Davidson; P. Bosch; R. Dave; L. Meyer, Mitigation of climate change, Cambridge University Press Cambridge, 2007, p.^pp.
2.   U. E. I. Administration, in: *Annual Energy Outlook*, 2013; Vol. DOE/EIA-0383(2013).
3.   M. Asif; T. Muneer, Renewable and Sustainable Energy Reviews 11 (7) (2007) 1388-1413
4.   V. Q. M.B.Muriel; , in: EIA, (Ed.) VGB Congress Power Plants: 2001.
5.   F.Kreith, in: 2007.
6.   G. Ordorica-Garcia; A. V. Delgado; A. F. Garcia, Energy Procedia 4 (0) (2011) 809-816.
7.   G. Nathan; D. L. Battye; P. J. Ashman, Applied Energy 113 (2014) 1235-1243
8.   Y. Ying; E. J. Hu, Applied Thermal Engineering 19 (11) (1999) 1173-1180
9.   Marwan Mokhtara; Muhammad Tauha Alia; Rajab Khalilpourb; Ali Abbasb; Nilay Shahc; Ahmed Al Hajajc; Peter Armstronga; Matteo Chiesaa; S. Sgouridisa, Applied Energy 92 (2012) 668-676
10.   SOLGATE, European Commision   (2005)
11.   C. P. Garcia P, Soler R, Gagnepain B, Ferriere A, Flamant G. , Journal of Solar Energy Engineering;   130 (14502) (2008) 1-3
12.   F. A. Grange B, Bellard D, Vrinat M, Couturier R, Fan Y. , Journal of Solar Energy Engineering 133: (31004) (2011) 1-11
13.   C. R. Gou C, Hong H. , Energy 32 (2007) 1707–1714.
14.   G. J. Kolb, Solar Energy 62 (1) (1998) 51-61
15.   Mehos MS; Anselmo KM; Moreno JB; Andraka CE; Rawlinson KS; C. J Combustion system for hybrid solar fossil fuel receiver. 2004.
16.   G. J. Nathan; Eric J. Hu; Bassam B. Dally; Zeyad T. Alwahabi; D. L. Battye; P. J. Ashman A boiler system receiving multiple energy sources. . 2009.
17.   Nathan GJ; Dally BB; Ashman PJ; S. A. A hybrid receiver combustor. 2012.
18.   P. Coelho, Progress in energy and combustion science 33 (4) (2007) 311-383
19.   W. H. Norton, The Norton History of Chemistry, W.W. Norton, New York, 1993,, p.^pp.
20.   P. R. Medwell; G. J. Nathan; Q. N. Chan; Z. T. Alwahabi; B. B. Dally, Combustion and Flame 158 (9) (2011) 1814-1821

CHAPTER 2

LITERATURE REVIEW

2.1 Influence of high flux radiation on combustion

Hybrids of concentrated solar thermal energy and fossil-fueled technologies are receiving growing attention because the combination of the two energy sources can provide lower emissions of carbon and other pollutants than pure fossil fuels, lower cost than pure solar thermal energy, and continuous supply [1, 2]. Various types of hybrid concepts have been proposed, e.g. preheating the feed water with the low grade solar energy [3], regenerating CO_2 solvents for the carbon capture and storage process [4], preheating the combustion air in a Brayton cycle [5-7], combining oxy-fuel combustion with solar thermal in a power cycle [8]. Since all of these concepts employ stand-alone solar receivers and combustors, there is great potential to reduce capital cost if shared infrastructure is employed for both energy sources, as was identified by Kolb [9]. Further to that, Mehos *et al.*[10] proposed one approach with which to better integrate these systems by mounting a combustor to the back of a solar receiver. More recently, Nathan *et al.* [2, 11, 12] has been developing an alternative approach with which to fully combine a combustor and a solar cavity receiver into a single device. This offers the potential for significant savings from reduced infrastructure investment and reduced start-up and shut-down losses [2]. A feature of this hybrid is that it results in the direct interaction between concentrated solar radiation and a flame, which are already known to be coupled, and that the relative strength of this interaction depends on the spectral characteristics of the species in the flame [13], details of which will be reviewed in Section 2.3.5.

The influence of concentrated solar radiation (CSR) on a flame was first experimentally investigated by Medwell *et al.*[14]. This work demonstrated that CO_2 laser radiation at 10.6 μm with a fluence of 4 MW/m^2 can approximately double the peak concentration of soot in an ethylene flame, and translate the soot layer towards the oxidizing side of the flame [14]. However, the previous investigation was undertaken with a single excitation wavelength on a small area of the

flame (5mm in diameter) [14], while the CSR is broadband and is of much larger radiant area. Therefore, the influence of broadband radiation of relevance to CSR on the whole flame is yet to be studied.

In order to experimentally assess the influence of CSR on combustion, the flame needs to be irradiated with high-flux broadband radiation typical of that from a concentrated solar receiver. This can be achieved by employing either concentrated solar radiation or simulated solar radiation provided by high-powered electrical lamps – a so-called solar simulator. Despite its abundance on earth, it is very challenging to use natural sunlight for research, owing to the high capital cost in establishing the heliostat field and the unrepeatable experimental conditions due to the variation of weather. In contrast, electrical solar simulators can provide high-flux, broad-band radiation in the visible spectrum in a well-controlled manner. However, they suffer from the disadvantages that their spectrum differs somewhat from that of the real solar resource, details of which will be reviewed in the following section.

2.2 High-flux solar simulators

2.2.1 Comparison of two types of lamps commonly used in solar simulators

Various high powered solar simulators employing electrically powered lamps, close-coupled with elliptical reflectors, have been reported in the literature with all aiming to simulate the intensity and spectrum of the radiation from solar concentrators (e.g. from a heliostat field or parabolic dish). Among all the high-flux solar simulators that have been reported in the public domain, two types of lamp have been predominantly used, which are the metal halide [15, 16] and xenon arc lamps [17-23]. The key characteristics that distinguish these two types of lamps are their different propensity to explode, which impacts both on safety and on the risk of a cascading failure; and the length of the electrical arc, which impacts on the final concentration ratio, and their radiant spectrum. The xenon arc bulbs are highly pressurized, making them vulnerable to explosion [24]. In contrast, the metal halide lamp is less vulnerable to explosion because of their secondary containment bulb that prevents hot pieces of debris from propagating into the working environment or impacting on other lamps, even though they are also pressurized. For metal halide lamps, this virtually eliminates the explosion risks to which xenon arc lamps are vulnerable [25]. On the other hand, the xenon arc lamp has a shorter electrical arc than does the metal halide lamp. This is desirable because the original dimension of the arc is magnified by the ellipsoidal reflector, so that the xenon arc lamp can generate a higher heat flux with a steeper Gaussian distribution than is possible with the long-arc metal halide lamp [26]. Nevertheless, while both types of lamp offer different advantages and disadvantages, gaps remain in the understanding of their relative merits, which justifies further investigation.

2.2.2 Spectra of solar simulators

2.2.2.1 Time-averaged spectra of solar simulators

As is discussed in Section 2.1, the major drawback of employing electrical solar simulators is that they offer a different spectrum than that of the real solar resource. The time-averaged spectra of xenon arc and metal halide lamps have been compared by Krueger [20] based on measurements reported by the manufacturers [24, 25]. Krueger identified that the differences between the spectra from the lamp and that of the sun at the site of Air Mass 1.5 [27] are less for the metal halide lamp than for the xenon arc lamp [20]. However, these measurements of the spectra are from the lamps alone, without accounting for the influence of the reflective surfaces used to concentrate the radiation. In addition, no direct comparison of the spectra of these lamps either with each other or with a real solar spectrum measured using the same instruments has been reported. Such a direct comparison is important because every spectrometer has its specific quantum efficiency at each wavelength. This makes it difficult to reliably compare spectra measured with different spectrometers, even with the response corrected, because the correction method may vary [28].

2.2.2.2 Time-resolved spectra of solar simulators

In addition to the direct comparison of the time-averaged spectra from solar simulators, details of the temporal variations in spectra are not yet available, even though the output from these lamps is known to fluctuate at a frequency related to that of the AC power supply [25, 29]. These fluctuations may be less important in receivers involving indirect heat transfer, e.g. through tubes, or where the residence time of the reactants is long compared with these oscillations, such as for the redox reactors with residence time of 8 s [30] or 34 s [31]. In contrast, the time-dependence of the spectra can have strong impacts on gas phase reactions among species that are spectrally absorbing in the visible spectra, particularly where the flows are turbulent so that the mixing time scales are of the order of milliseconds, and/or in reactors with short residence time. One such

example is in solar driven steam-gasification reactors, which involve the spectrally active gas phase species of CO, CO_2 and H_2O [32] and residence time of the order of 1 second [33]. Another example is the recently developed concept of a hybrid solar receiver and combustor, in which a turbulent flame, with residence time of the order of milliseconds, is directly irradiated by concentrated solar radiation [2]. Despite the significance of the time-resolved spectrum in such applications, the time-dependent spectral variations in metal halide and xenon arc lamps have not been reported before.

2.2.2.3 Influence of reflecting surface on the spectra of concentrated radiation

As is mentioned in Section 2.2.2.1, the lack of specific data has led to previous studies assuming that the spectrum from the concentrator is unchanged from that of the lamp as reported by the manufacturer [20]. However, any reflecting surface has its own specific spectral reflectivity [34, 35]. Furthermore, the reflectors for solar simulators are typically manufactured from highly polished aluminum, the reflective properties of which can be expected to influence the spectrum more significantly than would occur with the use of a perfect mirror. For these reasons it is important to quantify its influence on the spectrum of the concentrated light, even if it is small. However, the influence of the reflecting surface on the spectra of the concentrated radiation is yet to be reported.

2.2.3   Modelling and measurement of the flux distribution at the focal area

In addition to the spectra, the heat flux of concentrated radiation from solar simulators is also of great interest, because the efficiency of most practical solar receiver systems is directly related to the intensity of radiation. It is therefore important to quantify the heat flux at the focal area, not only for an existing system, but also to predict that from a new design using computational models, thus allowing the design to be undertaken with relatively high accuracy without first establishing a physical system and performing further experimental measurements of the heat flux distribution at

the target.

The modelling and measurement of the output from a variety of high powered solar simulator systems, comprising high-intensity-discharge lamps coupled with elliptical reflectors have been reported previously. While the measurement of heat flux distribution at the focal plane has been reported in most of the designs [16-23], only a few of them have reported the model of the arc used for the ray-tracing simulation [17, 18, 20, 21, 36], and even less have compared the predicted and measured heat flux distribution [18, 21]. Furthermore, the measurement of the arc profile, as well as the sensitivity analysis of the model of the arc on the prediction of heat flux distribution at target are not yet available in the literature. Therefore, there is a need both for the measurements of the properties of the light source and for various approaches with which to model the light source.

2.2.3.1 Significance of the structure of the arc profile

A prerequisite of an accurate prediction of the concentrated heat flux is a model of the light source that precisely represents the structure and intensity of the discharge arc, because the final prediction of heat flux distribution at the target is strongly sensitive to the original assumptions of the energy distribution of this light source. This justifies a detailed study of the structure of the light source. The time-averaged radiant distribution of the arc is not spatially uniform in energy density [37-40]. In contrast, previously reported analyses have assumed an uniformly distributed light source with radiation issuing from the surface of a sphere [17, 21], a cone [18] or within the volume of a cylinder with specified angular distribution [20, 36]. There is therefore a need to develop a model that accurately represents the structure, particularly the non-uniform energy distribution of the light source.

2.2.3.2 Significance of the shape and dimension of the arc profile

The details of shape and dimensions of the arc are also important, because any error on the assumptions of the shape and dimensions of the arc will be amplified by the reflector, resulting in

bigger error on the prediction of the heat flux distribution at the focal plane [41]. Although the mathematical relations between an extended source and its image from an elliptical reflector on the secondary focal plane has been derived by Rehn [41], the error of this analytical solution is yet to be quantified by comparison with experimental data. Petrasch *et al.* [17] have also numerically analyzed the effect of arc dimension on the transfer efficiency of the elliptical reflector, while Kruger [20] has assessed the influence of arc geometry and dimension on the transfer efficiency and flux non-uniformity. Despite their value, these assessments also have their limitations, because a better performance in transfer efficiency does not necessarily coincide with a better performance in non-uniformity. Hence there is a need to directly compare the assumed and measured intensity distribution of the arc, together with the equivalent values of heat flux distribution at the focal plane to provide a more robust and detailed assessment of the model's performance. However, the sensitivity analysis of the assumed size, shape and energy distribution of the arc on the distribution of the concentrated heat flux has not been reported before.

2.2.3.3 Measurements of the light source

Different types or designs of arc lamps typically generate different profiles of the arc source [37-40]. Although the lamp manufacturers generally report the half width for the profile of radiant intensity of the arc averaged from various lamps [40], it is impossible to determine the full shape of the profile from this data alone. Therefore, an accurate measurement of the profile of the light source provides critical information to the input of the model. However, these measurements and the modelling approach have not yet been available.

2.2.3.4 Measurement of the heat flux distribution at the focal area

An accurate measurement of the heat flux profile at the focal plane (i.e. the position of the target) is also desired for reliable validation of the final output from the models, e.g. the Monte-Carlo ray-tracing model. Although the measurement of heat flux at the focal plane has been reported in the

literature [17, 18, 20], no heat flux measurements have been reported together with the measurement of the arc profile for both the model input and output.

2.2.4   Secondary and tertiary concentrators of the solar simulator

The combination of a discharge arc lamp, coupled with elliptical reflector, and also aligned with a secondary and tertiary conical concentrators has been reported previously [16]. These studies demonstrate that the use of secondary concentrator can significantly increase the heat flux in the area of interest. The benefit of a secondary concentrator is more significant for the long-arc metal halide lamps than for the short-arc xenon-arc lamps that have been used most commonly in previous solar simulators [17-23]. Although it is inevitable that there will be some energy loss from the secondary concentrator itself, this loss is compensated by a more concentrated flux in the target area. Nevertheless, this requires the geometry of the concentrator be properly designed. This is because if the opening angle of the concentrator is too large, it tends to reflect more radiation to the lamp side rather than concentrate it, while if it is too small it is not possible to capture all of the radiation, especially with a multiple lamp system. In addition, if the secondary concentrator is further aligned with a back reflector, it would be advantageous compared with enclosed reactors in providing an open system, which is particularly useful for diagnostics using optical methods. However, the optimization of the secondary/tertiary concentrator for either a single lamp system or a multi-lamp solar simulator has not been reported in the literature.

In addition, although the measurement of heat flux at the focal plane has been reported in the literature [17, 18, 20] for the case without the secondary concentrator [42], that with the secondary concentrator present is not yet available. This experimental validation is also desirable, because the addition of the secondary concentrator can significantly change the path ways of the radiation, depending on the geometry and reflectance of the secondary concentrator.

Additionally, the sensitivity of concentrated heat flux to the surface reflectance of

secondary/tertiary concentrators provides important information for the choice of materials. It is expected that surfaces with lower reflectance will lower the cost at the expense of a lower concentration ratio. However, because of the multiple reflections involved in the concentration, it is difficult to quantify this without detailed calculations and/or experimental measurement. Though the influence of surface roughness of the elliptical reflector on the concentrated heat flux has been assessed by Alxneit and Dibowski using ray tracing code [18], no such assessment of the surface reflectance has been reported before.

Furthermore, though the influence of misalignment between the arc and the elliptical reflector on the heat flux distribution at the target is critical information to guide the procedure of the alignment, for both the single-lamp and multiple lamp systems, it has not been reported before. A comparison of the effect of misalignment with the conical secondary concentrator on and off is also useful, because it is expected that the conical concentrator can potentially reduce the sensitivity of the concentrated heat flux to the misalignment between the arc and the primary elliptical reflector.

2.3   Combustion-CSR interaction

2.3.1   Role of soot in combustion-CSR interaction

Soot is one of the key components in many combustion systems. This is because, within a flame, an increased presence of soot acts to increase the flame emissivity and hence the radiation — the dominant heat transfer mode in kilns, boilers and furnaces [43, 44]. Therefore, in these applications, an increase of soot concentration within the flame is highly desirable. However, as is discussed in Section 2.1, further study following Medwell *et al.*'s [14] work is required to determine the influence of broadband radiation of relevance to CSR on the soot volume fraction of the whole flame.

In most applications, the presence of soot outside a flame is undesirable because it is a source of fine particle emissions [45], although it can also be used as a source of "carbon black" for manufacturing [46]. Therefore, the consumption of soot in the oxidation zone of the flame is also of great interest. However, this information is not yet available in the literature. It is also hard to be deduced from the previous work reported by Medwell *et al.*[14]. This is because the previous assessment was done on flames stabilized on a Mckenna type burner, for which only locations with lower height above burner (HAB) were studied [14], while the consumption of soot mainly takes place at flame locations with higher HABs.

2.3.2   Measurement of soot volume fraction using laser induced incandescence (LII) technique

While combustion processes involving soot have been employed for many years, the formation and destruction of soot are still difficult to model in practical combustion environments [46]. This is because the radiation from soot and chemical reactions within the flame are coupled non-linearly [47]. Therefore in-situ measurement has been considered the most reliable way to quantify soot

concentration. Among many parameters involving soot, the measurement of soot volume fraction (SVF) within a flame can provide particularly valuable insights to the evolution of soot growth and radiant transport [48, 49]. Laser-induced incandescence (LII) has proven to be a powerful tool for particle-concentration [50], owing to its ability of performing in-situ, non-intrusive and highly accurate measurements [51]. However, the concentrated solar radiation brings additional challenges to the optical methods. This is because strong background scattering originates from particles under the irradiation of the high-flux solar energy and this causes strong interference to the signals collected in the LII measurement. Although the previous measurement has demonstrated that LII can stand the environment of high flux laser radiation [14], the viability of LII in sooting flames under strong broadband irradiation is yet to be demonstrated.

2.3.3 Role of temperature in combustion-CSR interaction

Combustion involves the non-linearly coupled processes of heat transfer, turbulence and chemistry, which are all dependent on flame temperature. The strength of this coupling can be expected to increase with the introduction of CSR, because external broadband radiation can influence the chemical species in a flame through direct and indirect molecular excitation, as well as blackbody radiation from soot [14]. It is therefore important to measure temperature distribution in this challenging high temperature receiver-combustor environment. This, in turn, demands advanced technique for temperature measurements.

2.3.4 Measurement of temperature using non-linear two-line atomic fluorescence (TLAF)

As was discussed in Section 2.3.2, the strong background scattering from particles under the irradiation of the high-flux solar energy also prevents many of the optical methods for temperature measurement to be applied reliably. For example, Rayleigh scattering/filtered Rayleigh scattering thermometry suffers from low signal-to-noise ratio (SNR) in sooting flames. Coherent anti-Stokes

Raman spectroscopy (CARS) has been demonstrated to measure the gas temperature of a reacting flow in a solar receiver/reactor, but it has been limited to point measurements [52]. Laser-induced fluorescence (LIF) based thermometry, on the other hand, possesses potential advantages compared to these aforementioned laser diagnostic tools in strong scattering background environments, owing to its signal is collected at a wavelength that is shifted away from its excitation wavelength. Particularly, two-line atomic fluorescence (TLAF) uses indium as tracer species provides an attractive option for the measurement of temperature under high-flux external radiation. This is because, in comparison to probing LIF signal from naturally existing species such as OH and NO, LIF signal from seeded atomic species is much stronger and exists in broader regions in the flames [47]. However, TLAF in sooting flames under strong irradiation is yet to be demonstrated.

2.3.5   Possible pathways through which CSR can interact with a flame

Generally, benzene, small aromatic hydrocarbons and PAH are UV absorbers and IR emitters [53, 54]. To be more specific, the carbonaceous materials of 2-3 nm in size absorb UV radiation of under 300 nm in wavelength and emit broadband radiation peaked at 330 nm [55-57], while the carbonaceous particles of 5-10 nm in size absorb radiation of 250-400 nm [56], those particles sized 10-30 nm also absorb UV radiation of 250-400 nm, but at a higher absorption rate, and carbon particles of about 100 nm in size become broadband absorbers in the UV-visible range [56, 57]; This is because the energy gap between the π— $\pi*$ bands decreases as the coordination length of the bonds increases and, consequently, the absorption spectra of poly-condensed aromatic functionalities shift toward the visible as the number of aromatic rings increases.

In addition to the absorption of carbonaceous particles, gas phase species such as C_2H_2 and H_2O absorb infrared radiation, while benzene and PAH are UV absorbers [58-60]. The molecular absorption is important, because where an energy transition of the fuel molecule can be excited, it typically leads to increased pyrolysis of the fuel, as has been demonstrated for ethylene heated by a CO_2 laser in pyrolysis reactors [61]; Any absorption that promotes fuel decomposition or the

formation of small aromatics is important because this is a rate-limiting step, even though it constitutes only a small part in the overall soot formation process [62-64].

The mechanism of black body absorption is well known to occur for small particles such as soot and pulverized coal [14]. It is also well known that this mechanism, where present, tends to dominate over molecular excitation because it is a broad-band absorber [14]. This can be evidenced by the laser extinction measurement in laminar diffusion flames reported by Ma and Long [65], which shows that the diffusion flame of 80% ethylene and 20% nitrogen absorbs laser radiation ranging from 450-700 nm, with an average absorption of 11.8% at HAB = 30mm, and 15.4% at HAB = 50mm. Furthermore, The extinction measurements using broadband radiation of 450-1100 nm through a laminar non-premixed ethylene flame reported by Migliorini *et al* .[66] show that, the line of sight absorption through the laminar ethylene diffusion flame at HAB/L_f= 0.14, 0.59, 0.70, and 0.77 is 0.029, 0.124, 0.073, 0.053 respectively. Despite the evidence of the interactions between the narrowband/broadband electromagnetic radiation and combustion, the potential mechanisms of the interactions between the concentrated solar radiation and combustion are yet to be explored.

2.3.6   Influence of the intensity of CSR on a flame

In addition to the quality, i.e. the spectral effect, of the irradiation, the quantity of the energy that is coupled into the flame may also play an important role on the magnitude of influence of CSR on a flame. To assess this influence, the previous relevant studies were compared [14, 67], as is shown in Table 1. If the ratio of the external energy to the combustion energy is defined as Eq. 1:

$$f_e = \frac{E_{CSR}}{E_{flame}} \quad , \qquad (1)$$

Then f_e for the work of Konsur *et al* [67] is up to 0.44%, that for the study of Medwell *et al.* is 13.3%. It can be seen that there are big differences in f_e between the two studies, and care should

be taken while trying to directly compare them. Because for the experiments of Konsur *et al.* [67], the external energy is the energy actually absorbed by the fuel. However, for the measurements of Medwell *et al.* [14], it is not yet clear what is the fraction of the external energy that is finally absorbed by the flame, though the f_e is higher. Nevertheless, the comparison of f_e itself still shows that, the peak soot volume fraction (f_v) in the flame is likely to increase with the increase of the fraction of external energy coupled into the flame.

Table 1. Comparison of the previously reported work.

Source	Coupling method	Q_{flame} (W)	$Q_{external}$	f_e $(\frac{Q_{external}}{Q_{flame}})$	Increase of peak f_v
Konsur *et al.* [67]	Fuel preheating to ΔT=97 and 137	106.6	0.32864 W (ΔT=97 K) 0.46416 W (ΔT=137 K)	0.31% 0.44%	5%
Medwell *et al.* [14]	10.6 μm laser radiation	517.8	69 W	13.3%	250%

2.4 Global performance of flames of different soot propensity

2.4.1 Soot volume fraction on the global performance of hydrogen-hydrocarbon blended flames

As has been demonstrated by Medwell *et al.*[14] and also reviewed in the previous section, a potential significant influence of the concentrated solar radiation on flames is that it may increase the soot volume fraction in a flame. Hence a further review of the influence of soot volume fraction on the global performance of the flame is important to further assess its influence on practical combustion processes. A reliable assessment of the influence of soot volume fraction on the global performance of the flames can be realized through a systematic study of flames using fuels of different soot propensities. This justifies the use of hydrocarbon fuels blended with hydrogen, through which the soot propensity of the fuel can range from that of pure hydrocarbon fuels to pure hydrogen. This will allow a trend to be derived of the global performance as a function of soot propensity of the fuel. This indirect way of assessment was preferred because the direct measurement of the changes of radiation from the flame under concentrated solar radiation is difficult due to the strong scattering of solar radiation by soot particles. The global performances of turbulent flames were targeted for the current study, because such global performances as the radiant fraction, flame size and pollutant emissions of turbulent flames are of great relevance to the practical combustion systems.

2.4.2 Effects of lift-off, strain rate and the hydrogen ratio on hydrogen-hydrocarbon blended flames

Although the global performance of hydrogen-hydrocarbon blended fuels has been measured previously, significant gaps remain. Choudhuri*et al.* [68] measured a series of turbulent diffusion flames with a Reynolds number of 8,700, while Wu *et al.* [69] reported measurements of the lift-off and blow-off stability limits of pure hydrogen and hydrogen/hydrocarbon blended jet flames. However, not all of these flames were attached to the burner. Where lift-off occurs it is impossible

to isolate the chemical effects due to the addition of H_2 from those of the different physical entrainment mechanisms for lifted and attached flames. Therefore, there remains a need to investigate the effect of varying the hydrogen volume fraction for flames that are all attached. The previous measurements of Turns and Myhr [70], were performed with hydrocarbon fuels surrounded by a hydrogen pilot, which is not the same as blended fuel, while the measurements of El-Gafour*et al.* [71] were limited to natural gas as the hydrocarbon component and to a maximum hydrogen volume fraction of 50%. Furthermore, no previous hydrogen-hydrocarbon flames have been investigated under constant exit strain rate, u/d, which strongly influences the axial and radial soot volume fraction profiles [72, 73].

2.4.3   Significance of boundary conditions

It is also important to note that none of the previous global flame measurements have been performed under boundary conditions that are sufficiently well defined to enable them to be modelled unambiguously. The development and validation of a computational fluid dynamics (CFD) model requires that the inflow boundary conditions, such as the mean and RMS velocity profiles, be reported. The process of model development and validation also requires sufficient detailed in-flame measurements to be reported for the same flames, to enable the sources of radiation, notably from the presence of soot, to be linked unambiguously to the global emissions of pollutant gases and radiation. Importantly, none of the previous global measurements of flames associated with hydrogen blends have either reported the inflow boundary conditions or are linked to other detailed in-flame measurements of parameters such as temperature and soot volume fraction. The recent advances in experimental techniques suitable for application in turbulent flames [47] means that it is now possible to achieve this. For example, a series of detailed measurements of soot volume fraction and temperature have recently been undertaken for four flames of a particular blend of 40% C_2H_4 + 41% H_2 + 19% N_2, carefully chosen to achieve attached, turbulent flames without a pilot. The first of these measurements are reported by Mahmoud *et al.* [74], who report joint statistics of soot volume fraction and flame temperature from simultaneous measurements of these parameters. However, the global measurements of flame

radiation and emissions to for these flames are yet to be reported.

2.5 Objective of the thesis

The primary objective of the thesis is to investigate the influence of concentrated solar radiation on sooty flames.

The detailed objectives of the thesis are:

1. To design and establish a high flux solar simulator using a discharge arc lamp, closely coupled with an elliptical reflector. To perform measurement of both the radiant distribution of the light source and the heat flux distribution on the focal plane to validate the input and output of the ray-tracing model, thus allowing a new design to be undertaken without first establishing an experimental platform.

2. To characterize the spectral property of the solar simulator, which involves the measurement of both the time-averaged and time-resolved spectral irradiance of solar simulators made of metal halide and xenon arc lamps, as measured before and after concentration from the optical reflectors of a high flux solar simulator.

3. To quantify the influences of the CSR on combustion by irradiating the whole flame with high flux broadband radiation, and performing in-situ soot volume fraction measurement using LII and temperature measurement using TLAF technique.

4. To assess the effect of soot volume fraction on the global performance of turbulent flames through flames of hydrogen-hydrocarbon blended fuels. This will be achieved by evaluating the influence of hydrogen blend ratio on such global performances as radiant fraction, flame size and pollutant emissions of non-premixed turbulent flames using hydrocarbon fuels.

5. To design and optimize the geometry of secondary/tertiary concentrators for the solar simulators to achieve higher flux and larger radiant area, using a ray-tracing model that is experimentally validated.

References

1.   G. Ordorica-Garcia; A. V. Delgado; A. F. Garcia, Energy Procedia 4 (0) (2011) 809-816.
2.   G. Nathan; D. L. Battye; P. J. Ashman, Applied Energy 113 (2014) 1235-1243
3.   Y. Ying; E. J. Hu, Applied Thermal Engineering 19 (11) (1999) 1173-1180
4.   Marwan Mokhtara; Muhammad Tauha Alia; Rajab Khalilpourb; Ali Abbasb; Nilay Shahc; Ahmed Al Hajajc; Peter Armstronga; Matteo Chiesaa; S. Sgouridisa, Applied Energy 92 (2012) 668-676
5.   SOLGATE, European Commision   (2005)
6.   C. P. Garcia P, Soler R, Gagnepain B, Ferriere A, Flamant G. , Journal of Solar Energy Engineering;   130 (14502) (2008) 1-3
7.   F. A. Grange B, Bellard D, Vrinat M, Couturier R, Fan Y. , Journal of Solar Energy Engineering 133: (31004) (2011) 1-11
8.   C. R. Gou C, Hong H. , Energy 32 (2007) 1707–1714.
9.   G. J. Kolb, Solar Energy 62 (1) (1998) 51-61
10.   Mehos MS; Anselmo KM; Moreno JB; Andraka CE; Rawlinson KS; C. J Combustion system for hybrid solar fossil fuel receiver. 2004.
11.   G. J. Nathan; Eric J. Hu; Bassam B. Dally; Zeyad T. Alwahabi; D. L. Battye; P. J. Ashman A boiler system receiving multiple energy sources. . 2009.
12.   Nathan GJ; Dally BB; Ashman PJ; S. A. A hybrid receiver combustor. 2012.
13.   P. Coelho, Progress in energy and combustion science 33 (4) (2007) 311-383
14.   P. R. Medwell; G. J. Nathan; Q. N. Chan; Z. T. Alwahabi; B. B. Dally, Combustion and flame)
15.   B. Ekman, http://www.swinburne.edu.au/media-centre/   (2014)
16.   D. S. Codd; A. Carlson; J. Rees; A. H. Slocum, Solar Energy 84 (12) (2010) 2202-2212
17.   J. Petrasch; P. Coray; A. Meier; M. Brack; P. Häberling; D. Wuillemin; A. Steinfeld, Journal of Solar Energy Engineering 129 (4) (2007) 405-411
18.   I. Alxneit; G. Dibowski, in: *Project SFERA*, PSI and DLR: 2011.
19.   R. A. Craig. Investigating the use of Concentrated Solar Energy to Thermally Decompose Limestone. The University of Adelaide, Adelaide, 2010.
20.   K. R. Krueger. Design and Characterization of a Concentrating Solar Simulator. UNIVERSITY OF MINNESOTA, 2012.
21.   Z. Li; D. Tang; J. Du; T. Li, Applied Thermal Engineering 31 (10) (2011) 1780-1789
22.   P. Kuhn; A. Hunt, Solar Energy Materials 24 (1-4) (1991) 742-750
23.   J. Sarwar; G. Georgakis; R. LaChance; N. Ozalp, Solar Energy 100 (0) (2014) 179-194.
24.   in: *xenon lamp listing*, Christie: www.projectionniste.net, 2008.
25.   OSRAM, in: *HMI 6000 W/SE*, 11/04 ed.; Display/Optic Berlin: 2011.
26.   X. Dong; P. J. Ashman; G. J. Nathan; Z. Sun, in: *Chemeca 2013*, Engineering Collection: Brisbane, Australia, 2013.
27.   C. Gueymard; D. Myers; K. Emery, Solar energy 73 (6) (2002) 443-467
28.   A. T. R. Williams; S. A. Winfield; J. N. Miller, Analyst 108 (1290) (1983) 1067-1071
29.   Osram, in: Osram.
30.   P. Furler; J. R. Scheffe; A. Steinfeld, Energy & Environmental Science 5 (3) (2012) 6098-6103
31.   W. C. Chueh; C. Falter; M. Abbott; D. Scipio; P. Furler; S. M. Haile; A. Steinfeld, Science 330 (6012) (2010) 1797-1801
32.   D. E. Burch; D. A. Gryvnak; R. R. Patty; C. E. Bartky, JOSA 59 (3) (1969) 267-278
33.   A. Z'graggen; P. Haueter; D. Trommer; M. Romero; J. De Jesus; A. Steinfeld, International Journal of Hydrogen Energy 31 (6) (2006) 797-811
34.   J. Bartl; M. Baranek, Measurement of Physical Quantities 43 (2004) 3136
35.   B. Karlsson; C. G. Ribbing, Journal of Applied Physics 53 (9) (1982) 6340-6346

36.   R. Bader; S. Haussener; W. Lipiński, Journal of Solar Energy Engineering 137 (2) (2015) 021012

37.   K. R. S. T. J. F. M. W. Davidson, in: Olympus http://www.olympusconfocal.com.

38.   M. W. D. P. Dirac, in: http://zeiss-campus.magnet.fsu.edu: http://zeiss-campus.magnet.fsu.edu/articles/lightsources/mercuryarc.html.

39.   Newport, in: Newport: http://www.newport.com/DC-Short-Arc-Lamps-Flashlamps.

40.   in: MetalL Halide Lamps and Photo Optics, OSRAM.

41.   H. Rehn, Optical Engineering 43 (7) (2004) 1480-1488

42.   X. Dong; G. J. Nathan; Z. W. Sun; D. H. Gu; P. J. Ashman, Solar Energy, acceptted   (2015)

43.   M. A. Delichatsios; J. De Ris; L. Orloff, Symposium (International) on Combustion 24 (1) (1992) 1075-1082

44.   Q. N. Chan; P. R. Medwell; P. A. Kalt; Z. T. Alwahabi; B. B. Dally; G. J. Nathan, Proceedings of the Combustion Institute 33 (1) (2011) 791-798

45.   W. H. Organization,   (2003)

46.   Z. A. Mansurov, Combustion, Explosion and Shock Waves 41 (6) (2005) 727-744

47.   G. Nathan; P. A. M. Kalt; Z. T. Alwahabi; B. B. Dally; P. R. Medwell; Q. N. Chan, Progress in energy and combustion science 38 (1) (2012) 41-61

48.   M. Choi; G. W. Mulholland; A. Hamins; T. Kashiwagi, Combustion and Flame 102 (1) (1995) 161-169

49.   N. Qamar; G. Nathan; Z. Alwahabi; K. King, Proceedings of the Combustion Institute 30 (1) (2005) 1493-1500

50.   B. Axelsson; R. Collin; P. E. Bengtsson, Applied Physics B 72 (3) (2001) 367-372 10.1007/s003400100504.

51.   C. Schulz; B. F. Kock; M. Hofmann; H. Michelsen; S. Will; B. Bougie; R. Suntz; G. Smallwood, Applied Physics B 83 (3) (2006) 333-354

52.   A. Steinfeld; R. Bombach; P. Haueter; B. Hemmerling; W. Kreutner; G. Thompson; D. Wuillemin, Journal of solar energy engineering 116 (4) (1994) 206-211

53.   W. W. Duley; D. A. Williams, The Astrophysical Journal Letters 737 (2) (2011) L44

54.   G. Malloci; C. Joblin; G. Mulas, Chemical Physics 332 (2) (2007) 353-359

55.   L. Sgro; P. Minutolo; G. Basile; A. D'Alessio, Chemosphere 42 (5) (2001) 671-680

56.   L. A. Sgro; G. Basile; A. C. Barone; A. D'Anna; P. Minutolo; A. Borghese; A. D'Alessio, Chemosphere 51 (10) (2003) 1079-1090

57.   P. Minutolo; G. Gambi; A. D'Alessio; S. Carlucci, Atmospheric Environment 33 (17) (1999) 2725-2732

58.   S. Fally; M. Carleer; A. C. Vandaele, Journal of Quantitative Spectroscopy and Radiative Transfer 110 (9–10) (2009) 766-782.

59.   Ž. Tomović; M. D. Watson; K. Müllen, Angewandte Chemie International Edition 43 (6) (2004) 755-758

60.   M. G. Debije; J. Piris; M. P. de Haas; J. M. Warman; Z. Tomovic; C. D. Simpson; M. D. Watson; K. Müllen, Journal of the American Chemical Society 126 (14) (2004) 4641-4645

61.   I. Morjan; I. Voicu; F. Dumitrache; I. Sandu; I. Soare; R. Alexandrescu; E. Vasile; I. Pasuk; R. M. D. Brydson; H. Daniels; B. Rand, Carbon 41 (15) (2003) 2913-2921

62.   I. Glassman in: Soot formation in combustion processes, Symposium (international) on combustion, 1989; Elsevier: 1989; pp 295-311.

63.   C. S. McEnally; L. D. Pfefferle; B. Atakan; K. Kohse-Höinghaus, Progress in Energy and Combustion Science 32 (3) (2006) 247-294

64.   C. S. McEnally; D. M. Ciuparu; L. D. Pfefferle, Combustion and flame 134 (4) (2003) 339-353

65.   B. Ma; M. B. Long, Applied Physics B 117 (1) (2014) 287-303

66.   F. Migliorini; K. A. Thomson; G. J. Smallwood, Applied Physics B 104 (2) (2011) 273-283 10.1007/s00340-011-4396-4.

67.   B. Konsur; C. M. Megaridis; D. W. Griffin, Combustion and flame 116 (3) (1999) 334-347

68.   A. R. Choudhuri; S. Gollahalli, International journal of hydrogen energy 28 (4) (2003) 445-454

69.   Y. Wu; Y. Lu; I. Al-Rahbi; G. Kalghatgi, International journal of hydrogen energy 34 (14) (2009) 5940-5945

70.   S. R. Turns; F. H. Myhr, Combustion and flame 87 (3) (1991) 319-335
71.   S. El-Ghafour; A. El-dein; A. Aref, International journal of hydrogen energy 35 (6) (2010) 2556-2565
72.   J. Kent; S. Bastin, Combustion and flame 56 (1) (1984) 29-42
73.   N. Qamar; G. J. Nathan; Z. T. Alwahabi; K. D. King, Proceedings of the Combustion Institute 30 (1) (2005) 1493-1500
74.   S. Mahmoud, Nathan, G.J., Medwell, P.R., Dally, B.B., Alwahabi, Z.T., Proceedings of the Combustion Institute vol. 35, accepted. (2015)

CHAPTER 3

CONCENTRIC MULTILAYER MODEL OF THE ARC IN HIGH INTENSITY DISCHARGE LAMPS FOR SOLAR SIMULATORS WITH EXPERIMENTAL VALIDATION

Xue Dong[1], Graham J. Nathan[2], Zhiwei Sun[2], Dahe Gu[2], Peter J. Ashman[1]

Centre for Energy Technology, [1]Schools of Chemical Engineering & [2]Mechanical Engineering,
The University of Adelaide, Adelaide, SA 5005, Australia
Email: xue.dong@adelaide.edu.au

Statement of authorship

Title of Paper	Concentric multilayer model of the arc in high intensity discharge lamps for solar simulators with experimental validation
Publication Status	☐ Published ☑ Accepted for Publication ☐ Submitted for Publication ☐ Publication Style
Publication Details	Solar Energy

Principal Author

Name of Principal Author (Candidate)	Xue Dong		
Contribution to the Paper	Under the supervision of P. J. Ashman and G. J. Nathan, I developed the experimental methods, performed the experiments, processed the data and wrote the manuscript.		
Overall percentage (%)	55%		
Signature		Date	09/09/2015

Co-Author Contributions

By signing the Statement of Authorship, each author certifies that:

    i.   the candidate's stated contribution to the publication is accurate (as detailed above);

    ii.   permission is granted for the candidate in include the publication in the thesis; and

    iii.   the sum of all co-author contributions is equal to 100% less the candidate's stated contribution.

Name of Co-Author	Peter J. Ashman		
Contribution to the Paper	I acted as primary supervisor for the candidate, aided in developing of the experimental method, revising the manuscript and evaluating the final version of the manuscript. I give consent for Xue Dong to present this paper for examination towards the Doctorate of Philosophy.		
Signature		Date	9/9/15

Name of Co-Author	Graham J. Nathan		
Contribution to the Paper	I acted as secondary supervisor for the candidate, aided in developing of the experimental method, revising the manuscript and evaluated the final version of the manuscript. I give consent for Xue Dong to present this paper for examination towards the Doctorate of Philosophy.		
Signature		Date	10/9/15.

Name of Co-Author	Zhiwei Sun
Contribution to the Paper	I am a post-doc who co-supervised the experimental campaign, aided in developing of the experimental method, performing the experiments, revising the manuscript and evaluating the final version of the manuscript. I give consent for Xue Dong to present this paper for examination towards the Doctorate of Philosophy.
Signature	Date 01/09/2015

Name of Co-Author	Dahe Gu
Contribution to the Paper	I am a fellow PhD student, aided in performing the experiments and evaluated the final version of the manuscript. I give consent for Xue Dong to present this paper for examination towards the Doctorate of Philosophy.
Signature	Date 1 /9 / 2015

Concentric multilayer model of the arc in high intensity discharge lamps for solar simulators with experimental validation

Xue Dong [a],*, Graham J. Nathan [b], Zhiwei Sun [b], Dahe Gu [b], Peter J. Ashman [a]

[a] Centre for Energy Technology, School of Chemical Engineering, The University of Adelaide, Adelaide, SA 5005, Australia
[b] Centre for Energy Technology, School of Mechanical Engineering, The University of Adelaide, Adelaide, SA 5005, Australia

Abstract

High flux solar simulators, comprising high-intensity-discharge lamps coupled with elliptical reflectors, have been widely employed to study concentrated solar thermal energy systems in a controlled manner. However, little information is available of the influence of the assumptions about the properties of the arc on the accuracy of the prediction of the heat flux at the focal plane. This paper presents a concentric multilayer model of the arc that is developed to predict the spatial distribution of the heat flux at the focus. Measurements were performed of both the time-resolved and time-averaged spatial distribution of the discharge arc from a commercial metal halide lamp with a 23 mm spacing between the two electrodes. The efficacy of various alternative simplified approaches to model the arc using a commercial Monte Carlo ray-tracing code were assessed, which include models of cylinder, monopole sphere, dipole-sphere and three types of compounds of these three shapes. These predictions were validated with measurements using a CCD camera and a heat flux gauge, which shows that the predicted profiles from the three compound models agree with the experimental results to similar extent, with no difference in the predicted maximum heat flux and within a difference of 11% for the predicted half-width.
Crown Copyright © 2015 Published by Elsevier Ltd. All rights reserved.

1. Introduction

The use of electrically powered lamps to simulate concentrated solar radiation has become increasingly common, because of its advantage over natural solar radiation in providing repeatable performance by avoiding the need to accommodate the variability of the solar resource (Dong et al., 2015). The design of a variety of high powered solar simulator systems, comprising high-intensity-discharge lamps coupled with elliptical reflectors have been reported, as is summarized in Table 1. It can be seen in Table 1 that, while the measurement of the distribution of the concentrated heat flux has been reported in most of the designs (Petrasch et al., 2007; Krueger, 2012; Codd et al., 2010; Craig, 2010; Alxneit and Dibowski, 2011; Li et al., 2011; Kuhn and Hunt, 1991; Sarwar et al., 2014), only a few of them have reported the model of the arc for ray-tracing simulation (Petrasch et al., 2007; Krueger, 2012; Alxneit and Dibowski, 2011; Li et al., 2011; Bader et al., 2015), and even less have compared the heat flux distribution of the simulation with the measurement (Alxneit and Dibowski, 2011; Li et al., 2011). Furthermore, neither measurements of the arc profile nor the sensitivity analysis of the predicted heat flux distribution at the target to the assumptions of the properties of the arc are available in

* Corresponding author.
E-mail address: xue.dong@adelaide.edu.au (X. Dong).

Table 1
Details of previously reported designs of high-flux solar simulators.

Source	Type of solar simulator	Type of model used for simulation of the arc profile	Arc profile measurement	Methodology used to measure the concentrated heat flux	Experimental validation of the concentrated heat flux	Sensitivity assessment of the arc model
Petrasch et al. (2007)	Xenon arc + elliptical reflector	Single layer of sphere	–	CCD + calorimeter	–	–
Krueger (2012)	Xenon arc + elliptical reflector	Uniform cylindrical volume	–	CCD + calorimeter	Reported	Reported
Ekman (2014)	Metal halide + elliptical reflector	–	–	–	–	–
Codd et al. (2010)	Metal halide + elliptical reflector + conical concentrator	–	–	Calorimeter	–	–
Craig (2010)	Xenon arc + elliptical reflector	–	–	CCD + heat flux gauge	–	–
Alxneit and Dibowski (2011)	Xenon arc + elliptical reflector	Single layer of cone	–	CCD + heat flux gauge	Reported	–
Li et al. (2011)	Xenon arc + elliptical reflector	Single layer of sphere	–	Thermopile	Reported	–
Kuhn and Hunt (1991)	Xenon arc + elliptical reflector	–	–	Calorimeter	–	–
Sarwar et al. (2014)	Xenon arc + elliptical reflector	–	–	CCD + heat flux gauge	–	–
Bader et al. (2015)	Xenon arc + elliptical reflector	Uniform cylindrical volume	–	–	–	–
Current study	Metal halide + elliptical reflector	Multilayers of different shapes	Reported	CCD + heat flux gauge	Reported	Reported

the literature. However, the significance of the energy distribution of the arc increases with the spacing between the electrodes, since the departure of the arc from a point source increases with the length of the arc. Hence this issue is more significant for the metal halide lamps, for which the electrode spacing of a 6000 W lamp is 23 mm, than for the xenon-arc lamps that have been used commonly in previous solar simulators (Petrasch et al., 2007; Krueger, 2012; Craig, 2010; Alxneit and Dibowski, 2011; Li et al., 2011; Kuhn and Hunt, 1991; Sarwar et al., 2014), for which the electrode spacing of a 6000 W lamp is typically 9 mm. However, the metal halide lamps offer the advantages of a spectrum that better matches that of the solar resource, improved safety and a lower risk of cascading failure (Dong et al., 2015). Therefore, there is a need both for measurements of the properties of the light source and for various approaches with which to model the arc source, thus allowing new designs to be undertaken with relatively high accuracy without first performing further experimental measurements of the heat flux distribution at the focal plane.

The structure of the arc needs to be spatially resolved because the radiant distribution of the arc is not spatially uniform in energy density (Spring et al.; Davidson and Dirac; Newport; Anon.). Accounting for these effects will potentially increase the accuracy over previously reported analyses, which have assumed a uniformly distributed light source with radiation issuing from the surface of a sphere (Petrasch et al., 2007; Li et al., 2011), a cone (Alxneit and Dibowski, 2011) or within the volume of a cylinder with specified angular distribution (Krueger, 2012; Bader et al., 2015). Since the final prediction of heat flux distribution at the target is strongly sensitive to the original assumptions of the energy distribution of this light source, there is a need to evaluate and compare the accuracy of a model assuming a uniformly radiant volume source and a model based on the measured energy distribution of the arc, which is non-uniform.

The details of shape and dimensions of the arc are also important, because any error in the assumptions of the shape and dimensions of the arc will be amplified by the reflector, resulting in larger errors in the prediction of the heat flux distribution at the focal plane (Rehn, 2004). Although the mathematical relations between an extended source and its image from an elliptical reflector on the secondary focal plane has been derived by Rehn (2004), the error of this analytical solution is yet to be quantified by comparison with experimental data. Petrasch et al. (2007) have also numerically analyzed the effect of arc dimension on the transfer efficiency of the elliptical reflector, while Krueger (2012) has assessed the influence of arc geometry and dimension on the transfer efficiency and flux non-uniformity. However, despite their value, these assessments also have their limitations, because a better performance in transfer efficiency does not necessarily coincide with a better performance in non-uniformity. Hence there is a need to directly compare the assumed and measured intensity

distribution of the arc, together with the equivalent values of heat flux distribution at the focal plane to provide a more robust and detailed assessment of the model's performance. Therefore, one aim of the present paper is to evaluate the sensitivity of the assumed size, shape and energy distribution of the arc on the reflected heat flux profile using a ray-tracing simulation.

Additionally, a detailed measurement of the arc profile is critical, because different types or designs of arc lamps typically generate different profiles of the arc source (Spring et al.; Davidson and Dirac; Newport; Anon.). Although the lamp manufacturers generally report the half-width for the profile of radiant intensity of the arc averaged from various lamps (Anon.), it is impossible to determine the full shape of the profile from this data alone. Therefore, another aim of the present paper is to accurately measure the profile of the light source from a metal halide lamp. For the details of a model to be applicable to other designs using the same model of lamp, it is also necessary to assess the extent to which the arc profile varies from one lamp to another. Hence a further aim is to quantify the lamp-to-lamp variations in the arc profile for the same model of lamp.

An accurate measurement of the heat flux profile at the second focal plane (i.e. the position of the target) is also required for reliable validation of the final output from any model, such as the Monte-Carlo ray-tracing model. Although the measurement of heat flux at the focal plane has been reported in the literature (Petrasch et al., 2007; Krueger, 2012; Alxneit and Dibowski, 2011), no heat flux measurements have been reported together with the measurement of the arc profile for both the model input and output. Therefore, an important aim of the present paper is to assess the influence of various assumptions about the size, the shape and the energy distribution of the arc on the accuracy with which the heat flux distribution at the target is predicted, as compared to measurements.

2. Methodology

2.1. Solar simulator system

A metal halide discharge arc lamp, HMI 6000, with an electrode separation of 23 mm was chosen for the current study, as is illustrated in Fig. 1. The model of the ballast and ignitor for the lamp are ARRI 6 kW CB, and Walter Bauch 907 respectively. 50 Hz AC power was supplied to the lamp. The spectral properties of the metal halide lamp have been reported by the Osram company (Dong et al., 2012), and also measured by our group (Dong et al., 2015), which shows that the spectral irradiance of the metal halide lamp is a closer match to that of the sun, as compared to the xenon arc lamp, with a deviation of no more than 200% over the range of 350–900 nm (Dong et al., 2015). The elliptical reflector, shown in Fig. 1, has a focal length of 3 m and is made of aluminium alloy 1050, with a Physical Vapour Deposition (PVD) coating comprising alumina and silica, following that used by PSI (Petrasch et al., 2007).
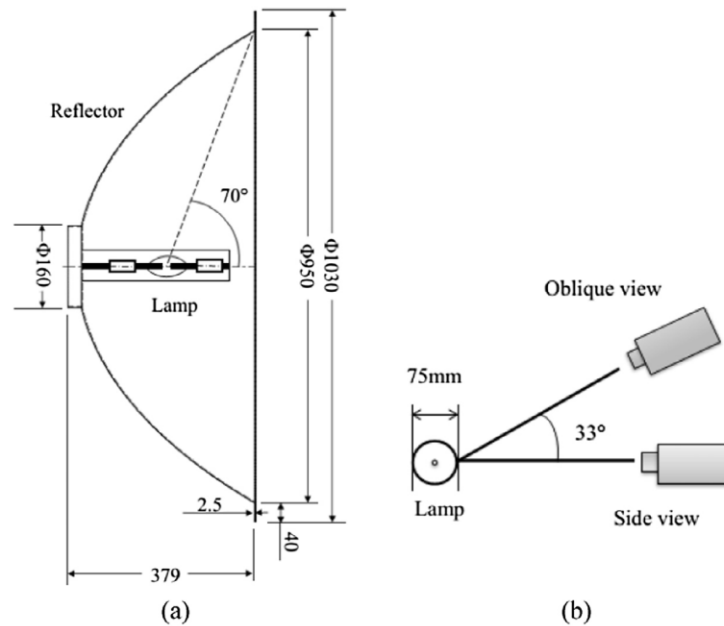
Fig. 1. (a) Cross section of the elliptical reflector reproduced from an earlier design (Petrasch et al., 2007), coupled with the metal halide lamp. Dimension is in mm. (b) Front view of the discharge arc lamp, with two cameras aligned at two different orientations for the measurement of arc profile.

2.2. Measurement of the arc

The spatial distribution of the intensity of light emitted from the radiant source was measured by imaging the arc from the lamp, using two cameras: MegaPlus E2020 and AndoriStar, DH734-18H-13. As is shown in Fig. 1(b), the side view was 33° apart from the oblique view, and both measurements were performed without the presence of the elliptical reflector. The measurements started at least 2 min[1] after the lamp was ignited to ensure that the arc was stabilized. Six hundred frames of the arc were recorded over 60 discharge cycles, which is sufficient to provide an unbiased average. The integration time for each frame is 10 μs, and the phase of each image was determined from the knowledge of the 100 Hz discharge frequency of the lamp (twice the 50 Hz AC power) (Dong et al., 2015) and that of the framing rate of the cameras (3.135 Hz). To characterize the individual differences of the metal halide HMI 6000 W lamps, we also measured and compared the profiles of the arc from another 5 lamps of the same model using the Andor ICCD camera.

2.3. Measurement of the concentrated heat flux

Among many methods of heat flux measurement (Petrasch et al., 2007; Krueger, 2012; Kaluza and Neumann, 2001; Ballestrín et al., 2006; Hager et al., 1991), a reliable technique for planar heat flux measurement is

via a combined measurement of a CCD camera and a heat flux sensor (Petrasch et al., 2007; Krueger, 2012; Craig, 2010; Lovegrove and Stein, 2012). A Lambertian target, which is a water-cooled aluminium panel that has been plasma coated with alumina, was placed at the focal plane of the elliptical reflector. The heat flux distribution was acquired by imaging the focal plane using a 1600×1200 pixels Mega-plus camera. The Lambertian target was then removed, a water-cooled circular foil heat flux transducer TG1000-1 (Vatell Corporation), with a range of 0–3 MW/m^2 and an accuracy of ±3%, was positioned at the centre of the focal plane to measure the absolute heat flux. The ratio of the absolute heat flux and the average pixel intensity in the corresponding area in the image was defined as the conversion factor, which was used to convert the CCD image into an absolute heat flux image as is shown in Fig. 6.

2.4. The Monte-Carlo ray-tracing model

A ray-tracing model of the radiation from the lamp, reflected by a closely-coupled elliptical reflector was developed with the commercial code *TracePro*®. The surfaces of lamps, elliptical reflectors and the focal plane were each modelled as a compound non-uniform rational b-spline (NURBS) surface (Tracepro User's Manual 7.3, 2012). The material properties of the reflector were taken to be those of polished aluminium, while the radiation source was modelled as a radiometric flux with a Lambertian-type angular distribution. A comparison of the Lambertian angular distribution with the measured data from the manufacturer is shown in Fig. 2. The area covered by the two

---

[1] Note that the need for 2 min start-up time reported here supersedes our earlier conference paper (Dong et al., 2013), which incorrectly reported this value as 30 s.
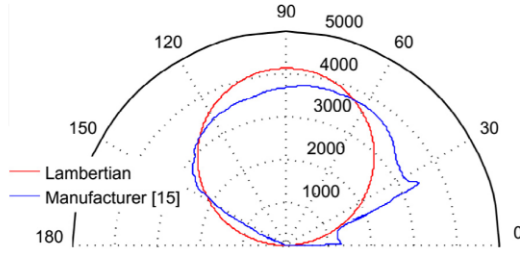
Fig. 2. Probability density function of the angular emission distribution of the lamp relative to the lamp axis for the metal halide lamp provided by the lamp manufacturer (Anon.), and Lambertian-type angular emission distribution adopted in the current paper.

curves in Fig. 2 is the same to keep the total energy equivalent. The difference σ between the Lambertian angular distribution and that reported by the manufacturer is defined in Eq. (1):

$$\sigma = \frac{\int_0^\pi \left| \frac{(I_{Lamb}(\theta) - I_{Manuf}(\theta))}{I_{Manuf}(\theta)} \right| d_\theta}{\pi - 0},\tag{1}$$

where $I_{Lamb}(\theta)$ is the radiant intensity of Lambertian distribution at angle θ, $I_{Manuf}(\theta)$ is the radiant intensity at angle θ reported by the manufacturer. The assumption of a Lambertian angular distribution can be seen to match the measured angular distribution of the lamp, with a difference of 17.3%.

The model employs the Monte-Carlo method, in which rays are directed randomly from a specified surface source, without making any assumptions of the order in which objects and surfaces will be intersected. The optical flux associated with each ray is tracked, accounting for the specular reflection of the aluminium reflector with a 95% reflectance, following the bi-directional reflectance distribution function (BRDF) (Nicodemus, 1965) as is shown in Eq. (2). The reliability of the simulation depends on the use of a statistically significant number of rays (Tracepro User's Manual 7.3, 2012).

$$N_{ref} = N_{inc} \int_{\Delta\Omega} BRDF \cos\theta_{inc} d\Omega_{inc},\tag{2}$$

where N_{ref} is the reflected power which obeys the law of reflection, N_{inc} is the incident power, Ω_{inc} is the solid angle of the incident power, the range of which is determined by the surface curvature of the reflector, θ_{inc} is the incident angle from the normal to the incident location. The BRDF model is a quasi-inverse-power-law model, known as the ABg model, as is shown in Eq. (3) (Tracepro User's Manual 7.3, 2012).

$$BRDF = \frac{A}{B + |\vec{\beta} - \vec{\beta_0}|^g},\tag{3}$$

where $A = 0.0025$, $B = 0.001$ and $g = 1.8$ are empirical constants (Tracepro User's Manual 7.3, 2012), β_0 is a projection onto the surface of the unit vector r_0 in the specular direction, β is a projection onto the surface of the unit

vector r in the reflecting direction, and the magnitude of their difference is the variance of BRDF.

In the results presented hereafter, the total radiant energy from each 6 kW metal halide lamp was considered to be 4.5 kW, accounting for 10% ohmic loss from the foil and electrodes and a 15% heat loss from the bulb (OSRAM, 2011). The arc of the lamp was modelled as a series of concentric layers, details of which are shown in Section 4.3, each layer providing radiation from its surface with Lambertian angular distribution. Each surface is also fully transparent to light emitted from another surface source. The characteristic dimensions of the elliptical reflector established in the model is the same with those shown in Fig. 1. An optically transparent plane was placed at the focal area to display the heat flux through that area.

3. Experimental results

3.1. Spatial profile of the discharge arc

Fig. 3 presents four instantaneous images of the arc from the metal halide lamp at different phases of a cycle. Phase 0 is defined as the moment with the lowest radiant intensity. Fig. 3 reveals that the shape of the arc approximates that of a cylinder during the first three phases of the cycle (Fig. 3(a)–(c)), when the intensity is also the brightest. However, as the intensity begins to decrease, the arc becomes more elliptical in shape and approaches being spherical for the outer layers. The shape and brightness of the arc varies with the discharge cycles because the metal halide lamp employed 50 Hz AC power supply (Dong et al., 2015). In contrast, the discharge from a xenon
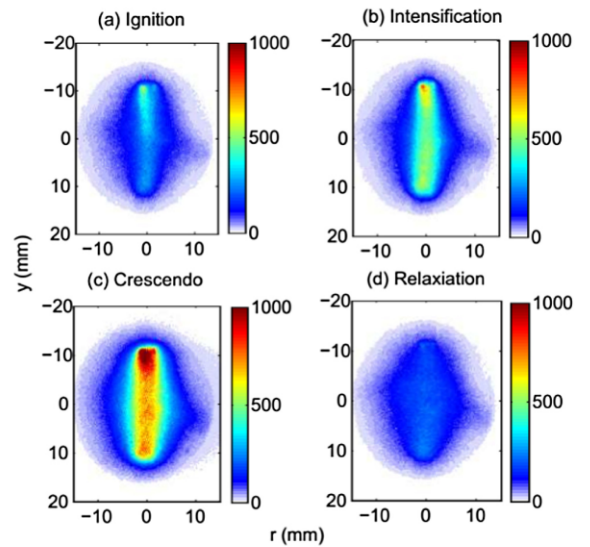

Fig. 3. Transient evolution of the arc intensity distribution through a discharge cycle (0.01 s), with the phase being (a) 36°, (b) 144°, (c) 216° and (d) 324°. The integration time of each image is 10 μs. The colour-bars are in arbitrary unit. (For interpretation of the references to colour in this figure legend, the reader is referred to the web version of this article.)

arc lamp is much more stable because they are supplied with the DC power through an AC–DC rectifier (Dong et al., 2015). Though the arc varies with time in both shape and intensity during a discharge cycle, the present work is limited to the time-averaged profile of the arc. Because though the time-averaged properties of the light source may be insufficient for those cases in which the residence time of certain reacting species is comparable with a discharge cycle, they are sufficient for those applications in which the residence time of reactants in the solar cavity receiver is much longer than a discharge cycle (Wegner et al., 2006; Chueh et al., 2010). Therefore, it is common to assess only the time-averaged profile of the arc (Petrasch et al., 2007; Krueger, 2012; Craig, 2010; Alxneit and Dibowski, 2011; Li et al., 2011).

Fig. 4(a) and (b) presents the time-averaged profile of the arc, viewed from two azimuthal directions, 33° apart, both averaged from 60 discharge cycles. It can be seen that the profiles viewed from two directions exhibit the same shape, and very similar in light intensity and energy distribution. In addition, both of them are asymmetric, with the profiles bending to the right side. This is due to the gravity effect of the arc, as the right side was facing the ground during the measurement. Fig. 4(c) shows the radial profiles of the arc from Fig. 4(a) and (b). It can be seen in Fig. 4(c) that the maximum difference between the profiles from the side view and the oblique is 13%, while the average difference is 3.3%. Hence the time-averaged image from a single viewing direction is considered to be representative of those from all directions. Therefore, the time-averaged image from the side view was used to resolve the structure of the arc.

3.2. Lamp-to-lamp variation in radiant intensity

Fig. 5 presents the radial profiles of 6 different lamps at the mid-point through the arc, i.e. at $y = 0$ of Fig. 4. It can
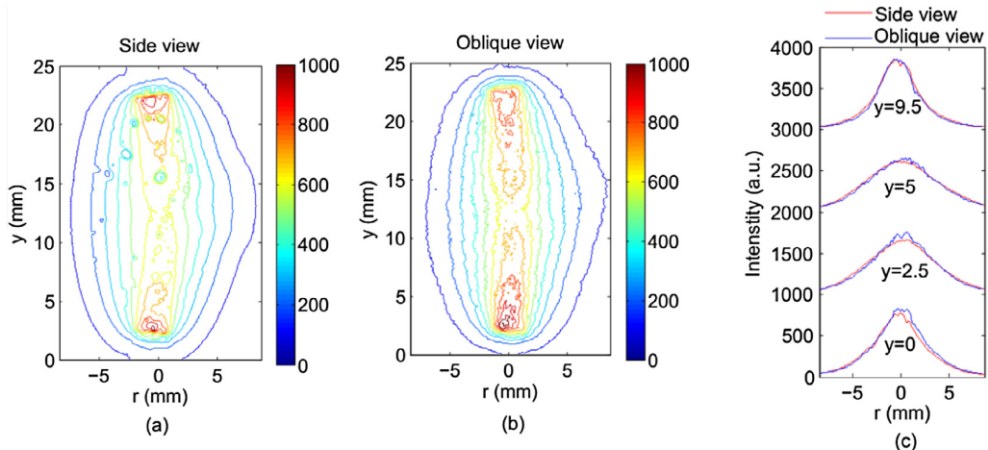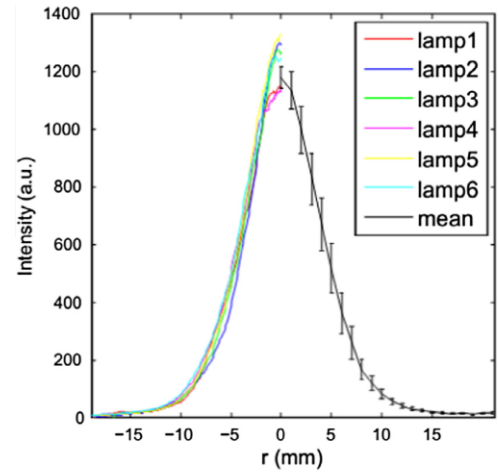

Fig. 5. Radial profiles of the arcs of six different lamps of the same model through the mid-point of the arc. Profiles shown on the left side are those from 6 lamps respectively, and that shown on the right side is the arithmetic average of the 6 profiles. Error bars on the right side are the RMS of the 6 profiles about the mean value.

be seen that while different HMI 6000 lamps exhibit very similar profiles of the arc they do have some lamp-to-lamp variation. In the present work, the variation is defined as the standard deviation relative to the arithmetic average, i.e.

$$v = \sqrt{\frac{1}{n}\sum_1^n (I_i - \bar{I})^2} \Big/ \left(\frac{1}{n}\sum_1^n I_i\right), \qquad (4)$$

where I is the radiant intensity of the arc.

It was found that the variation of peak intensity is 8.6%, and that of mean intensity and half-width are 2.2% and 7.2% respectively. The half-width is defined as the radial distance between the position of the peak intensity and that

Fig. 4. (a) Time-averaged spatial distribution of the arc from the side view as is illustrated in Fig. 1b; (b) an oblique view obtained from 33° relative to the side view as is illustrated in Fig. 1b; and (c) the radial profiles of two views, red line for the side view, blue line for the oblique view. The contour is averaged from 60 discharge cycles, with an integration time of 10 μs for each frame. (For interpretation of the references to colour in this figure legend, the reader is referred to the web version of this article.)

of half of the peak intensity. In addition, the measured half-width to arc length ratio is 0.256, while that provided by the manufacture for average illuminance of the metal halide lamps is 0.262 (Anon.). This means that the current measurement agrees well with the manufacturer's data for the profile of the arc. These values can be used to assess the uncertainty of the application of the current measurements to calculate the performance of other designs with the same model of lamp. However, new measurements of the arcs of different models and/or type of lamps are required to assess the extent to which their arcs differ from those reported here. Nevertheless, the current methodology is expected to be more widely applicable to other light sources.

3.3. Heat flux at the focal plane

Fig. 6 presents the measured heat flux distribution at the focal plane. It can be seen that the distribution of the heat flux on the focal plane is approximately radially symmetrical, except that the shape of flux profile at the top-left of Fig. 6 is a little deformed. Potential causes for this are asymmetries in the arc, departure from a purely spherical shape of the bulb and the presence of a metal wire outside the bulb that cause a shadowing effect. The total energy within the area of 95×95 mm is 0.71 kW, with a maximum heat flux of 0.112 MW/m^2. This means the overall transfer efficiency of the 6 kW Metal Halide Lamp to the 95×95 mm target is 11.8%. This relatively low transfer efficiency results from a 10% ohmic loss from the foil and electrodes of the lamp, a 15% heat loss from the bulb
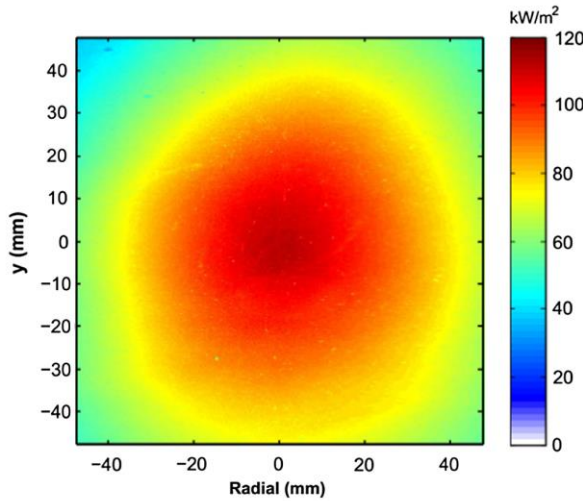

Fig. 6. Time-averaged heat flux measured at the focal plane of the elliptical reflector by calibrating a CCD image with a heat flux gauge.

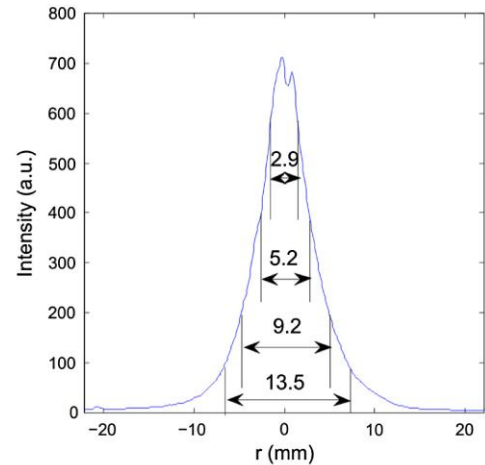Fig. 8. Cross-sectional profile of the arc, averaged from $y = 0$–11 mm in Fig. 4a, superimposed on the dimension of the contours.
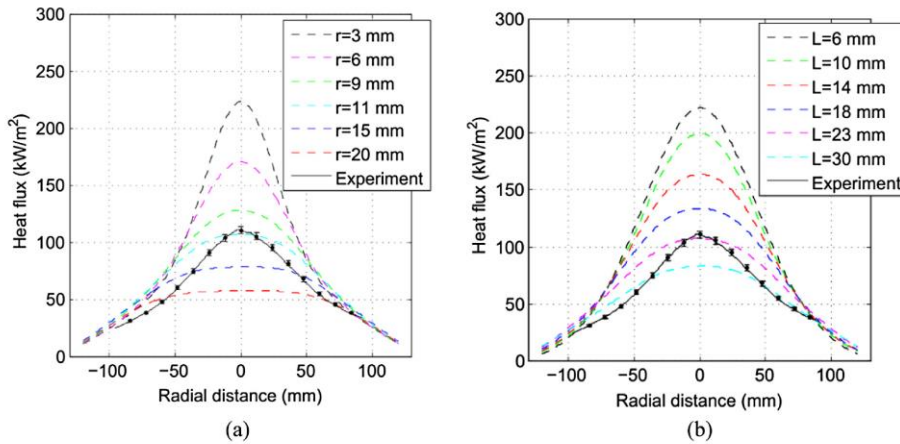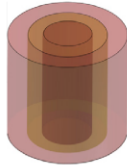

Fig. 7. Measured heat flux at $y = 0$ of Fig. 6 compared with simulated heat flux profiles of a metal halide 6000 W lamp with different assumed cylindrical arc dimensions, namely (a) the radius is varied at constant $L = 23$ mm and (b) the length is varied at constant $r = 11$ mm.

Table 2

Details of the models of the arc, assuming coaxial cylinders, concentric monopole spheres and dipole spheres, all with a total radiant power from the arc of 4500 W. The length of all cylindrical layers is 23 mm. Fluxes are calculated through the focal plane within an area of 240 mm in diameter.

Pixel intensity of concentric arc (a.u.)	Diameter of the arc layer (mm)	Radiant power input (%)	Contribution to average flux (%)		
			Coaxial cylinders of 23 mm long	Concentric monopole spheres	Concentric dipole spheres[a]
600	2.9	36.6	39.35	38.6	39.36
500	4.3	14.8	15.78	15.61	15.91
400	5.2	10.36	10.98	10.92	11.12
300	7.8	8.12	8.41	8.56	8.64
200	9.2	8.12	8.27	8.54	8.52
100	13.5	7.42	7.03	7.65	7.05
50	16	7.6	6.78	7.26	6.62
10	30	4	2.2	1.98	1.92
5	41	3	1.17	0.84	0.85
Total		100	100	100	100[b]

[a] For the case of the dipole spheres, the diameter of each arc layer is the same for each of the two poles. The radiant energy input shown is for the total dipole, hence that for each sphere is half of this value. The distance between the dipoles is 8 mm.

[b] The sum of the contribution to the average flux from individual layers may not exactly equal that from the multilayers due to rounding errors. This note also applies to Tables 3–5.

Table 3

Details of coaxial cylinders and concentric monopole spheres model 1. The total radiant power from the arc is 4500 W and length of all cylindrical layers is 23 mm. Fluxes are calculated through the focal plane within an area of 240 mm in diameter.

Pixel intensity of concentric arc (a.u.)	Diameter of the arc layer (mm)	Radiant power input (%)	Contribution to average flux (%)	Shape of layer
600	2.9	36.6	39.34	Cylinder
500	4.3	14.8	15.77	Cylinder
400	5.2	10.36	11.06	Cylinder
300	7.8	8.12	8.34	Cylinder
200	9.2	8.12	8.16	Cylinder
100	13.5	7.42	6.89	Cylinder
50	16	7.6	7.61	Sphere
10	30	4	1.96	Sphere
5	41	3	0.9	Sphere
Total		100	100	Compound

Table 4

Details of coaxial cylinders and concentric monopole spheres model 2. The total radiant power from the arc is 4500 W and length of all cylindrical layers is 23 mm. Fluxes are calculated through the focal plane within an area of 240 mm in diameter.

Pixel intensity of concentric arc (a.u.)	Diameter of the arc layer (mm)	Radiant power input (%)	Contribution to average flux (%)	Shape of layer
700	1.2	9.79	10.71	Cylinder
550	3.6	30.6	32.84	Cylinder
450	4.6	9.9	10.55	Cylinder
350	6	12.13	12.79	Cylinder
250	7.4	10.17	10.58	Cylinder
150	10.8	12.72	12.25	Cylinder
50	16	7.6	7.49	Sphere
10	30	4	1.94	Sphere
5	41	3	0.86	Sphere
Total		100	100	Compound

Table 5

Details of the compound models of coaxial cylinders and concentric spheres (dipole and monopole). The total radiant power from the arc is 4500 W and length of all cylindrical layers is 23 mm. Fluxes are calculated through the focal plane within an area of 240 mm in diameter.

Pixel intensity of concentric arc (a.u.)	Diameter of the arc layer (mm)	Radiant power input (%)	Contribution to average flux (%)	Shape of layer
600	2.9	36.6	40.25	Dipole[a]
500	4.3	14.8	15.5	Cylinder
400	5.2	10.36	10.79	Cylinder
300	7.8	8.12	8.27	Cylinder
200	9.2	8.12	8.15	Cylinder
100	13.5	7.42	6.74	Cylinder
50	16	7.6	7.38	Sphere
10	30	4	2	Sphere
5	41	3	0.86	Sphere
Total		100	100	Compound

[a] Diameter of arc layer for dipole spheres shown in this table is for each of the two poles, the radiant input for each of the dipole is half the value as is shown in the table. Distance between the dipoles is 8 mm.

(OSRAM, 2011), a capturing angle of 220° over the 360° source (Fig. 1), a 5% heat loss to the reflector and departure of the shape of the arc from a point source.

4. Simulation

4.1. Arc model of single layer surface source

Fig. 7 presents the sensitivity of the calculated heat flux profile to the assumed diameter and length of the arc.

This calculation was performed for the single-cylinder model of the light source, which models the arc as a single cylindrical surface with 4.5 kW radiant power. Specifically, Fig. 7(a) shows the heat flux from a cylindrical arc of various diameters at a constant length of 23 mm; While Fig. 7(b) shows heat flux from a cylindrical arc of various lengths at a constant diameter of 11 mm. The error-bar of ±3% for the experimental results comes from the accuracy of the heat flux gauge. It can be seen from Fig. 7(a) that the calculated values depend strongly on the assumed diameter

of the cylinder, with both the peak and the total flux increasing with a decrease in the diameter of the cylindrical arc, so that an arc of smaller diameter results in a higher peak flux and a smaller half-width. However, the single cylinder model does not reliably reproduce the half-width of the experimental results, so that even the case with a similar peak flux, which has an assumed diameter of 11 mm, differs from the experimental data in shape, with a difference of 55.42% in the half-width. Similarly, the intensity and profile of the calculated heat flux is also sensitive to the length of the arc, as is shown in Fig. 7(b), with longer arc predicting a lower peak flux, total flux and longer half-width as expected. However, the use of non-physical lengths is not expected to be useful because any deviations from the real dimension of the arc will result in error in the calculated heat flux. Hence the development of the model was undertaken using the actual arc length of 23 mm (distance of the gap between the two electrodes, as is shown in Fig. 4 for the present metal halide lamp.

4.2. Concentric multilayer arc model based on measurement

Hence we next consider the alternative concentric multi-layer model, in which a series of concentric layers are stratified based on the energy distribution of the real arc as is shown in Fig. 8, and their sum provides a reasonable step-wise approximation of the actual profile. The profile in Fig. 8 was averaged from radial profiles at $y = 0$–11 mm in Fig. 4(a). The dimension superimposed on the profile is the width of the contours $I = 600, 400, 200$ and 100 respectively. Due to the complexity of the shape of the arc, three alternative shapes of layer were assessed: namely coaxial cylinders, concentric monopole spheres and concentric dipole spheres, as is shown in Table 3. The case of coaxial cylinders was chosen because it can be seen from Fig. 4(a) and (b) that, the shape of some of the

contours is approximately cylindrical. The case of the sphere was chosen because the outer layers are approximately elliptical, which can be derived from the sum of a cylinder and a sphere, while some of the outer-most layers even approach being spherical directly. The case of the dipole spheres was considered because Fig. 4 also shows that the inner layers of the contours tend to be dipole in profile. The size of each layer was determined by the dimension of contours as is illustrated in Fig. 4(a), and the radiant energy of each layer was calculated from the area covered by each segment of the arc profile in Fig. 8. The details of the stratification of the arc are shown in Tables 2–5. In Tables 2–5, the contribution to the average flux is determined from the average flux from each individual layer out of that from multiple layers at a target of 240 mm in diameter.

Fig. 9 shows the simulated heat flux profiles from the three models described in Table 2, compared with the experimental results. It can be seen that all of the three concentric models differ from the experimental data, with the concentric monopole and dipole spheres resulting in larger deviations from the measurements than the coaxial cylinders model. This implies that a model of concentric layers of only one type of shape is unlikely to best simulate the discharge arc. This is consistent with the observations from Fig. 4, which shows that the contours of the arc exhibit a compound structure. For this reason, we also consider the concentric layers of compound shapes.

Three types of shape compounds were evaluated, as are shown in Tables 3–5, i.e. one compound of dipole sphere–cylinders–monopole spheres, and two different compounds of cylinders–monopole spheres. An example of one of the compounds was illustrated in Fig. 10. The difference between the models presented in Tables 3 and 4 is that,
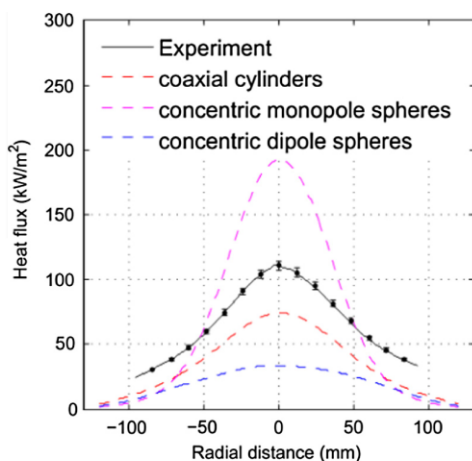

Fig. 9. Measured heat flux profile at $y = 0$ of Fig. 6 compared with simulated heat flux profiles from an arc model of coaxial cylinders, concentric monopole spheres and concentric dipole spheres, respectively.
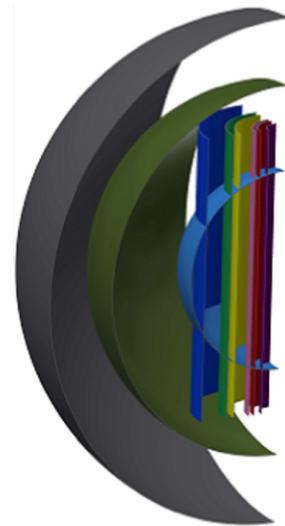

Fig. 10. Coaxial cylinder and concentric sphere compound model (quarter section) of the arc to represent the actual profile of the arc. Details of the multilayer model are presented in Table 3.

the arc was stratified into multilayers of different diameters, both based on the radial energy distribution shown in Fig. 8. It can be seen from Tables 2–5 that the contribution to the average flux from each layer is similar, but not exactly equal to the corresponding radiant power input. Besides, the contribution to average flux per radiant power input decreases with the increase of the diameter of the layer.

Fig. 11(a) presents the calculated heat flux distribution at the second focal plane of the elliptical reflector for both of the cylinder–sphere compound models. Fig. 11(b) presents the differences in heat flux between the cylinder–sphere compound models and the measurement, normalized by the local experimental data. It can be seen from Fig. 11(b) that the simulated flux matches well with the measurement within an area of 92×92 mm in the focal plane, with differences of no more than 3% in the central area. The differences on the top left of Fig. 11(b) are increased to 13% because the profile of the measured heat flux is not exactly symmetrical, as was discussed related with Fig. 6.

Fig. 12 shows that the simulated results with all the compound models agree reasonably well with the experimental results, for both the shape of the profiles and the peak flux, although in terms of half-width, the simulated profiles exhibit a deviation of within 11% from the measured profile. Fig. 12 also shows that the simulated results of cylinders–monopole spheres models are insensitive to the way the arc source is stratified for the presented two models, which indicates that the use of 9 concentric layers is sufficient for a compound model to give a reasonable approximation of the shape and energy distribution of the light source regardless of the method of stratification.

4.3. Arc model assuming a uniformly radiant volume source

The efficacy of the approach proposed previously to model the arc as a cylinder that emits radiation with
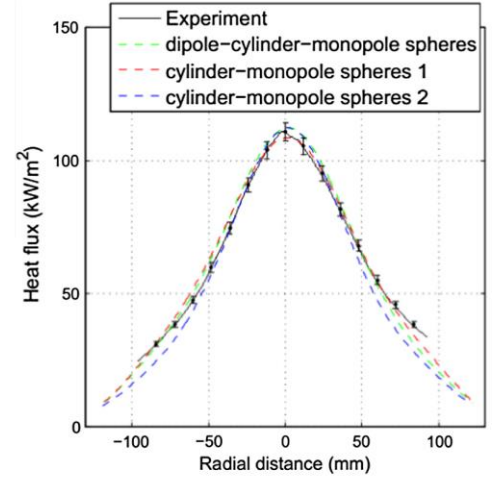

Fig. 12. Measured heat flux profile at $y = 0$ of Fig. 6 compared with simulated heat flux from three compound models of the arc as shown in Tables 3–5.

uniform energy density throughout its volume (Krueger, 2012; Bader et al., 2015), following a Lambertian-type angular distribution, was also assessed. For the current study, the solid volume is approximated as a series of concentric cylinders, each as a finite element. Assuming that the flux within the volume of the arc is a constant C, i.e.:

$$\frac{d_E}{d_V} = C, \quad (5)$$

and all the layers are equally spaced, i.e.:

$$r_i = k_0 \cdot i, \quad (6)$$

then the energy from layer i is:

$$E_i - E_{i-1} = C \cdot L \cdot \pi (r_i^2 - r_{i-1}^2), \quad (7)$$

the energy ratio between the ith layer and the first layer ε_i is
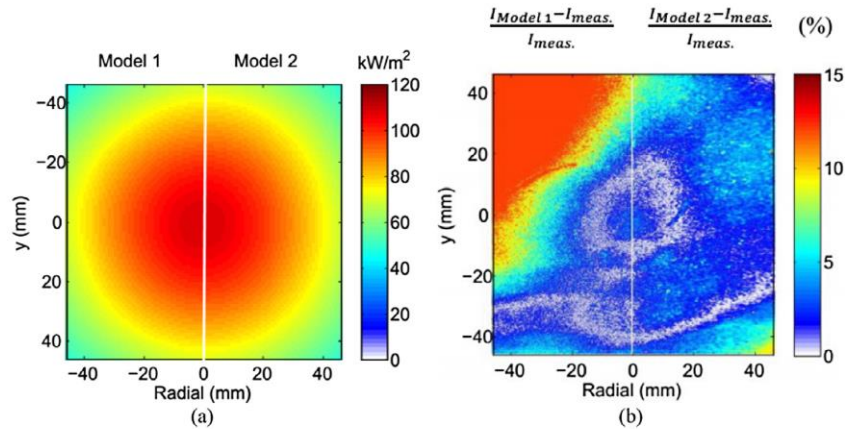

Fig. 11. (a) Irradiance map on the focal plane simulated with Monte Carlo ray-tracing method. The left side of the irradiance map is from compound model 1 shown in Table 3, and right hand side of the map is from compound model 2 shown in Table 4. (b) The difference of between the simulated heat flux and the measurement, relative to the measured local heat flux.
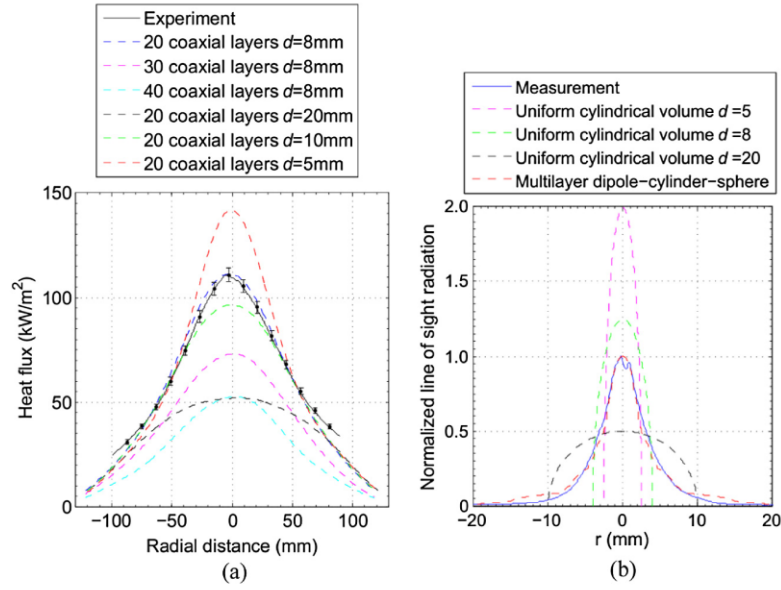
Fig. 13. (a) The measured heat flux profile compared with the simulated heat flux from models of the arc with uniform energy density and a Lambertian angular distribution. (b). Normalized line of sight radiation as measured from the arc (blue curve), averaged from $y = 0$–11 mm in Fig. 4a, and as calculated with the assumptions of arc with uniform flux distribution per volume, together with that from the multilayer model as is described in Table 5. (For interpretation of the references to colour in this figure legend, the reader is referred to the web version of this article.)

$$\varepsilon_i = \frac{(E_i - E_{i-1})}{E_1} = \frac{(r_i^2 - r_{i-1}^2)}{r_1^2} = 2 \cdot i - 1, \qquad (8)$$

the fraction of energy from the ith layer out of the total energy of the arc f_i is:

$$f_i = \frac{\varepsilon_i}{\sum_1^n \varepsilon_i} = \frac{2 \cdot i - 1}{\sum_1^n (2 \cdot i - 1)}, \qquad (9)$$

where $i = 1, 2, 3, \ldots, n$; L is the length of the arc; r_i is the radius of layer i; E_i is the radiant energy contained by the cylindrical volume with radius r_i; n is the number of layers.

This model of an arc with uniform intensity distribution was assessed for number of layers $n = 20, 30, 40$ at constant $r_n = 4$ mm, and for $r_n = 10, 5, 4, 2.5$ mm at constant $n = 20$. The total arc energy for each case is 4500 W. The results of these simulations are presented in Fig. 13(a), together with the experimental measurements. It can be seen that, while it is possible to identify a distribution that exhibits reasonable accuracy in the central region of the focal plane, the data in the outer half of the focal plane falls outside of the error bars. Besides, the predicted heat flux depends strongly on the assumed number of layers and the arc diameter. That is, for a given assumed diameter of the arc, an increase in the number of layers leads to a lower peak heat flux. Hence the peak heat flux from an ideal cylindrical volume, with an infinite number of layers, will be even lower than that from the 40 layer case reported here. Furthermore, the results from this modelling approach are also sensitive to the assumed diameter of the cylindrical volume, with a smaller assumed diameter resulting in a higher peak flux. The sensitivity of the

assumed arc diameter is shown in Fig. 13(b), which presents the measured and simulated line of sight radiation emitted from the arc. Since each of these models of the arc contains the same amount of energy as the measured arc, the area under the measured profile of the arc (blue curve) is the same with that under the other curves. The maximum diameter (20 mm) was based on the dimension needed to capture 95% of the energy within the measured arc profile, which is plausible. It can be seen that this case yields poor agreement with both the measurement for the concentrated flux (Fig. 13(a)), and with the measurement for the line of sight radiation from the arc (Fig. 13(b)). The optimal diameter with this model is somewhere between 5 and 10 mm (Fig. 13(a)). Nevertheless, none of the cases calculated with the assumption of uniform flux provides a good match with the arc profile (Fig. 13(b)). In contrast, the multilayer model assuming non-uniform flux distribution of the arc provides a very good match with the measured line-of sight arc intensity (Fig. 13(b)), which explains its better agreement with the measured concentrated flux (Fig. 12).

5. Conclusions

A single-cylinder model of the arc from the metal halide lamps, whose arc length is 23 mm, is too simplistic to provide reliable calculations of heat flux from a solar simulator. That is, even with the best case, which corresponds to an assumed arc diameter of 11 mm diameter, the predicted peak flux is 4.5% lower and the half-with is 52% greater than the measured values. Hence a more complex

model is required for accurate prediction of the heat flux from these lamps. The simulated heat flux at the focal plane is sensitive to the length and diameter of the arc in a single layer arc model, so that a smaller diameter and shorter length of the cylindrical arc results in a higher peak flux, shorter half-width and higher total flux at the target with a small aperture. While the calculations obtained by assuming the arc as an uniformly radiant volume source yield better agreement than the single layer model, the calculated flux falls outside the error bars towards the outer half of the focal zone. In addition, the calculated flux is sensitive to the assumed diameter of the cylindrical volume, for which there is no absolute definition. The limitations of this model can be explained by comparison of the measured and predicted line of sight radiation from the arc, which show that the real arc does not exhibit uniform flux density.

A model employing concentric multi-layered cylinders or spheres gives somewhat improved accuracy, it nevertheless also fails to provide good agreement with the measured heat flux. This is because the cyclical nature or the arc results in a shape that differs significantly from either a cylinder or a sphere during certain phases of the cycle.

Simulations obtained with a compound model of cylinders and monopole spheres and dipole spheres were found to give the best agreement with the measured data of the models evaluated here. The best cases falls within the error bar of the experiment for peak flux, and the departure of the half-width from the measured value is within 11%. The difference in heat flux between the measurement and simulation is less than 13% within an area of 92 mm diameter. In addition, when the concentric layers are spaced sufficiently closely to resolve the profile of the arc, which here corresponds to 9 layers, the simulated results become insensitive to the way in which the arc source is stratified.

The measured lamp-to-lamp variation in the mean radiant intensity was found to be 7.2% for the metal halide lamp HMI6000 assessed in our laboratory. However, these details will depend upon the quality of the power supply. In addition, the radiation distribution of the arc is somewhat lamp-specific, so that the present measurements cannot be expected to necessarily translate exactly to other models or types of lamp. That is, in-situ measurements of the arc for different lamps will lead to the most accurate predictions, although the proposed modelling approach is likely to be applicable.

Acknowledgments

References

Alxneit, I., Dibowski, G., 2011. Solar simulator evaluation report. In: Project SFERA, PSI and DLR.

Anon. Technology and Application. In: Metal Halide Lamps and Photo Optics, OSRAM.

Bader, R., Haussener, S., Lipiński, W., 2015. Optical design of multisource high-flux solar simulators. J. Solar Energy Eng. 137, 021012.

Ballestrín, J., Estrada, C., Rodríguez-Alonso, M., Pérez-Rábago, C., Langley, L., Barnes, A., 2006. Heat flux sensors: calorimeters or radiometers?. Solar Energy 80 1314–1320.

Chueh, W.C., Falter, C., Abbott, M., Scipio, D., Furler, P., Haile, S.M., Steinfeld, A., 2010. High-flux solar-driven thermochemical dissociation of CO_2 and H_2O using nonstoichiometric ceria. Science 330, 1797–1801.

Codd, D.S., Carlson, A., Rees, J., Slocum, A.H., 2010. A low cost high flux solar simulator. Solar Energy 84, 2202–2212.

Craig, R.A., 2010. Investigating the use of concentrated solar energy to thermally decompose limestone. Mechanical Engineering. The University of Adelaide, Adelaide, p. 369.

Davidson, M.W., Dirac, P. Mercury Arc Lamp Construction. <http://zeiss-campus.magnet.fsu.edu/articles/lightsources/mercuryarc.html>.

Dong, X., Ashman, P.J., Nathan, G.J., 2012. A high-flux solar simulator system for investigating the influence of concentrated solar radiation on turbulent reacting flows. Solar 2012. Australian Solar Council, Melbourne.

Dong, X., Ashman, P.J., Nathan, G.J., Sun, Z., 2013. Optical design of a high flux solar simulator configurable to achieve either a line or a point focus. In: Chemeca 2013, Engineering Collection, Brisbane, Australia.

Dong, X., Sun, Z., Nathan, G.J., Ashman, P.J., Gu, D., 2015. Time-resolved spectra of solar simulators employing metal halide and xenon arc lamps. Solar Energy 115, 613–620.

Ekman, B., 2014. Controlled sun' could lead to better processing of Australia's mineral exports. <http://www.swinburne.edu.au/media-centre/>.

Hager, J., Simmons, S., Smith, D., Onishi, S., Langley, L., Diller, T., 1991. Experimental performance of a heat flux microsensor. J. Eng. Gas Turbines Power 113, 246–250.

Kaluza, J., Neumann, A., 2001. Comparative measurements of different solar flux gauge types. J. Solar Energy Eng. 123, 251–255.

Krueger, K.R., 2012. Design and Characterization of a Concentrating Solar Simulator. University of Minnesota.

Kuhn, P., Hunt, A., 1991. A new solar simulator to study high temperature solid-state reactions with highly concentrated radiation. Solar Energy Mater. 24, 742–750.

Li, Z., Tang, D., Du, J., Li, T., 2011. Study on the radiation flux and temperature distributions of the concentrator–receiver system in a solar dish/Stirling power facility. Appl. Therm. Eng. 31, 1780–1789.

Lovegrove, K., Stein, W., 2012. Concentrating Solar Power Technology Principles, Developments and Applications, first ed. Woodhead Publishing Limited.

Newport, DC Short Arc Lamps & Flashlamps. Newport. <http://www.newport.com/DC-Short-Arc-Lamps-Flashlamps>.

Nicodemus, F.E., 1965. Directional reflectance and emissivity of an opaque surface. Appl. Opt. 4, 767–775.

OSRAM, 2011. Technical Information: High Power Metal Halide Lamp. In: HMI 6000 W/SE, Display/Optic Berlin.

Petrasch, J., Coray, P., Meier, A., Brack, M., Häberling, P., Wuillemin, D., Steinfeld, A., 2007. A novel 50 kW 11,000 suns high-flux solar simulator based on an array of xenon arc lamps. J. Solar Energy Eng. 129, 405–411.

Rehn, H., 2004. Optical properties of elliptical reflectors. Opt. Eng. 43, 1480–1488.

Sarwar, J., Georgakis, G., LaChance, R., Ozalp, N., 2014. Description and characterization of an adjustable flux solar simulator for solar thermal, thermochemical and photovoltaic applications. Solar Energy 100, 179–194.

Spring, K.R., Fellers, T.J., Davidson, M.W. Non-coherent light sources for confocal microscopy. Olympus. <http://www.olympu sconfocal.com>.

Tracepro User's Manual 7.3, 2012. In: Corporation of Lambda Research.

Wegner, K., Ly, H.C., Weiss, R.J., Pratsinis, S.E., Steinfeld, A., 2006. In situ formation and hydrolysis of Zn nanoparticles for H_2 production by the 2-step ZnO/Zn water-splitting thermochemical cycle. Int. J. Hydrogen Energy 31, 55–61.

CHAPTER 4

TIME-RESOLVED SPECTRA OF SOLAR SIMULATORS EMPLOYING METAL HALIDE AND XENON ARC LAMPS

Xue Dong [a,b,*], Zhiwei Sun [a,c], Graham J. Nathan [a,c], Peter J. Ashman [a,b], Dahe Gu [a,c]

[a] *Centre for Energy Technology, The University of Adelaide, SA 5005, Australia*
[b] *School of Chemical Engineering, The University of Adelaide, SA 5005, Australia*
[c] *School of Mechanical Engineering, The University of Adelaide, SA 5005, Australia*

Statement of authorship

Title of Paper	Time-resolved spectra of solar simulators employing metal halide and xenon arc lamps
Publication Status	☑ Published ☐ Accepted for Publication ☐ Submitted for Publication ☐ Publication Style
Publication Details	Solar Energy 115 (2015) 613-620

Principal Author

Name of Principal Author (Candidate)	Xue Dong		
Contribution to the Paper	Under the supervision of P. J. Ashman and G. J. Nathan and Z. W. Sun, I developed the experimental methods, performed the experiments, processed the data and wrote the manuscript.		
Overall percentage (%)	55%		
Signature		Date	01 / 09 / 2015

Co-Author Contributions

By signing the Statement of Authorship, each author certifies that:

   iv.   the candidate's stated contribution to the publication is accurate (as detailed above);

   v.   permission is granted for the candidate in include the publication in the thesis; and

   vi.   the sum of all co-author contributions is equal to 100% less the candidate's stated contribution.

Name of Co-Author	Peter J. Ashman		
Contribution to the Paper	I acted as primary supervisor for the candidate, aided in revising the manuscript and evaluating the final version of the manuscript. I give consent for Xue Dong to present this paper for examination towards the Doctorate of Philosophy.		
Signature		Date	9/9/15

Name of Co-Author	Graham J. Nathan		
Contribution to the Paper	I acted as secondary supervisor for the candidate, aided in developing of the experimental method, revising the manuscript and evaluated the final version of the manuscript. I give consent for Xue Dong to present this paper for examination towards the Doctorate of Philosophy.		
Signature		Date	10/9/15

Name of Co-Author	Zhiwei Sun
Contribution to the Paper	I am a post-doc who co-supervised the experimental campaign, aided in developing of the experimental method, performing the experiments, revising the manuscript and evaluating the final version of the manuscript. I give consent for Xue Dong to present this paper for examination towards the Doctorate of Philosophy.
Signature	Date — 01 /09 / 2o15

Name of Co-Author	Dahe Gu
Contribution to the Paper	I am a fellow PhD student, aided in performing the experiments and evaluated the final version of the manuscript. I give consent for Xue Dong to present this paper for examination towards the Doctorate of Philosophy.
Signature	Date 1 / 9 / 2o15

Time-resolved spectra of solar simulators employing metal halide and xenon arc lamps

Xue Dong [a,b,*], Zhiwei Sun [a,c], Graham J. Nathan [a,c], Peter J. Ashman [a,b], Dahe Gu [a,c]

[a] Centre for Energy Technology, The University of Adelaide, SA 5005, Australia
[b] School of Chemical Engineering, The University of Adelaide, SA 5005, Australia
[c] School of Mechanical Engineering, The University of Adelaide, SA 5005, Australia

Communicated by: Associate Editor Jan Kleissl

Abstract

The time-resolved spectra of the irradiation emitted from solar simulators employing the two types of high-intensity discharge arc lamps that are commonly used in solar simulators, i.e. metal halide (here 6 kW) and xenon arc (here 5 kW) lamps, are reported. The lamp emission was recorded by a fast-response photodiode, which reveals that the amplitude of oscillating irradiation intensity from the metal halide lamp is approximately 60% of the peak intensity, while its oscillation frequency is twice of the frequency of the AC power supply, here 100 Hz. The irradiation of the xenon arc lamp is powered by a modulated DC supply to oscillate at 300 Hz, with an amplitude that is found to be only approximately 9% that of the peak intensity. An intensified CCD camera, which was coupled with a spectrometer operating in a range of 350–900 nm, was synchronized with the lamp to provide phase-resolved spectra. The irradiation from the xenon arc lamp was found to be spectrally stable with time; while that from the metal halide lamp varies significantly throughout oscillation cycle, especially at the shorter-wavelengths of below 550 nm. All spectra were calibrated to reveal that the time-averaged spectrum of the simulator with a metal halide lamp matches the solar spectrum significantly better than does that from a xenon arc lamp. The reflecting surface of polished ellipsoidal reflector was found to reduce the intensity of selected frequency bands by up to 10%, while that from both the polished ellipsoidal reflector and conical concentrator was found to reduce the intensity in selected frequency bands by up to 20%.
© 2015 Elsevier Ltd. All rights reserved.

Keywords: Spectra; Time-resolved; Metal halide lamp; Xenon arc lamp; Solar simulator

1. Introduction

Various high powered solar simulators employing electrically powered lamps have been reported in the literature, all aiming to simulate the intensity and spectrum of the radiation from solar concentrators (e.g. from a heliostat field or parabolic dish) (Petrasch et al., 2007; Alxneit and Dibowski, 2011; Craig, 2010; Krueger, 2012; Ekman, 2014; Codd et al., 2010; Turner and Ash, 1994; Li et al., 2011). Electrical solar simulators can provide high-flux, broad-band radiation in the visible spectrum that offer the advantages for research over concentrators of real solar radiation of repeatable performance and avoiding the need to accommodate the variability of real solar radiation. However, they suffer from the disadvantages that their spectrum differs somewhat from that of the real solar resource. Nevertheless, while this trend is known, no detailed assessment of their spectral differences has been

---

* Corresponding author at: School of Chemical Engineering, The University of Adelaide, SA 5005, Australia.
E-mail address: xue.dong@adelaide.edu.au (X. Dong).

reported previously. Hence the overall aim of the present paper is to meet this need.

Table 1 presents the key specifications and capacity for all high-flux solar simulators that have been reported in the public domain. It can be seen that only two types of lamp have been used in high flux solar simulators, which are the metal halide and xenon arc lamps. The major characteristics that distinguish these two types of lamps are their different propensity to explode, which impacts both on safety and on the risk of a cascading failure; the length of the arc, which impacts on the final concentration ratio, and their radiant spectrum. The xenon arc bulbs are highly pressurized, making them vulnerable to explosion (Hight performance short arc Xenon lamp solutions, 2008). However, the metal halide lamp is less vulnerable to explosion because of their secondary containment bulb that prevents hot pieces of debris from propagating into the working environment or impacting on other lamps, even though they are also pressurized. This virtually eliminates the explosion risks to which xenon arc lamps are vulnerable (OSRAM, 2011). On the other hand, the xenon arc lamp has a shorter arc than does the metal halide lamp. This is desirable because the original dimension of the arc is magnified by the ellipsoidal reflector, so that the xenon arc lamp can generate a higher heat flux with a steeper Gaussian distribution than is possible with the long-arc metal halide lamp (Dong et al., 2013). Nevertheless, while both types of lamp offer different advantages and disadvantages, gaps remain in the understanding of their relative merits, which justifies further investigation.

The time-averaged spectra of these two types of lamp have been compared by Krueger (2012) based on measurements reported by their respective manufacturers (Xenon lamp, 2008; OSRAM, 2011). Krueger identified that the differences between the spectra from lamp and the solar spectrum at the site of Air Mass 1.5 (defined as the secant of the angle between the zenith and the sun) (Gueymard et al., 2002) are less for the metal halide lamp than for the xenon arc lamp (Krueger, 2012). However, these measurements of the spectra are from the lamps alone, without accounting for the influence of the reflective surfaces used to concentrate the radiation. In addition, no direct comparison of the spectra of these lamps either with each other or with a real solar spectrum has been reported using the same instruments and techniques. Such a direct comparison is important because every spectrometer has its specific quantum efficiency at each wavelength. This makes it difficult to reliably compare spectra measured with different spectrometers, even with the response corrected, because the correction method may vary (Williams et al., 1983). Furthermore, no details of the temporal variations in spectra are available, even though the output from these lamps is known to fluctuate at a frequency related to that of the AC power supply (OSRAM, 2011; Osram, xxxx). These fluctuations can be significant in some applications even though they may be less so in receivers involving indirect heat transfer, e.g. through tubes, or where the residence time of the reactants is long compared with these oscillations, such as for the Redox reactors with residence time of 8 s (Furler et al., 2012) and 34 s (Chueh et al., 2010), respectively. In contrast, they can be significant where gas phase reactions occur with species that are spectrally absorbing in the visible spectra, particularly where the flows are turbulent so that mixing time scales are of the order of milliseconds, and/or in reactors with short residence time. One such example is in solar driven steam-gasification reactors, which involve the spectrally active gas phase reactants of CO, CO_2 and H_2O (Burch et al., 1969) and residence time of the order of 1 s (Z'graggen et al., 2006). Another example is the recently developed concept of a hybrid solar receiver and combustor, in which a turbulent flame is directly irradiated by concentrated solar radiation during periods of moderate solar flux (Nathan et al., 2014). The residence time of a turbulent mixing flames in a typical combustor is also of the order of milliseconds and, in a laboratory–scale flame, the total residence time is in the range of 10–30 ms (Mungal et al., 1991). Because knowledge of the time-resolved spectrum is important in such applications, the aim of the present paper is to meet the need for time-resolved measurements of the spectral variations in metal halide and xenon arc lamps, as measured before and after concentration from the optical system of a high flux solar simulator.

Finally, the influence of the reflecting surface used to concentrate the radiation is yet to be reported. The lack of specific data has led to previous studies assuming that the spectrum from the concentrator is unchanged from that of the lamp as reported by the manufacturer (Krueger, 2012). However, any reflecting surface has its own specific spectral reflectivity (Bartl and Baranek, 2004; Karlsson and Ribbing, 1982). Furthermore, the reflectors for solar simulators are typically manufactured from highly polished aluminum owing to their ellipsoidal shape, the reflective properties of which can be expected to influence the spectrum more significantly than would occur with the use of perfect mirror. For these reasons it is important to quantify its influence on the spectrum of the concentrated light, even if it is small. Hence the final aim if the paper is to investigate the influence of a concentrator typical of those employed in solar simulators on the spectrum from the lamp.

2. Methodology

2.1. Solar simulators

Both types of solar simulator, one with a metal halide and one with a xenon arc lamp, were investigated in the current study. The metal halide lamp was a 6 kW long arc Osram HMI 6000 device, with a 50 Hz AC power supply; while the xenon arc lamp was a 5 kW short arc Osram XBO 5000 W/HBM OFR unit, employing a DC power supply converted from a 3 phase AC power supply using an AC–DC rectifier. Both lamps were close-coupled with

Table 1
Details of the high-flux solar simulators reported previously utilizing an array of lamps, together with polished aluminum as reflectors.

Solar simulator	Lamp type	Concentrator	Electrical power (kW/ lamp)	Number of lamps	Maximum radiant flux (MW/m^2)	Average radiant flux on target of 60 mm dia. (MW/m^2)	Radiant power in the focal area (kW)
Petrasch et al. (2007)	Xenon arc	Ellipsoidal	15	10	11	6.8	50
Krueger (2012)	Xenon arc	Ellipsoidal	6.5	7	7.3 ± 0.89	3.24 ± 0.39	9.20
Ekman (2014)	Metal halide	Ellipsoidal	6	7			
Codd et al. (2010)	Metal halide	Ellipsoidal + conical	1.5	7	0.06	4.5	5.1
Craig (2010)	Xenon arc	Ellipsoidal	5	1	10		4
Alxneit and Dibowski (2011)	Xenon arc	Ellipsoidal	6	10			
Li et al. (2011)	Xenon arc	Ellipsoidal	7	12[a]	4.27 (0.356 per lamp)		12.55
Kuhn and Hunt (1991)	Xenon arc	Ellipsoidal	23/30	1	16		
Sarwar et al. (2014)	Xenon arc	Ellipsoidal	7	1	3.58	0.1	1.64
Current design 1	Metal halide	Ellipsoidal + conical	6	1	0.7	0.1	1.2
Current design 2[b]	Metal halide	Ellipsoidal + conical	6	7	2.8	1.6	18

[a] Li et al. (2011) designed a simulator with 12 lamps, although experimental results were only reported for a single lamp.

[b] Design 2 is currently under construction. Hence for the present paper the heat flux has been estimated using a ray tracing model, which was validated by the experimental results from design 1.

an ellipsoidal reflector. That for the metal halide lamp was made from polished aluminum with a 3000 mm focal length, and physical vapour deposition (PVD) coated with alumina and silica; while that for the xenon arc lamp was made from polished aluminum with a 650 mm focal length (Craig, 2010). The concentrator for the metal halide lamp was co-aligned with an additional conical secondary concentrator made of polished stainless steel to further concentrate the radiation before reaching the focal point, as shown in Fig. 1. However, no secondary concentrator was employed for the xenon arc lamp (Craig, 2010).

2.2. Spectral measurement of solar simulator

Fig. 1 presents the experimental arrangement used to measure the spectrum from the metal halide simulator. The arrangement for the xenon arc lamp was similar, except that no secondary concentrator was used. The oscillating cycle of the radiation from both lamps was captured using a photodiode (DET210) with a broadband spectral response from 200 to 1100 nm and recorded using an oscilloscope. Light was collected through an optical fiber with a quartz collimator, and delivered to a spectrometer, which is combined with an intensified CCD camera. The numerical aperture (NA) of the optical fiber probe was 0.22. The sensitive spectral range of this detection system is 350–900 nm. The probe was mounted at a distance of 0.5 m from the focal plane of the metal halide lamp and about 1.5 m from the focal point of the solar simulator for the case of xenon

arc lamp, with the sensor oriented toward the incident simulated solar radiation for both cases. The reference solar spectrum was measured in Adelaide, by reflecting the sunlight to the fiber probe using an optical diffuse reflector with a flat spectral response within the range of 350–900 nm.

The photodiode was positioned outside the field of concentrated light and aligned normal to the principal axis of the focused light from the metal halide lamp to provide an external trigger for a DG535 signal generator, whose output was then used to trigger the spectrometer. Twenty-four phased-resolved spectral measurements, each accumulated from 50 measurements with a gate width of 0.5 ms, were collected over the 12 ms cycle. For the xenon arc lamp, an internal trigger was used to trigger the spectrometer, because the amplitude of oscillation is too weak to be externally triggered. In this way, the spectral measurement was performed over 250 consecutive frames. The measured spectral range of 350–900 nm was obtained by combining data from 5 spectral ranges, each of 175 nm.

The relative spectral response of the spectrometer was calibrated by comparing the measured solar spectrum with the Air Mass 1.5 (direct normal) reference spectrum reported by Gueymard et al. (2002) as is shown in Fig. 2a, from which a response curve of the spectrometer was acquired as is shown in Fig. 2b. (Note that small differences between the standard atmospheric condition and those in Adelaide do not affect the evaluation of relative differences between the spectral distributions of different
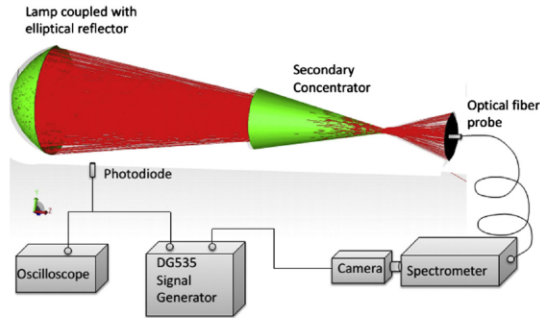
Fig. 1. Schematic diagram of the experimental arrangement, shown here with the secondary conical concentrator employed with the metal halide lamp.

configurations, even though their absolute values will differ slightly.) This response curve was applied to all the results measured with our spectrometer to obtain the corrected spectra. The direct normal solar spectrum (Gueymard et al., 2002) was used as the reference because the direct normal beam was also the component utilized in the spectra measurement of the solar simulators. It can also be seen from Fig. 2a that the sensitivity of the present detector falls sharply with wavelength through the visible spectrum, which presents data from being reported for wavelength greater than 900 nm.

2.3. Comparison of spectra of radiation from pure lamp and that reflected by concentrators

The spectral measurement was also performed of the radiation transmitted directly from the metal halide lamp and compared with that from the ellipsoidal and conical concentrators, respectively, to assess the influence of the concentrators on the spectrum. Radiation from the lamp, the ellipsoidal reflector and the conical concentrator was reflected from a Lambertian target to the optical fiber probe, which was then transmitted to a portable spectrometer (Ocean Optics USB 4000). The Lambertian

target was a square, water cooled aluminum panel of 250 mm × 250 mm in size, plasma coated with alumina, similar to those used by other groups (Petrasch et al., 2007; Krueger, 2012). This was used to provide a repeatable spectrum viewed from any angle relative to the target. Although the Lambertian surface itself has its own spectral reflectance, this spectral effect contributes equally to all measurements, so that the comparison of the relative spectral irradiance reflected by Lambertian target is valid.

3. Results and discussion

3.1. Oscillation cycle of the solar simulators

Fig. 3 presents the time resolved intensity from the two types of lamp. This shows that the frequency of the oscillation of the radiant intensity from metal halide lamp is 100 Hz, which is twice the frequency of the AC power supply, while that of xenon arc lamp is around 300 Hz. It can also be seen that the amplitude of the oscillation of the radiation intensity from metal halide lamp is about 60% of its peak value, while that of xenon arc lamp is around 9%. Hence, while the xenon arc lamp offers the advantage over the metal halide lamp in providing a steadier output, neither lamp achieves a truly steady-state output. The difference in the amplitude of fluctuations in radiation intensity can be attributed to the difference in the type of power supply. While the metal halide lamp employs AC power, the xenon arc lamp uses a DC power supply from an AC–DC rectifier. Hence, the frequency and amplitude of fluctuations from the metal halide lamp depends on the quality of the AC-power supply. Similarly, that from the xenon arc lamp depends on the type and performance of the AC–DC rectifier. Furthermore, the time-varying performance of the lamp array will also be dependant on the configuration of the power supply to the lamp array. For example, if the various phases in the power supply to each lamp of a lamp array is suitably staggered, the amplitude of variation of their combined beams will be offset, resulting in a flatter output than for the single lamp case.
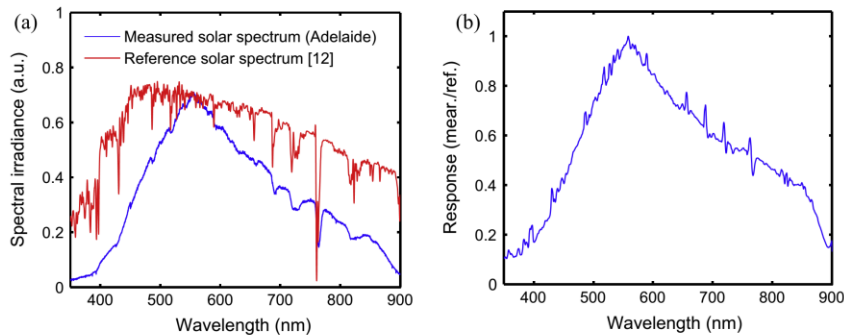

Fig. 2. (a) Measured and reference solar spectrum, arbitrary units (a.u.) for y-axis; (b) response of the spectrometer.
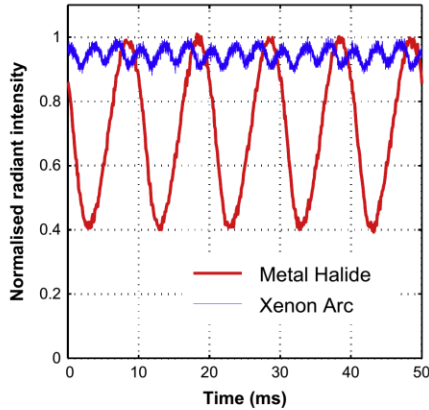
Fig. 3. Normalised radiant intensity from the metal halide and xenon arc lamps as a function of time.

3.2. Time resolved spectra from the solar simulators

Fig. 4 presents the phase resolved spectra from the solar simulator with the metal halide lamp. The red shaded curve in each subfigure represents the time averaged spectrum of the solar simulator with the metal halide lamp. Here Phase 0 was defined as the spectrum with the weakest intensity. This shows that the spectrum at Phase 0 has only one apparent peak at 860 nm, while several other peaks start to emerge at 365, 440, 540 and 580 nm for a Phase angle of 0.2π. Additional peaks at 670–770 nm then emerge for phase angle of 0.4π, after which no significant change in the distribution of spectral intensity occurs even though the intensity continues to increase from 0.4π to π. The

reverse trend is then found to occur over the phase range from π to 2π .

Fig. 5 presents the temporal evolution of the radiation in different wavebands over 1 cycle (10 ms) for the metal halide lamp. It can be seen that the radiant intensity varies through the cycle of the arc, and the magnitude of variation is dependent on the wavelength ranges. The intensity of the spectral radiation within 700–900 nm is found to double from the trough to the peak, while that in the range 550–700 nm is found to triple and that in the range 400–550 nm is found to increase by 6 times. Although light of wavelengths <400 nm exhibits the strongest variation within a cycle, it accounts for a relatively small part of the total radiation. It can also been seen that light in the range 400–700 nm dominates the broadband radiation from the solar simulator with the metal halide lamp.

The time resolved spectrum from the solar simulator with the xenon arc lamp is presented in Fig. 6a. This was obtained by setting the sampling frequency to be asynchronous with the lamp fluctuation frequency by recording 500 spectra over 50.83 s, i.e. at a frequency of 9.8367 Hz. When converted to phase-time, this leads to about 10 realisations of the 300 Hz fluctuation frequency of the xenon arc solar simulator, which can then be phase-shifted to yield a phase-average spectrum of one cycle as is presented in Fig. 6a. It can be seen from Fig. 6a that the spectrum of the concentrated radiation from the solar simulator with the xenon arc lamp is quite stable. This is attributed to its use of a DC power supply as was discussed with regard to Fig. 3. Also as shown in Fig. 3, the fluctuation in intensity of the broadband radiation from the xenon arc lamp is about 9% relative to its peak value, a similar magnitude of fluctuation was also found for each of the narrowband spectral ranges, as is shown in Fig. 6b. In contrast to the radiation from the metal halide lamp, that from the xenon arc lamp is dominated by the spectral range of 700–900 nm, with a significant contribution from the range 400–700 nm.
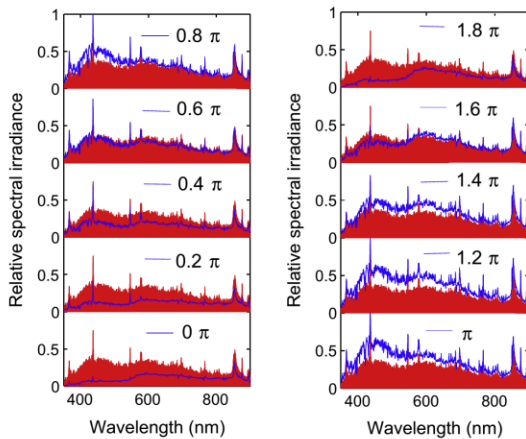

Fig. 4. Phase resolved spectra (blue lines) relative to the time averaged spectrum (red shaded curve) of the solar simulator with the metal halide lamp. (For interpretation of the references to color in this figure legend, the reader is referred to the web version of this article.)
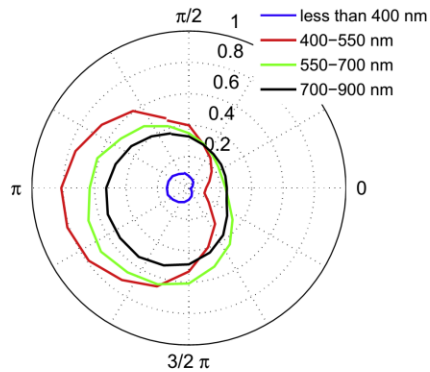

Fig. 5. Phase resolved light intensity of different wave bands of the concentrated light from the metal halide lamp.

Fig. 7a presents the time-averaged solar spectrum measured in Adelaide, calibrated to match that reported by Gueymard et al. (2002), hereafter referred to as Adelaide/ Gueymard solar spectrum. Also presented is the concentrated radiation from the metal halide and xenon arc lamps. It can be seen that the time averaged spectrum of metal halide lamp matches that of the Adelaide/ Gueymard solar spectrum significantly better than does the xenon arc lamp, mainly due to the strong radiation peaks in the 800–900 nm range from xenon arc lamp. Fig. 7b shows the spectrally resolved deviation factor by which the intensity from each of the lamps differs from the solar spectrum. This is defined as $(I_{lamp} - I_{sun})/I_{sun}$, where I_{sun} and I_{lamp} are the spectral irradiance of the sun and solar simulators, respectively. Fig. 7b shows that the deviation factor for the spectrum from metal halide lamp occurs at peaks centered at approximately 365, 435, 545, 580, 765 and 855 nm, and all have values of $(I_{lamp} - I_{sun})/I_{sun} < 2$; In contrast, the spectral irradiance of xenon arc lamp is constantly lower than that of the solar spectrum over the range 350–700 nm, yet is significantly higher over the range 760–900 nm, with $(I_{lamp} - I_{sun})/I_{sun} \sim 7$. Furthermore, the integrated value of the modulus of the

deviation $\frac{\int_{350nm}^{900nm}(I_{lamp}-I_{sun})/I_{sun}d_\lambda}{(900-350)nm} = -0.0126$ for the metal halide lamp, 3.4 times lower than the corresponding value of 0.0434 for the xenon arc lamp.

Fig. 7 also reports the manufacturers' spectra over the range 300–1600 nm. This shows that, while their data agrees well with the present measurement for the metal halide lamp, that of xenon arc lamp exhibits some differences from the current measurement. In particular, over the range $350 < \lambda < 700$ nm, the manufacturer's spectra for the xenon arc lamp reports a better agreement with the solar spectrum than does the present measurement, relative to which it is higher by an average value of 54%. Nevertheless, importantly, both measurements report the large energy spike in the range 750–900 nm for the xenon arc lamp, for which the total energy content in this range agrees to within 9.4%, although the peak value is different by a factor of 2.1. These differences in details in the
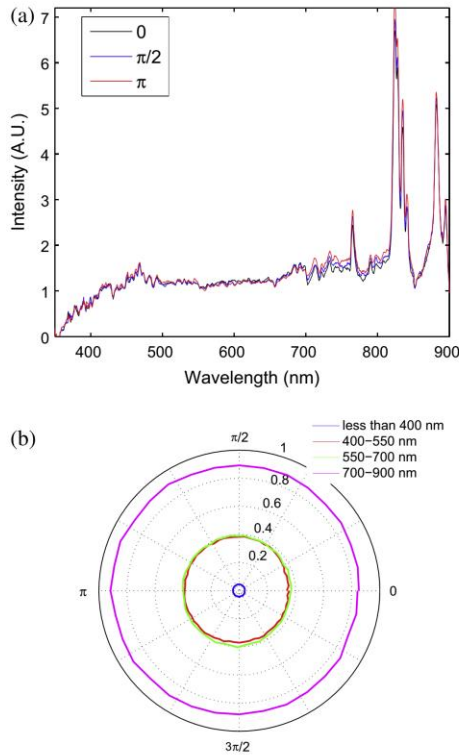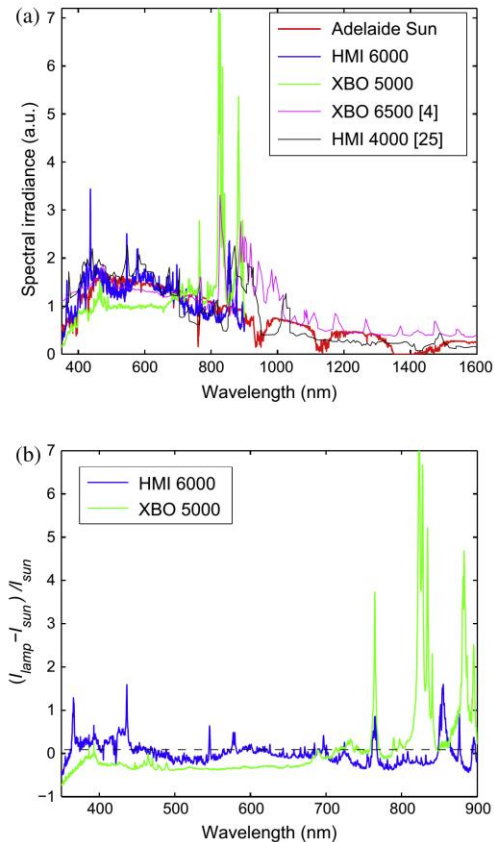

Fig. 7. (a) Measured time averaged spectra of the sun (Adelaide/ Gueymard) and of the two solar simulators (with metal halide HMI 6000 and xenon arc XBO 5000), as well as the spectra of XBO 6500 (Krueger, 2012) and HMI 4000 (Technology and Application, xxxx) reported by the manufacturer; and (b) the spectrally resolved deviation factor of the lamps from the solar spectrum.

Fig. 6. (a) Spectra of xenon arc lamp at phase 0, π/2 and π; and (b) phase-resolved intensity (a.u.) in four spectral bands integrated from (a).
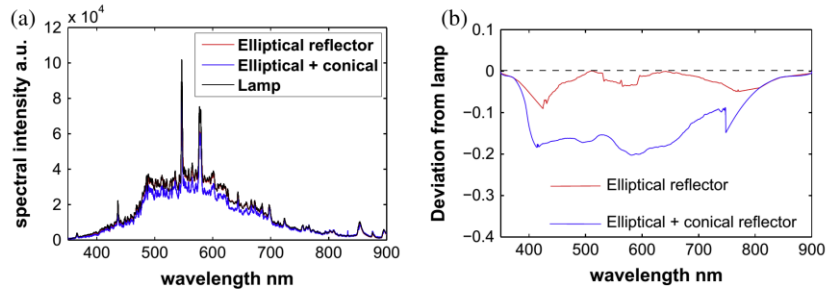
Fig. 8. (a) Time averaged spectra of the radiation from metal halide lamp, and that reflected by the ellipsoidal reflector and by the combination of the ellipsoidal reflector and conical concentrator, (raw data, i.e. without calibration). The radiation was measured after reflection by the Lambertian surface for all cases; and (b) the deviation of the spectra from the reflectors relative to that of the pure metal halide lamp, $(I - I_{lamp})/I_{lamp}$, derived from (a).

measured spectra have many potential causes that include differences in AC power quality, in lamp manufacture and in the measurement techniques. However, such differences are second order relative to the differences in the lamp type.

Given that only about 70% of the energy in the solar spectrum is within the visible range, it is also important to consider the energy in the near-infrared range. This can be done to a limited extent from the available data from the manufacturers (Krueger, 2012; Technology and Application, xxxx) which extends to 1600 nm for both the metal halide and xenon arc lamps Fig. 7a. These data suggest that the spectral radiant intensity of xenon arc lamp in the near infra-red is generally higher than the solar spectrum by a factor of about 2, which is similar to the factor by which the metal halide lamp is lower than the solar spectrum. Nevertheless, the spectrum of the metal halide lamp at around 900 nm is higher than the solar spectrum by a factor of about 2, which is consistent with our measurement. More comprehensive measurements in the near infra-red are desirable, but are beyond the scope of the present investigation.

3.3. Influence of reflectors and concentrators on the spectra from lamps

Fig. 8 presents the influence of the ellipsoidal reflector and the conical concentrator on the spectrum of pure metal halide lamp. While the differences are not large, as can be seen from the direct comparison of spectra shown in Fig. 8a, it is also non-negligible in certain spectral bands. The differences are more apparent in the plot of the spectrally resolved deviation factor, defined as $(I - I_{lamp})/I_{lamp}$, as is shown in Fig. 8b, where it can be seen that deviation of the spectrum from the original is reduced in some bands by up to 10% and 20%, respectively, for the elliptical only and for the combination of the elliptical and conical reflectors. More particularly, the ellipsoidal reflector decreases relative intensity centered at 420, 550 and 750 nm of the radiation from the metal halide lamp, while the combination of ellipsoidal reflector and conical

concentrator reduced the spectra intensity of pure lamp in the range of 400–800 nm.

4. Conclusions

It was found that the integrated deviation of the time-averaged spectrum of metal halide lamp from the solar spectrum is 3.4 times less than from the xenon arc lamp, mainly due to the strong radiation peaks in the 800–900 nm range from xenon arc lamp. The deviation of the spectrum from the metal halide lamp $(I_{lamp} - I_{sun})/I_{sun}$ is less than a factor of 2 for all wavelengths; while that of xenon arc lamp is up to a factor of 7 in the 800–900 nm range. This trend is consistent with previous understanding from manufacturer's data, although the present relative comparison is expected to be more accurate since it was performed with identical equipment. Some differences were found between the present measurements and those of the manufacturers, as is expected, due to slight differences in power supply, manufacturing details and the measuring technique. However, such differences are second order compared with differences in the lamp type.

The time-resolved measurements of the radiation intensity of solar simulators has revealed that the radiant intensity from metal halide lamp oscillates at a frequency of 100 Hz, which is twice the frequency of the AC power supply, while that of xenon arc lamp is around 300 Hz. In addition, the amplitude of the oscillation of the radiation intensity from the metal halide lamp is about 60% of its peak value, while that from the xenon arc lamp is around 9%. The difference in the amplitude of fluctuations in radiation intensity is due to the difference in the type of power supply. Hence too, while the xenon arc lamp offers a steadier radiant output than the metal halide lamp, neither lamp achieves a truly steady-state output.

The spectrum from the xenon arc lamp is more stable than that for the metal halide lamp due to its use of a DC power supply. The fluctuation in intensity of the broadband radiation from the xenon arc lamp is only approximately 9% relative to its peak value. However, the spectrum from the metal halide lamp shows that the intensity of spectral irradiance gradually increases from 0

to π, and then reverses over the phase range from π to 2π. Overall, light in the range 400–700 nm dominates the broadband radiation from the solar simulator with the metal halide lamp.

The application of concentrators can have a significant influence on the spectrum of the radiation from the lamp in selected bands, with reductions in certain wavelength by up to 10% for the elliptical reflector only and to 20% for that with both the elliptical and conical concentrators. Hence care must be taken in assuming the lamp spectrum is the same as that from the concentrator.

Acknowledgements

References

Alxneit, I., Dibowski, G. 2011. Solar Simulator Evaluation Report. Project SFERA, PSI and DLR.

Bartl, J., Baranek, M., 2004. Emissivity of aluminium and its importance for radiometric measurement. Meas. Phys. Quantities 43, 3136.

Burch, D.E., Gryvnak, D.A., Patty, R.R., Bartky, C.E., 1969. Absorption of infrared radiant energy by CO_2 and H_2O. IV. Shapes of collision-broadened CO_2 lines. JOSA 59, 267–278.

Chueh, W.C., Falter, C., Abbott, M., Scipio, D., Furler, P., Haile, S.M., Steinfeld, A., 2010. High-flux solar-driven thermochemical dissociation of CO_2 and H_2O using nonstoichiometric ceria. Science 330, 1797–1801.

Codd, D.S., Carlson, A., Rees, J., Slocum, A.H., 2010. A low cost high flux solar simulator. Sol. Energy 84, 2202–2212.

Craig, R.A., 2010. Investigating the use of concentrated solar energy to thermally decompose limestone. Mechanical Engineering. The University of Adelaide, Adelaide, p. 369.

Dong, X., Ashman, P.J., Nathan, G.J., Sun, Z., 2013. Optical design of a high flux solar simulator configurable to achieve either a line or a point focus. Chemeca 2013. Engineering Collection, Brisbane, Australia.

Ekman, B., 2014. Controlled sun' could lead to better processing of Australia's mineral exports. <http://www.swinburne.edu.au/media-centre/>.

Furler, P., Scheffe, J.R., Steinfeld, A., 2012. Syngas production by simultaneous splitting of H_2O and CO_2 via ceria redox reactions in a high-temperature solar reactor. Energy Environ. Sci. 5, 6098–6103.

Gueymard, C., Myers, D., Emery, K., 2002. Proposed reference irradiance spectra for solar energy systems testing. Sol. Energy 73, 443–467.

High performance short arc xenon lamp solutions. In: Xenon Lamp Listing, Christie. 2008. <www.projectionniste.net>.

Karlsson, B., Ribbing, C.G., 1982. Optical constants and spectral selectivity of stainless steel and its oxides. J. Appl. Phys. 53, 6340–6346.

Krueger, K.R., 2012. Design and Characterization of a Concentrating Solar Simulator. In: University OF Minnesota.

Kuhn, P., Hunt, A., 1991. A new solar simulator to study high temperature solid-state reactions with highly concentrated radiation. Sol. Energy Mater. 24, 742–750.

Li, Z., Tang, D., Du, J., Li, T., 2011. Study on the radiation flux and temperature distributions of the concentrator–receiver system in a solar dish/Stirling power facility. Appl. Therm. Eng. 31, 1780–1789.

Mungal, M., Karasso, P., Lozano, A., 1991. The visible structure of turbulent jet diffusion flames: large-scale organization and flame tip oscillation. Combust. Sci. Technol. 76, 165–185.

Nathan, G., Battye, D.L., Ashman, P.J., 2014. Economic evaluation of a novel fuel-saver hybrid combining a solar receiver with a combustor for a solar power tower. Appl. Energy 113, 1235–1243.

OSRAM, 2011. Technical information: high power metal halide lamp. In: HMI 6000 W/SE, Display/Optic Berlin.

Osram, Metal halide lamps-instructions for the use and application, in, Osram.

Petrasch, J., Coray, P., Meier, A., Brack, M., Häberling, P., Wuillemin, D., Steinfeld, A., 2007. A novel 50 kW 11,000 suns high-flux solar simulator based on an array of xenon arc lamps. J. Sol. Energy Eng. 129, 405–411.

Sarwar, J., Georgakis, G., LaChance, R., Ozalp, N., 2014. Description and characterization of an adjustable flux solar simulator for solar thermal, thermochemical and photovoltaic applications. Sol. Energy 100, 179–194.

Technology and Application. In: MetalL Halide Lamps and Photo Optics, OSRAM.

Turner, T.L., Ash, R.L., 1994. Numerical and Experimental Analyses of the Radiant Heat Flux Produced by Quartz Heating Systems. Citeseer.

Williams, A.T.R., Winfield, S.A., Miller, J.N., 1983. Relative fluorescence quantum yields using a computer-controlled luminescence spectrometer. Analyst 108, 1067–1071.

Z'graggen, A., Haueter, P., Trommer, D., Romero, M., De Jesus, J., Steinfeld, A., 2006. Hydrogen production by steam-gasification of petroleum coke using concentrated solar power—II Reactor design, testing, and modeling. Int. J. Hydrogen Energy 31, 797–811.

CHAPTER 5

THE INFLUENCE OF HIGH FLUX BROADBAND IRRADIATION ON SOOT CONCENTRATION AND TEMPERATURE OF A SOOTY FLAME

Xue Dong[1, 2, *], Zhiwei Sun[1, 3], Dahe Gu[1, 3], Graham J. Nathan[1, 3*], Peter J. Ashman[1, 2], Zeyad T. Alwahabi[1, 2], Bassam B. Dally[1, 3]

[1]Centre for Energy Technology, Schools of [2]Chemical Engineering and [3]Mechanical Engineering, The University of Adelaide, SA 5005, Australia

Statement of authorship

Title of Paper	The influence of high flux broadband irradiation on soot concentration and temperature of a sooty flame
Publication Status	☐ Published ☐ Accepted for Publication ☐ Submitted for Publication ☑ Publication Style
Publication Details	Combustion and Flame, manuscript

Principal Author

Name of Principal Author (Candidate)	Xue Dong	
Contribution to the Paper	Under the supervision of P. J. Ashman and G. J. Nathan, I developed the experimental methods, performed the experiments, processed the data and wrote the manuscript.	
Overall percentage (%)	55%	
Signature	Date	09/09/2015

Co-Author Contributions

By signing the Statement of Authorship, each author certifies that:

    vii.   the candidate's stated contribution to the publication is accurate (as detailed above);

    viii.   permission is granted for the candidate in include the publication in the thesis; and

    ix.   the sum of all co-author contributions is equal to 100% less the candidate's stated contribution.

Name of Co-Author	Peter J. Ashman	
Contribution to the Paper	I acted as primary supervisor for the candidate, aided in developing of the experimental method and evaluating the final version of the manuscript. I give consent for Xue Dong to present this paper for examination towards the Doctorate of Philosophy.	
Signature	Date	9/9/15

Name of Co-Author	Graham J. Nathan	
Contribution to the Paper	I acted as secondary supervisor for the candidate, aided in developing of the experimental method, revising the manuscript and evaluating the final version of the manuscript. I give consent for Xue Dong to present this paper for examination towards the Doctorate of Philosophy.	
Signature	Date	10/9/15

Name of Co-Author	Zhiwei Sun
Contribution to the Paper	I am a post-doc who co-supervised the experimental campaign, aided in developing of the experimental method, performing the experiments, revising the manuscript and evaluating the final version of the manuscript. I give consent for Xue Dong to present this paper for examination towards the Doctorate of Philosophy.
Signature	Date 01/09/2015

Name of Co-Author	Zeyad Alwahabi
Contribution to the Paper	I acted as co-supervisor for the candidate, aided in evaluating the concept of the study and evaluating the final version of the manuscript. I give consent for Xue Dong to present this paper for examination towards the Doctorate of Philosophy.
Signature	Date sept 17, 2015

Name of Co-Author	Bassam B. Dally
Contribution to the Paper	I am a professor who co-supervised the research project, aided in evaluating the concept of the study and evaluating the final version of the manuscript. I give consent for Xue Dong to present this paper for examination towards the Doctorate of Philosophy.
Signature	Date 10/9/15

Name of Co-Author	Dahe Gu
Contribution to the Paper	I am a fellow PhD student, aided in performing the experiments and evaluating the final version of the manuscript. I give consent for Xue Dong to present this paper for examination towards the Doctorate of Philosophy.
Signature	Date 1/9/2015

The influence of high flux broadband irradiation on soot concentration and temperature in a sooty flame

Xue Dong[1, 2, *], Zhiwei Sun[1, 3], Dahe Gu[1, 3], Peter J. Ashman[1, 2], Zeyad T. Alwahabi[1, 2], Bassam B. Dally[1, 3], Graham J. Nathan[1, 3, *]

[1]Centre for Energy Technology, [2]School of Chemical Engineering and [3]School of Mechanical Engineering, The University of Adelaide, SA 5005, Australia
*Email: xue.dong@adelaide.edu.au;
graham.nathan@adelaide.edu.au

Abstract: This paper reports the first set of measurements of the influence of simulated concentrated solar radiation (CSR) on the soot volume fraction and temperature in a laminar diffusion ethylene flame. Broad-band radiation that closely approximates the solar spectrum was produced with a metal-halide lamp configured in a series of three optical concentrators to achieve fluxes of up to 0.45 MW/m^2 in a focused area of 80 mm diameter. The radiation was used to irradiate an entire Santoro-type laminar flame of 64 mm in length, where the soot volume fraction and flame temperature were measured using planar laser-induced incandescence (PLII) and two-line atomic fluorescence (TLAF), respectively. The results show that the simulated concentrated solar radiation significantly influences the evolution of soot on the fuel-rich side of the flame. It causes the total volume of soot within the flame to increase by up to 55%, the soot inception to be translated upstream by 7% of the flame length, and the consumption rate of soot in the radial direction to increase by an average value of 54% for heights greater than 10 mm above the burner. The spatially-average flame temperature in the radial direction was also found to increase by about 8% in most of the downstream locations.

Keywords: *combustion-radiation interactions, concentrated solar radiation, soot volume fraction, temperature*

1.   Introduction

Hybrids of concentrated solar thermal energy and fossil-fuelled technologies are receiving growing attention because the combination of the two energy sources offers lower emissions of carbon and other pollutants than pure fossil fuels, lower cost than pure solar thermal energy, and continuous supply [1, 2]. Various types of hybrid concepts have been proposed, e.g. preheating the feed water with the low grade solar energy [3], regenerating CO_2 solvents for the carbon capture and storage process [4], preheating the combustion air in a Brayton cycle [5-7], combining oxy-fuel combustion with solar thermal in a power cycle [8]. However, all of these concepts employ stand-alone solar receivers and combustors. There is potential to further reduce capital cost by sharing the infrastructure employed to harvest both energy sources [2]. Mehos *et al.* [9] proposed one approach with which to reduce heat losses from a solar receiver and a combustor in a hybrid system by mounting a combustor directly onto the back of a solar receiver. More recently, Nathan *et al.* [2, 10, 11] have been developing an alternative approach with which to fully combine a combustor and a solar cavity receiver into a single device. This offers the potential for significant savings from reduced infrastructure investment and reduced start-up and shut-down losses [2]. Importantly, this direct integration of the two energy sources also results in conditions in which the flame is directly irradiated by high flux solar radiation. However, the influence on a flame of high-flux radiation, whose spectrum approximates the solar spectrum, is poorly understood and has not been reported previously.

Medwell *et al.* [12] identified that a flame can absorb radiation through the unburned fuel, the combustion products (such as CO_2 and H_2O) and intermediates (such as radicals, molecules and soot). Among these species, soot is the most efficient radiation receptor due to its strong absorption coefficient in a broadband spectral region from visible to near-infrared. Nevertheless, the relative significance of these different species and their role in a sooting flame has yet to be reported. Indeed, to our knowledge, the relevant investigation is that of Medwell *et al.* [12], who demonstrated that CO_2 laser radiation at 10.6 μm with a fluence of 4 MW/m^2 can approximately double the peak concentration of soot in a laminar ethylene/air diffusion flame, and translate the

61

soot layer towards the oxidising side of the flame. However, the work was undertaken with a coherent light of single excitation wavelength and irradiating on a small area of the flame (~ 5 mm in diameter) [12], while the CSR is broadband and would irradiate a large area of flames in a practical hybrid device. Therefore, new measurements are needed to assess the influence of radiation on a sooty flame using high-flux broadband solar irradiation of the whole flame.

The influence of CSR on soot oxidation, despite its importance in affecting the emission of soot as pollutant, has not yet been reported to our knowledge. For example, the most relevant previous investigation by Medwell *et al.* [12] was performed by irradiating and measuring the upstream region of flame, while the consumption of soot occurs mostly in the vicinity of the flame tip. Therefore, the present work also aims to assess the influence of high-flux radiation on soot oxidation through the measurements of both soot volume fraction and temperature throughout a flame that is entirely irradiated by high-flux broadband radiation.

Additionally, no previous measurements of both flame temperature and soot volume fraction have been reported for an irradiated flame. Measurement of both of these parameters is important because the mechanisms of soot formation and oxidation depend exponentially on flame temperature [13, 14]. However, such measurements are also difficult because the introduction of high-flux, broadband radiation introduces challenges both to intrusive and to optical measurements. The use of a thermocouple is problematic because the thermocouple will be heated by irradiation to a temperature different from that of the surrounding gases. Strong broadband irradiation will also generate strong interferences to relevant optical methods [15]. However, this challenge has recently been overcome by Gu *et al* [16], who developed improved capability for the two-line atomic fluorescence (TLAF) method that had previously been developed only for non-irradiated flames [17]. Therefore, this new method was adopted in the present work to measure flame temperatures.

For the reasons outlined above, the first aim of the present paper is to quantify the influence on the soot volume fraction and temperature of a sooty flame of broadband irradiation at fluxes of relevance to solar towers using non-intrusive laser techniques LII and TLAF,

respectively. The second aim is to provide new insight into the mechanisms responsible for any influences thus identified.

2.   Methodology

2.1   High flux solar simulator

The solar simulator, illustrated in Figure 1, consists of a 6 kW Metal Halide Lamp close-coupled with an elliptical reflector and co-aligned with a conical secondary lamp concentrator to further concentrate the radiation. A tertiary concentrator is also employed to cause the concentrated radiation to double-pass through the focal area. Details of the optical design of the solar simulator, which was perfomred using an experimentally validated Monte-Carlo ray-tracing code, are reported elsewhere [18]. The study employs a metal halide lamp as the light source of the solar simulator, whose spectrum closely matches the solar spectrum [19]. The elliptical reflector is made of aluminum alloy 1050, with a physical vapor deposition coating comprising alumina and silica, similar to that used by Petrasch *et al.* [20]. The secondary concentrator is cone shaped with an inlet diameter of $D = 500$ mm, an outlet diameter of $d = 55$ mm and a length of $L = 1100$ mm. The tertiary concentrator is also conical with $D = 200$ mm, $d = 0$ and $L = 60$ mm. Both the secondary and tertiary concentrators were made of polished stainless steel with a reflectivity of 65% and are water cooled to less than 50 °C during operation, to minimize both the thermal impact of the facility on the flame and degradation of the reflecting surface.
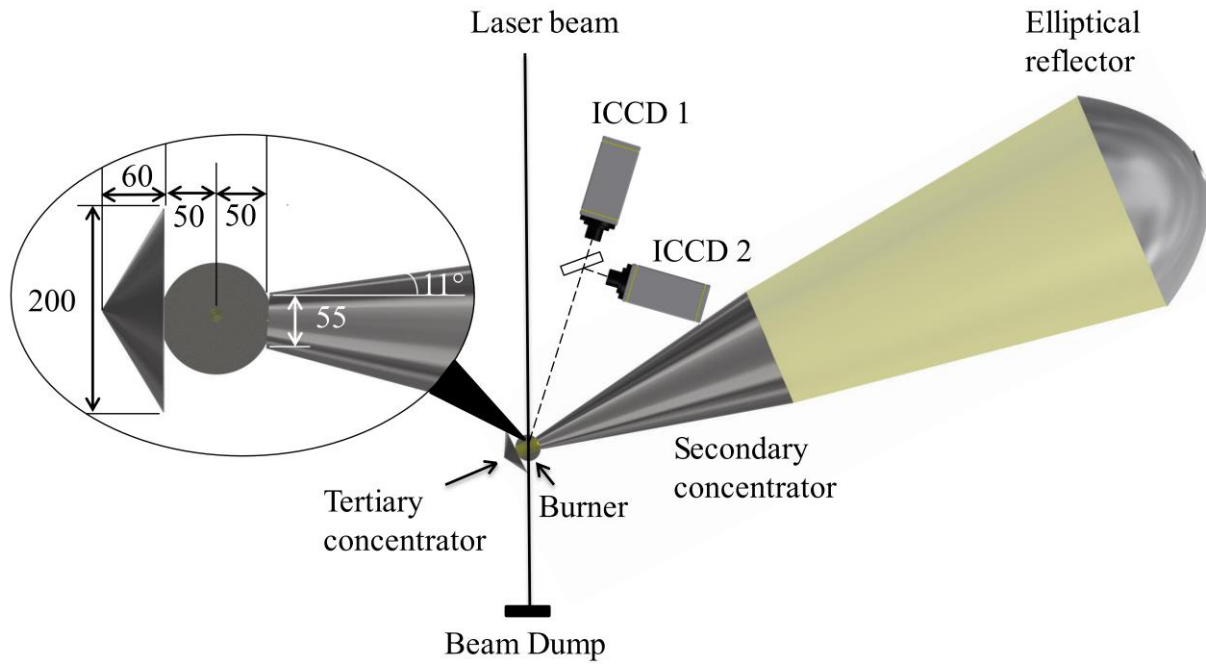
Figure 1. A plan view of the LII and TLAF arrangement in flame irradiated by broadband radiation from a the solar simulator. Dimensions are in mm.

The heat flux profile at the target area was determined with a validated Monte Carlo ray-tracing model. Firstly, the heat flux concentrated by the secondary cone was measured following the method reported previously [18, 20-23]. A Lambertian plane of 250 mm × 250 mm was placed 50 mm downbeam of the secondary lamp concentrator, which is also the focal plane of the elliptical reflector with 3 m focal length. Images of the Lambertian plane were acquired using a 1600×1200 pixels Mega-plus camera. The Lambertian target was then replaced with a water cooled circular foil transducer TG1000-1 (Vatell Corporation) to measure the temperature difference between the center and the circumference of the transducer, which is directly proportinal to heat flux. The image of the radiation reflected by the Lambertian target was converted to a heat flux based on the measurement with the transducer. The measured heat flux map 50 mm downbeam from the secondary concentrator was then used to validate a Monte-Carlo ray-tracing model. After this, an irradiance map 50 mm downbeam of the seconedary concentrator and 50 mm upbeam of the tertiary concentrator was simulated with the experimentally validated ray-tracing model [18]. This was necessary becayse the double path of radiation in the area between the secondary and tertiary concentrator prevents the application of any intrusive physical instrument.

Figure 2a presents the 64 mm long laminar sooty flame employed in the current study. Figure 2b

shows the irradiance map of the radiation applied to the flame, with the radiant flux peaking at 0.45 MW/m^2 and generating an average flux of 0.27 MW/m^2 in the flame area. Figure 2c presents the radial profiles of the heat flux at different heights above burners, HABs. It can be seen that the heat flux varies significantly in the axial direction, while that in the radial direction is quasi-uniform within the flame width (10 mm). The simulated heat flux for the case without the tertiary concentrator agree with the measured results to within 5% for the peak flux and to within 13% in half width.

(a) (b) (c)
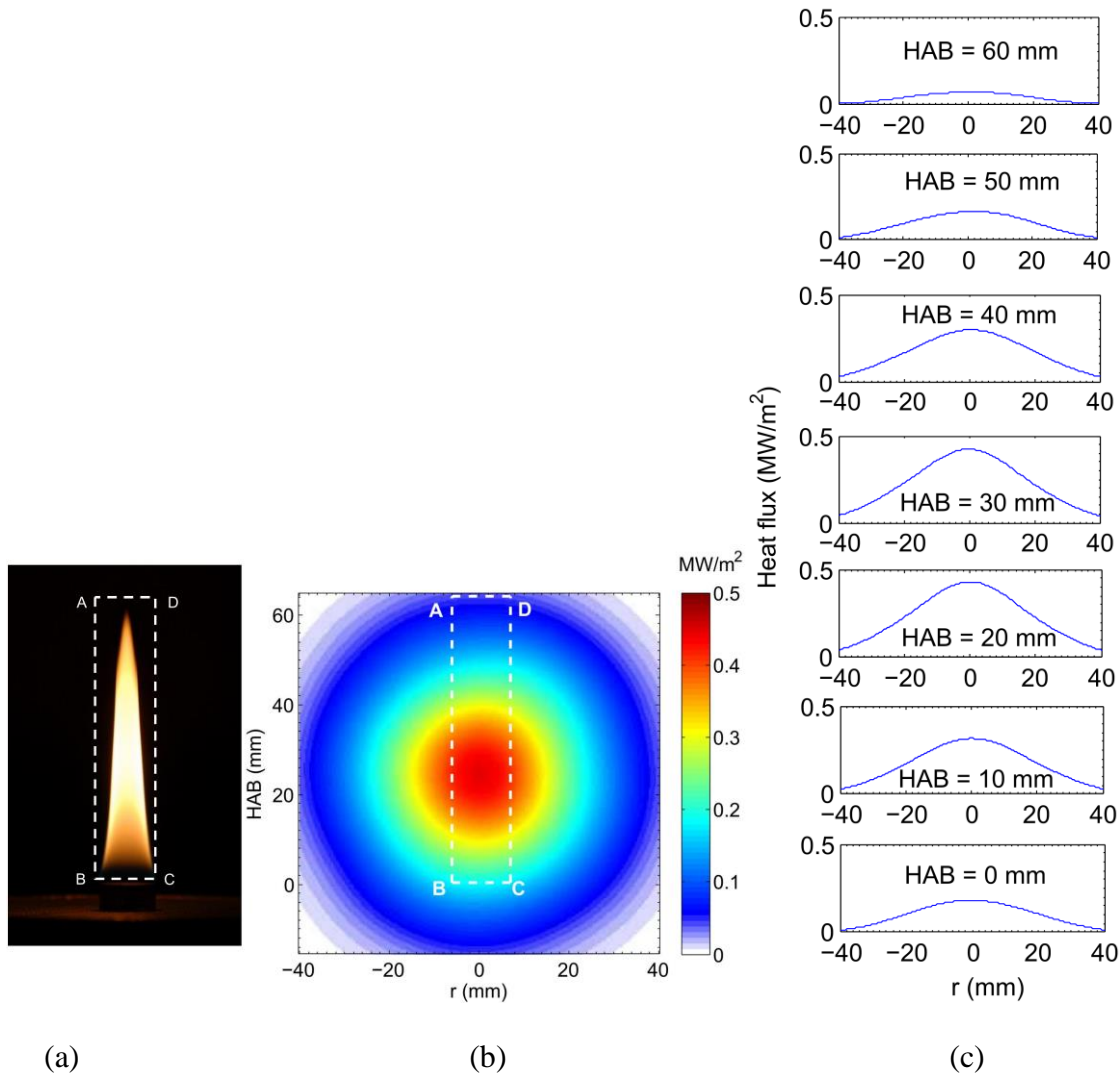
Figure 2. a) Image of the natural luminescence from the C$_2$H$_4$/air diffusion flame, termed a "Santoro flame" [24, 25], with the solar lamp off. b) The distribution of heat-flux at the focal plane of the solar simulator, without the flame present. The position of the flame is shown by square A-B-C-D in both a and b. c). the radial profiles of heat-flux at HAB = 0-60 mm.

2.2 Burner

A laminar non-premixed ethylene flame was employed firstly becaues its high soot loading results in a strong potential for absorption of CSR and, secondly, because this flame without irradiation has been widely investigated previously [26-28]. The burner consists of a central fuel pipe with ID 10.5 mm and OD 12.6 mm, surrounded by an annular co-flow cylinder with an inner diameter of ID 97.7 mm and OD 101.5 mm, both made of brass. The conditioning of the co-flow gas stream was achieved with the use of stainless steel mesh, steel honey comb and glass beads. A steel honey comb was also employed in the fuel jet to ensure uniform velocity distribution at the jet exit. Industrial grade ethylene (>99.5% C_2H_4) at a flowrate of 0.184 standard litres per minute (SLM) was used for the fuel, while the air flowrate was127.7 SLM.

2.3   Planar LII measurement

The experimental arrangement used for the present LII measurements follows that described previously [24]. A schematic diagram of the experimental layout is shown in Figure 1. An Nd:YAG laser operating at 1064 nm was used for the LII excitation. The laser beam was circularly polarised and formed into a sheet of ~0.3 mm thick that was aligned with the nozzle axis. The LII laser sheet was clipped with a rectangular aperture to 25 mm in height. The operating laser fluence was maintained at ~0.5 J/cm^2, which is within the plateau regime to avoid the dependence of the LII signals with the laser fluence variation [29, 30]. The LII signals were detected with an ICCD camera (ICCD 1) through a 410-nm optical filter (10-nm bandwidth) [24]. The gate width of the camera was set to 30 ns. The images from the cameras were spatially matched to pixel accuracy by taking an image of the target immediately after the LII measurement using long gate width. The LII signals were calibrated using laser extinction measurements following Qamar *et al.* [31]. A chopped, continuous-wave 1064-nm beam was used to avoid the influence of the extinction processes by polycyclic aromatic hydrocarbons (PAH) [32]. The soot extinction coefficient (K_e) was taken to be 4.03, computed with the formula obtained from Mie theory [33], using the complex refractive index *m=2.75-2.25i* [34].

The LII measurements of the Santoro flame were conducted with and without the irradiation from the solar simulator. Images of the flame with the lamp on but the laser off were

also taken to be used for the background correction. This was later substraced from the LII signal with the lamp on to correct for the interferences of scattering from soot. The 25 mm high laser beam was traversed axially, to allow imaging of the entire flame. The measurement of f_v is repeatable to within 5% as determined from 6 separate measurements. All images presented here have been corrected for background and detector attenuation. The images presented for this laminar flame were averaged from 200 frames to improve the SNR. Being a steady laminar flame, there is no loss of information resulting from this averaging [17].

2.4   TLAF measurement

The temperature was measured using two-line atomic fluorescence (TLAF) following Gu *et al.* [16]. Briefly, two Nd:YAG pumped dye lasers (Quantel, TDL 90) were employed in the present study to produce laser beams centred at 410.18 nm and 451.13 nm. The tracer species employed in the TLAF technique, atomic indium, is excited to the same upper state at 410.18 nm and 451.13 nm. The corresponding fluorescence signals were collected at 451.13 nm (Stokes signal) and at 410.18 nm (anti-Stokes signal) were collected using two intensified CCD cameras (ICCD 1 & ICCD 2 shown in Figure 1). Flame temperature was then derived from the collected LIF signals according to the Boltzmann's function after correcting the raw images for scatted interferences from the high flux radiation. This correction is the main feature that differentiates this measurement from our previous work reported elsewhere [35].

3.   Results

3.1.   Influence of CSR on the soot concentration and temperature within a flame

Figure 3 presents images of the spatial distribution of soot volume fraction (f_v) for the cases with and without the irradiation from the solar simulator. It can be seen that f_v is significantly higher in the flame with CSR, especially on the fuel rich side, although there is no detectable change to the length and width of the flame. The reason for the lack of perfect symmetry in the distribution of soot for the irradiated flame is that, in the plane where the laser beam intersects with the flame, the profile of simulated solar radiation is not symmetrical.
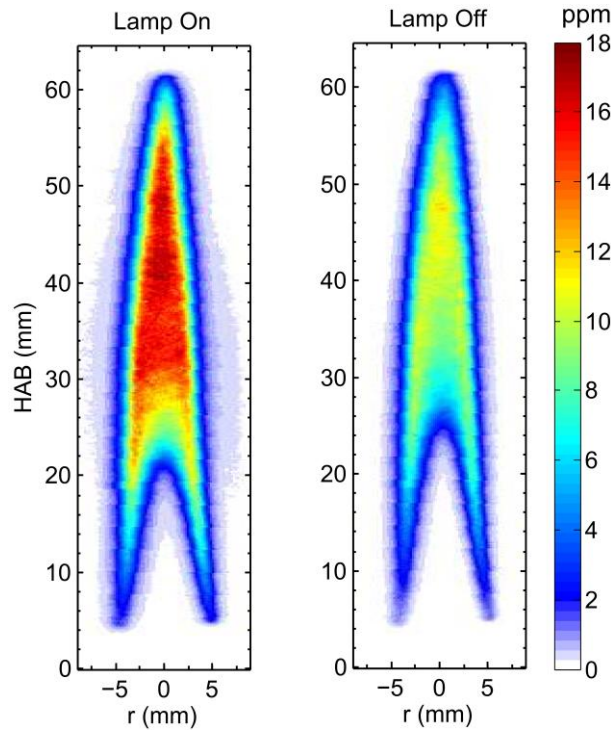
Figure 3. Measured soot volume fraction in a planar slice (0.3 mm thick) through the axis of the flame with simulated solar radiation on (left) and off (right).

Figure 4a presents the axial profiles of f_v and temperature as a function of the normalized HAB, i.e. HAB/L_f, where L_f is the flame length. It can be seen that, f_v is increased by a factor of ~ 1.8 by CSR for HAB/L_f > 0.16, and peaks slightly upstream at HAB/L_f =0.7. Also presented is the data of Konsur *et al.* [36], who measured the influence of preheating a fuel jet by up to 160 °C, but without any irradiation. Some important trends can be deduced, despite some differences between the conditions employed in the two experiments. In particular their burner had an internal diameter of 1.6 mm, no co-flow, and used a fuel mixture of 50% (volume) C_2H_2–50% N_2 [36]. However, while the results reported by Konsur *et al.* [36] show that the f_v can be increased by fuel preheating, the influence is only observed in the upstream region of the flame and does not increase the peak value of f_v. Their increase is explained by the preheating of the fuel promoting pyrolysis rates which generates more soot in this region [36]. In contrast, the extent of preheating of the fuel in the current study is negligible for HAB/L_f < 0.19. In addition, while the fuel preheating translates the position of soot formation upstream, it does not increase the magnitude of the peak f_v. Furthermore, the TLAF measurement shows that the addition of CSR causes the centre line flame temperature to

increase by 50-100 K at HAB/L_f =0.35-0.6. These comparisons are sufficient to show that the irradiation with solar flux has a more profound influence on f_v than does the preheating of the fuel over the temperature range investigated previously.

Figure 4b presents the spatial gradients of soot. Because this is a temporally stable flame, the spatial gradient of soot can be used to quantify the formation rate (d_{fv}/d_{HAB} >0) and consumption rate (d_{fv}/d_{HAB} <0) of soot. The inception point is defined as the location where d_{fv}^2/d_{HAB} is the highest. By this definition, the inception of soot is found to be translated upstream by CSR by 7% of the flame length. Comparing the soot formation rate, i.e. the positive values of the spatial gradient with and without CSR, it was found that the rate of soot formation is higher for the case with CSR, by a spatial average percentage of 36%. Furthermore, in the downstream locations (HAB/L_f > 0.7), the soot consumption rate is also higher for the case with CSR than that without, by a spatial averaged value of 34%. Noteworthy is that the measurement of f_v is repeatable to within 5% as determined from 6 separate measurements.


(a)   (b)
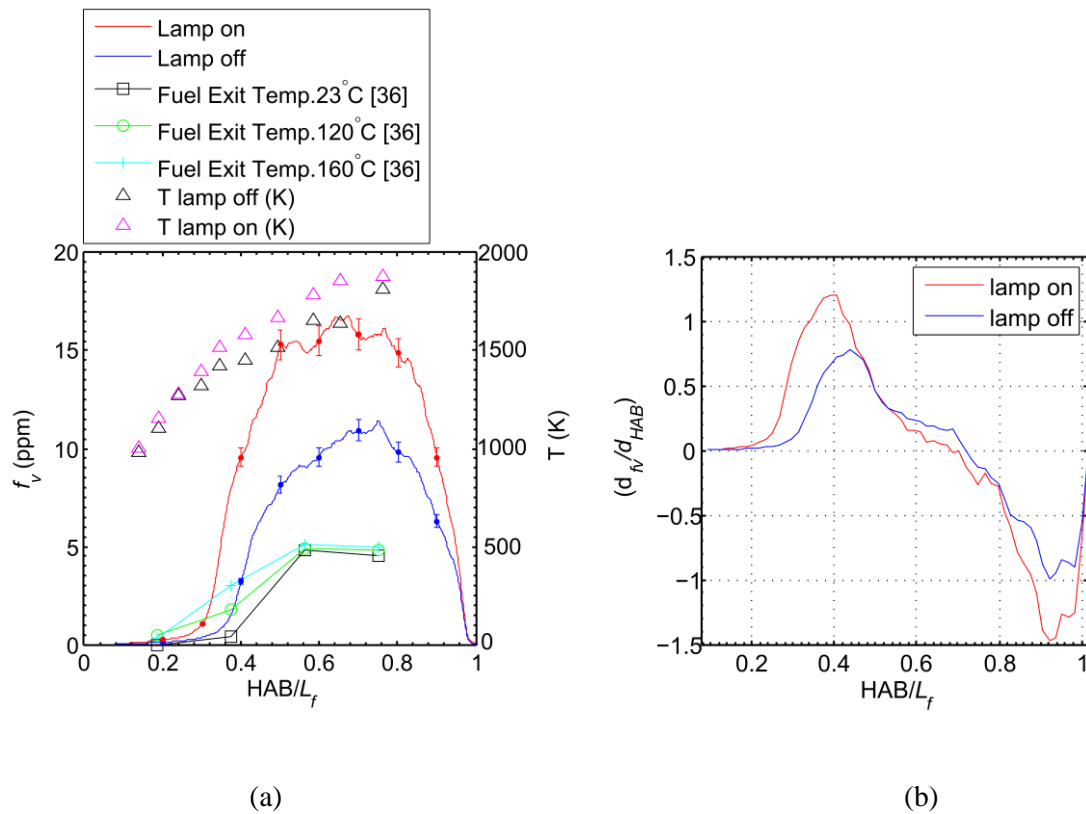
Figure 4. a). Profiles of f_v and T along the axis of the flame, i.e. at r =0, for the current measurements and those of preheating a fuel mixture of C_2H_2/N_2 (50%/50%) reported by Konsur *et*

al. [36]; and b) the spatial gradient of f_v along the centre line from the base to the tip of the flame.

Figure 5 presents the radially integrated f_v as a function of HAB, i.e.

$$f_{v\_int} = \int_0^{2\pi} d_\theta \int_0^R f_v \cdot r \cdot d_r \text{ (ppm·m}^2\text{)}, \qquad (1)$$

It can be seen that the total soot volume for the case with the irradiation (the area under the red curve) is 55% greater than that without (the area under the blue curve). The lack of perfect convergence of the two curves at the flame tip is attributed to the relatively high noise at this point, which is more significant for the integral than for the single point measurements reported in Figure 4, where the convergence is better.
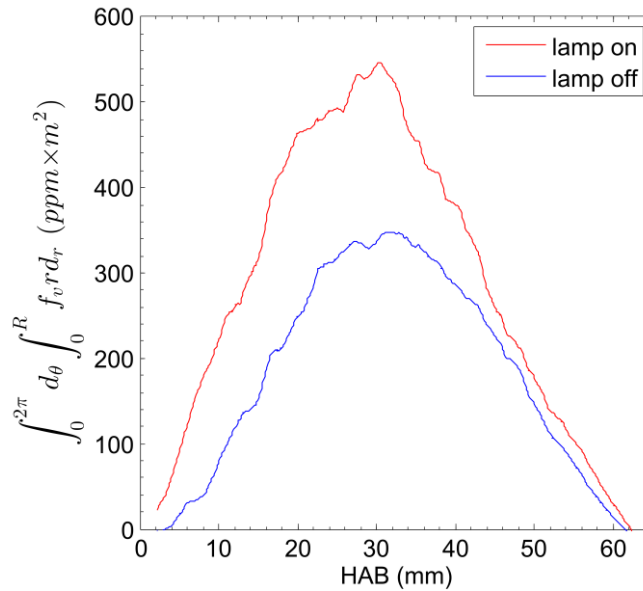
Figure 5. Radially integrated f_v through the cross section of the flame at each HAB (Eqn 1), as a function of HAB.

Figure 6 presents the radial profiles of f_v and T [16] at different flame heights, from HAB=12 mm to 49 mm. It can be seen that f_v is increased with the addition of CSR by 40% - 50 % at downstream locations HAB > 26 mm. The spatially averaged flame temperature along the radial direction was also increased for the case with CSR by a fraction of about 8% for 26 mm < HAB < 49 mm. That the increase of temperature is lower than that of f_v is consistent with the non-linear relationship between temperature and f_v. That is, reaction rates have an exponential dependence of temperature, while soot evolution depends also on residence time.
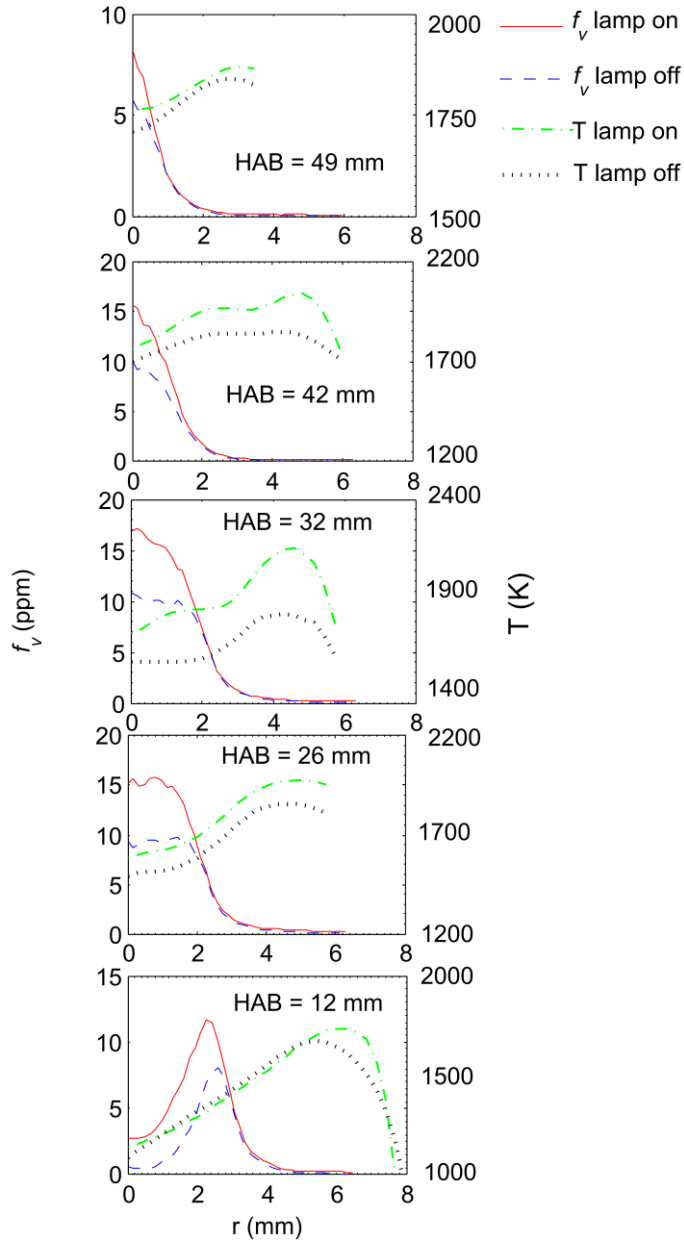
**Figure 6.** Radial distributions of f_v and T at HAB=12, 26, 32, 42 and 49 mm.

Figure 7 presents the radial distribution of the mole fraction of benzene (A_1), pyrene (A_4) and C_2H_2 calculated by Liu *et al.* [28] using the DLR mechanism. It can be seen that C_2H_2 and A_1 are found mostly at the upstream locations, HAB < 30 mm, while A_4 is found at all HABs studied (12mm $\leq$ HAB $\leq$ 49mm) and peaks at around HAB = 32 mm [28]. All of these species can potentially contribute to the absorption of CSR because benzene, small aromatic hydrocarbons and PAH are UV absorbers and IR emitters [37, 38]. This absorption is therefore deduced to be the most plausible explanation for the upstream translation of the point of soot inception.

71
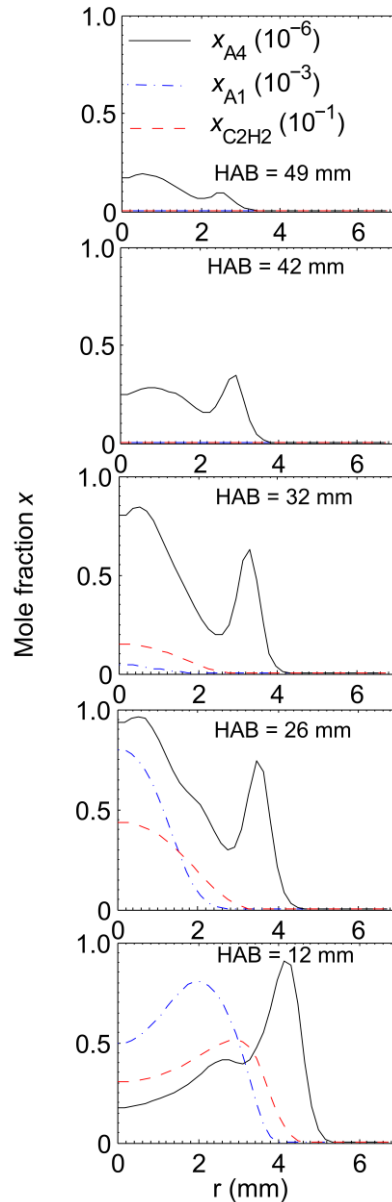
Figure 7. Radial distribution of the mole fraction of benzene (A_1), pyrene (A_4) and C_2H_2 at HAB = 12, 26, 32, 42, 49 mm, calculated using the DLR mechanism by Liu *et al.* [28]. Note the difference in range of each species shown in the key.

Figure 8 presents the radial gradient of f_v, df_v/dr, which was calculated from the fuel rich side to the fuel lean side. As for the discussion related to Figure 4b, the spatial gradient of soot is used to quantify the formation rate ($df_v/dr > 0$) and consumption rate ($df_v/dr < 0$) of soot in the radial direction. It can be seen that the formation rate of soot in the radial direction is increased by the introduction of CSR by 82% (HAB = 10 mm), 63% (HAB = 20 mm) and 32% (HAB = 30 mm). The consumption rate of soot in the radial direction is also increased by the external radiation by an

average of 54%, with the increase being 86%, 63%, 20%, 41% and 61 % for HAB = 10, 20, 30, 40, 50 mm, respectively. In addition, the CSR translates soot consumption towards the flame axis beyond HAB = 20 mm. That is, the irradiation translates the soot consumption/formation zone closer to the fuel rich side, which implies a greater potential to consume soot.
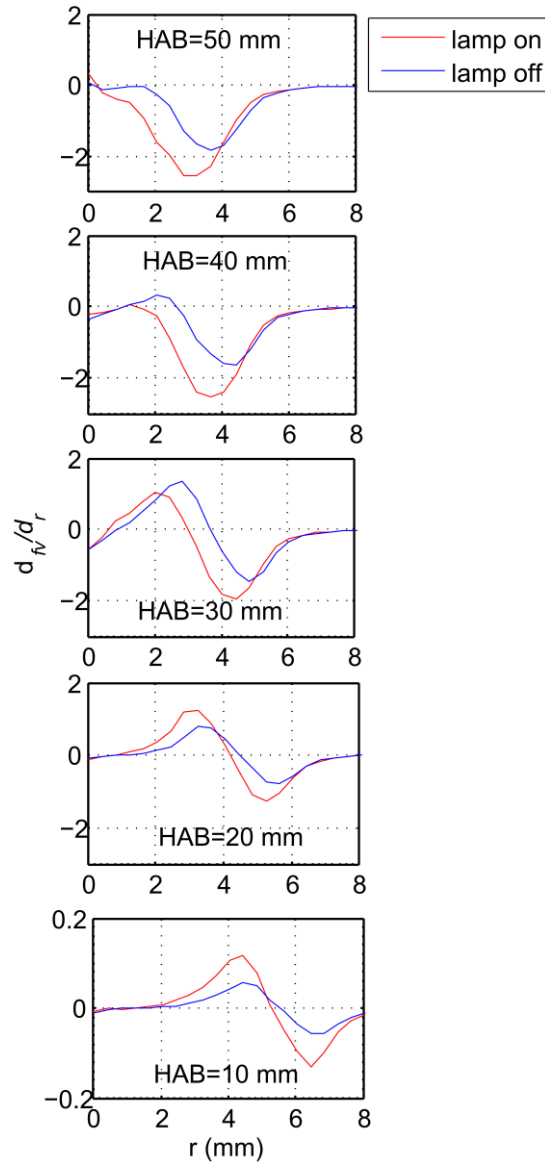
Figure 8. Spatial gradients of f_v as a function of radius.

The fraction of solar radiant energy absorbed by the flame was estimated with the extinction measurement performed by Migliorini *et al.* [39]. These measurements were performed with broadband radiation of 450-1100 nm generated with a tungsten strip lamp through a laminar non-premixed ethylene flame with a fuel flow rate of 0.194 SLM and a jet ID = 10.8 mm [39]. This flame condition is very close to that of the current work (fuel flow rate of 0.184 SLM and fuel jet

ID = 10.5 mm). Their results show that the line-of-sight absorption through the flame at $HAB/L_f =$ 0.14, 0.59, 0.70, and 0.77 is 0.029, 0.124, 0.073, 0.053 respectively. These measurements were used to estimate the flame absorption as a function of normalised flame length. This estimation requires converting their measured value of line-of-sight absorption through the axis [39] to a line-of-sight absorption throughout the entire flame cross section (α_A), details of which are provided in the Appendice 1.

The values of α_A as derived from the measurement of Migliorini *et al.* [39] are shown at 4 HABs in Figure 8 (black circles). The continuous function of α_A was estimated from the averaged values of measured f_v at each HAB, assuming that soot controls the absorption of broadband radiation, as follows

$$\alpha_A = C_1 \frac{\int_{-R}^{R} f_v d_r}{2R} , \qquad (3)$$

where R is the flame edge in the radial direction. C_1 is a coefficient that represents the line of sight absorption rate, which depends only on soot volume fraction. This was determined empirically from Eqn 3 to be C_1 = 0.00725/ppm, which yields the lowest deviation (σ) between the measured and the calculated α_A, with σ = 2.3%, where σ is defined as the standard deviation of the difference between the calculated and measured α_A. The assumption that soot dominates the absorption of broadband radiation was validated by an independent calculation of soot absorption, which shows that these two values agree with each other to within 3% (Appendix 2).

Also shown in Figure 8 is the calculated radially integrated incident radiant flux in the flame region as is expressed in Eqn 4,

$$I_{int} = \int_{-R}^{R} I d_r, \qquad (4)$$

where I is the incident radiant flux (kW/m^2) applied to the flame as is shown in Figure 2b.

The products of the incident lamp radiation and the absorption rate were then used to calculate the absorbed lamp radiation (blue lines in Figure 9). Hence the integral of this relationship corresponds to the external radiant energy that is absorbed by the flame, which is 12 W for this case. This corresponds to 6.9% of the energy of the total power of the flame, 174.8 W, based on the lower heating value (LHV) of the fuel. The flame absorption can, in turn, be used to

estimate the total temperature rise of the flame.
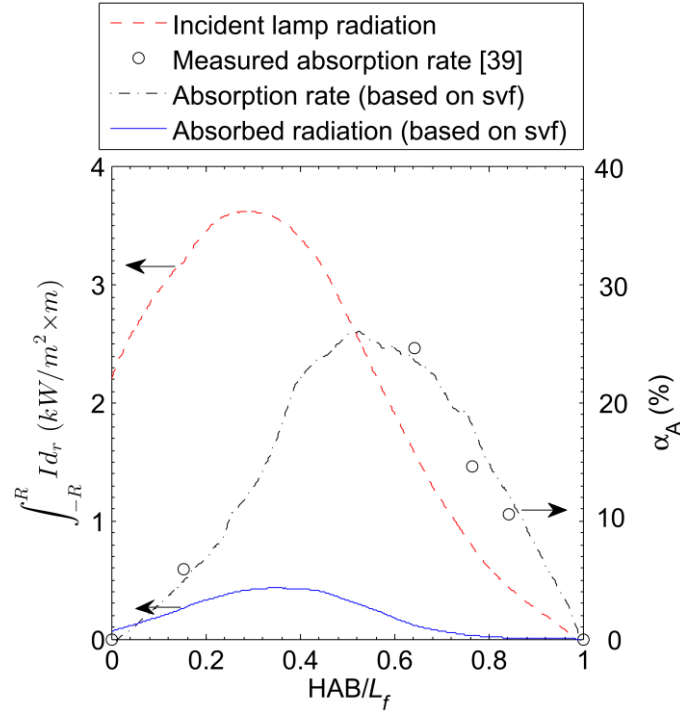
Figure 9. Calculated axial variation of absorbed radiation by the flame region (red curve); together with the measured values of absorption through the cross section of each HAB (black symbols), derived from the previous measurements of line of sight absorption [39]; estimated absorption rate based on the radially-averaged f_v at each HAB (black curve); together with the calculated lamp radiation that is absorbed by the flame (blue curve), i.e., the product of the irradiation and absorption.

3.2. Calculation of the global temperature increase of the flame

The change of global temperature within the flame can be estimated using an energy conservation equation, as is shown in Equation 2:

$$\sum h_{i,T_2} - \sum h_{i,T_1} = E_{CSR} - E_{\Delta\ radiant\ loss} \qquad , \qquad (3)$$

Here T_1 is the spatial averaged flame temperature without CSR, which was calculated following Liu *et al.* [28], T_2 is the spatial averaged flame temperature with CSR, which is to be calculated; E_{CSR} is the CSR that is absorbed by the flame, which is estimated to be 12 W based on Figure 9; $h_{i,T}$ is the enthalpy of species i in the flame at temperature T for reference state of 298.15 K, as is defined below:

$$h_{i,T} = \int_{298.15}^{T} c_{p,i,T} d_T \ , \qquad (4)$$

$c_{p,i,T}$ is the heat capacity of species i at temperature T [40]; the species assessed include CO_2, CO, C_2H_4, CH_4, C_2H_2, soot, H_2O, O_2 and N_2, the flow rate of these species was determined by their spatial averaged concentration within the flame, which was calculated following Liu *et al.* [28]; $E_{\Delta\,radiant\,loss}$ is the increased radiant loss due to the increased soot volume, as was determined from Figure 5.

$$E_{\Delta\,radiant\,loss}=\varepsilon\sigma AT^4 \,, \qquad (5)$$

where ε is taken to be 1 for soot; A is the surface area of soot, which is determined by the increased soot volume and an assumed soot particle diameter of 30 nm.

With the method described above, the estimated temperature difference $\Delta T_{esti.}$ of the flame with and without CSR is around 107 K. Comparing $\Delta T_{esti.}$ with the measured value ΔT_{TLAF} averaged from 5 radial profiles shown in Figure 6, it can be seen that the calculation is consistent with the measurement within about 10% (i.e. 10 K). This demonstrates that the measured increase in temperature can be explained by the energy absorbed by soot and other species in the flame, which transfer the heat to the flame gases, increasing the global enthalpy and temperature of the flame.

4. Discussion

The upstream translation of soot inception can be attributed primarily to the absorption of CSR by soot precursors such as C_2H_2, which absorb infrared radiation [41], together with benzene, small aromatic hydrocarbons and PAH, which are UV absorbers [37, 38]. The absorption spectra of poly-condensed aromatic functionalities shift toward the visible as the number of aromatic rings increases, because the energy gap between the $\pi— \pi^*$ bands decreases with an increase in the coordination length of the n bonds [42]. Any absorption that promotes fuel decomposition or the formation of small aromatics is important in accelerating the soot formation because this is a rate-limiting step, even though it constitutes only a small part in the overall soot formation process [43-45]. Strong evidence that this mechanism is significant in the present process can be found in the upstream translation in the point of inception by approximately 7% of the flame length (Figure 4b).

To identify the major mechanism responsible for the increase in flame temperature under CSR, the absorption of radiation by several key species has been estimated and compared. The molecular absorption was estimated by multiplying the spectral line intensity ($S_{\eta\eta\prime}$) reported in the HITRAN database [46] with molecular number density (*N*) derived from the work of Liu *et al.* [28], the optical path length ($\int_{-R}^{R} dx$) of the current study and the bandwidth of absorption ($\int_{\lambda_1}^{\lambda_2} d\lambda$). This yields the fraction of the energy within the solar spectrum that is absorbed along an optical distance with a molecular number density of *N*. The details of this estimation are reported in Appendix 2, Section 2.1. The absorption of soot was estimated based on the beam attenuation theory, where the ratio of the attenuated beam to the incident beam intensity (I/I_0) can be calculated based on the soot volume fraction, optical path and wavelength of radiation using Bouguer's law [47, 48]. Details of this estimation are reported in Appendix 2, Section 2.2.

These estimations show that the absorption of gas phase species such as O_2, CO_2 and C_2H_4 has a negligible contribution to the total CSR absorbed by the flame for the current case, because there is hardly any overlap between the absorption bands of these molecules and the lamp spectrum. The absorption by several key gas phase species including H_2O, C_2H_2, A_1 and A_4 is plotted in Figure 10, together with the absorption by soot and that by the whole flame, based on previous measurements (Figure 9). It can be seen that the estimated soot absorption matches to the overall absorption by the flame to within 3%, making this the dominant factor driving the increase of flame temperature. The molecular absorption by H_2O is one order of magnitude lower than soot absorption, but may be significant under some conditions. The contribution to temperature rise by other gas phase species is negligible, with C_2H_2 being two orders of magnitude lower than soot absorption, while that of A_1 and A_4 is about 4 orders of magnitude lower than soot absorption. It is worth noting that the molecular absorption was estimated based on the absorption spectra of gases at atmospheric temperature, while actual gases will be at flame temperature. The exact level of uncertainty associated with this approximation is unknown, but is expected to be good enough to support the conclusion.
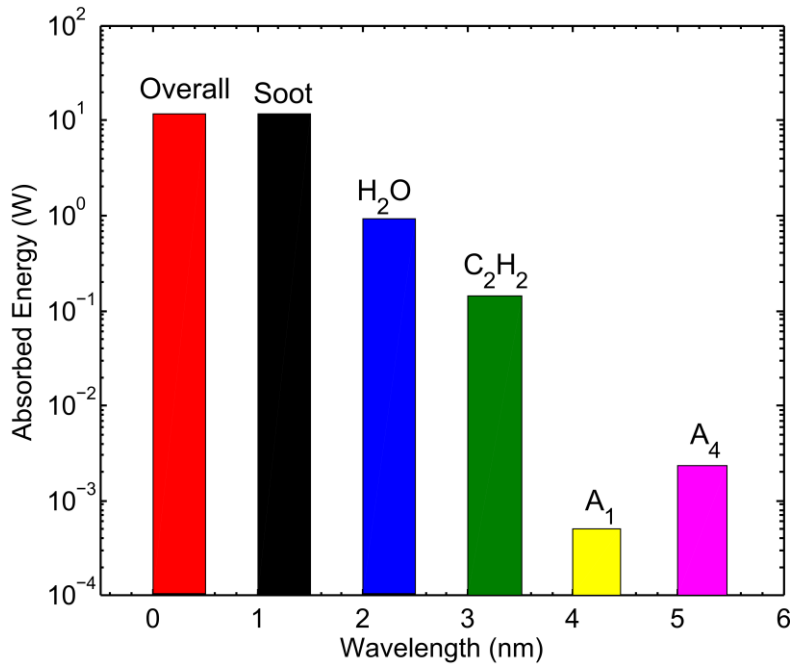
Figure 10. Calculated absorption by key species in the flame and that by the whole flame. Refer to Appendix 2 for details.

The measured increase in soot volume fraction from the introduction of CSR is deduced to be caused by two factors: 1) the increased temperature on the fuel-rich side of the reaction zone, which in turn is driven mostly by the absorption of radiation by soot; 2) the augmented soot inception due to the absorption of radiation by soot precursors. The large increase in f_v by irradiation with CSR (Figures 3 and 4) also provides direct experimental evidence that this process is strongly coupled. That is, an increase in f_v caused by the absorbed irradiation will further enhance absorption of CSR thus leads to a further increase in f_v.

The increased rate of soot consumption at the edge of the flame (Figure 7) can be explained by the increased diffusion rate of oxygen to the soot oxidation zone due to the increased temperature, thus generating more OH. Puri *et al.* [49] demonstrated that OH is the dominant oxidizer of soot, with O_2 concentration remain very small in the regions of active soot oxidation. Based on Puri *et al.*'s measurement, Lautenberger *et al.* [50] concluded that the paucity of oxygen suggests that soot oxidation in non-premixed flames is controlled by the diffusion of oxygen into the soot oxidation zone at temperatures high enough for the oxygen to react with H to form OH radicals. As the diffusion rate of oxygen molecule increases with temperature, it is widely adopted that OH concentration in the soot oxidation zone also increases with temperature [51, 52].

5.   Conclusions

The influence of simulated concentrated solar radiation on the Santoro flame was found to be significant. Specifically, the irradiation of this flame by CSR at an average flux of 0.27 MW/m^2 causes:

1. f_v to increase by up to 50% at HAB > 30 mm, while the integrated soot volume in the flame is increased by 55%.

2.   the point of soot inception to be translated upstream by 7% of the flame length.

3.   no change to either the visible length or width of the flame, nor to the measured position of the outer envelope of soot.

4.   the consumption rate of soot in the axial direction to increase by 34% at the downstream locations (HAB/L_f > 0.7). The consumption rate of soot in the radial direction was also found to be higher for the case with the simulated CSR, by an average value of 54%.

5.   the spatially-averaged flame temperature in the radial direction to increase by about 8% at 26 mm< HAB < 49 mm.

The explanations of the increase of soot volume fraction, soot consumption rate and T are as follows:

1.   The upstream translation of the point of soot inception is attributed to the absorption of CSR by soot precursors.

2.   The increase in temperature is deduced to result primarily from absorption of CSR by soot. The contribution of molecular absorption is at most second order, with that of H_2O being one order of magnitude lower and that of all other species being at least two orders of magnitude lower than soot absorption.

3.   The increase in soot volume fraction from the CSR is deduced to be caused by two factors: 1) the increased temperature on the fuel-rich side of the reaction zone, promoting soot formation; 2) the upstream translation of soot inception due to the absorption of radiation by soot precursors.

4.   The increased rate of soot consumption is attributed to the increased flame temperature.

79

Acknowledgements:

Reference:

1.   G. Ordorica-Garcia; A. V. Delgado; A. F. Garcia, Energy Procedia 4 (0) (2011) 809-816
2.   G. Nathan; D. L. Battye; P. J. Ashman, Applied Energy 113 (2014) 1235-1243
3.   Y. Ying; E. J. Hu, Applied Thermal Engineering 19 (11) (1999) 1173-1180
4.   Marwan Mokhtara; Muhammad Tauha Alia; Rajab Khalilpourb; Ali Abbasb; Nilay Shahc; Ahmed Al Hajajc; Peter Armstronga; Matteo Chiesaa; S. Sgouridisa, Applied Energy 92 (2012) 668-676
5.   C. P. Garcia P, Soler R, Gagnepain B, Ferriere A, Flamant G. , Journal of Solar Energy Engineering;   130 (14502) (2008) 1-3
6.   F. A. Grange B, Bellard D, Vrinat M, Couturier R, Fan Y. , Journal of Solar Energy Engineering 133: (31004) (2011) 1-11
7.   SOLGATE, in: Solar hybrid gas turbine electric power system; European Commision: 2005.
8.   C. R. Gou C, Hong H. , Energy 32 (2007) 1707–1714.
9.   M. S. Mehos; K. M. Anselmo; J. B. Moreno; C. E. Andraka; K. S. Rawlinson; J. Corey Combustion system for hybrid solar fossil fuel receiver. 2004.
10.   G. J. Nathan; B. B. Dally; P. J. Ashman; A. Steinfeld A hybrid receiver combustor. Provisional Patent Application No. 2012/901258. Adelaide Research and Innovation Pty. Ltd. 2012.
11.   H. E. Nathan GJ, Dally BB, Alwahabi ZT, Battye DL, Ashman PJ, et al. A boiler system receiving multiple energy sources. [Priority Date: 19.10.09]. 2009.
12.   P. R. Medwell; G. J. Nathan; Q. N. Chan; Z. T. Alwahabi; B. B. Dally, Combustion and Flame 158 (9) (2011) 1814-1821
13.   K. Leung; R. Lindstedt; W. Jones, Combustion and flame 87 (3) (1991) 289-305
14.   J. H. Kent; D. R. Honnery, Combustion and Flame 79 (3–4) (1990) 287-298.
15.   G. J. Nathan; P. A. M. Kalt; Z. T. Alwahabi; B. B. Dally; P. R. Medwell; Q. N. Chan, Progress in Energy and Combustion Science 38 (1) (2012) 41-61
16.   D. Gu; Z. Sun; G. J. Nathan; X. Dong; Z. Alwahabi; B. B. Dally, in: *The 10th Asia-Pacific Conference on Combustion*, Beijing, China, 2015.
17.   Q. N. Chan; P. R. Medwell; Z. T. Alwahabi; B. B. Dally; G. J. Nathan, Applied Physics B 104 (1) (2011) 189-198
18.   X. Dong; G. J. Nathan; Z. W. Sun; D. H. Gu; P. J. Ashman, Solar Energy 122 (2015) 293-306
19.   X. Dong; Z. W. Sun; G. J. Nathan; P. J. Ashman; D. H. Gu, Solar Energy 115 (2015) 613-620
20.   J. Petrasch; P. Coray; A. Meier; M. Brack; P. Häberling; D. Wuillemin; A. Steinfeld, Journal of Solar Energy Engineering 129 (4) (2007) 405-411
21.   K. R. Krueger. Design and Characterization of a Concentrating Solar Simulator. UNIVERSITY OF MINNESOTA, 2012.
22.   Concentrating Solar Power Technology Principles, developments and applications, Woodhead Publishing Limited, 2012, p.^pp.
23.   R. A. Craig. Investigating the use of Concentrated Solar Energy to Thermally Decompose Limestone. The University of Adelaide, Adelaide, 2010.
24.   Q. N. Chan; P. R. Medwell; P. A. Kalt; Z. T. Alwahabi; B. B. Dally; G. J. Nathan, Proceedings of the Combustion Institute 33 (1) (2011) 791-798
25.   A. Gomez; M. Littman; I. Glassman, Combustion and Flame 70 (2) (1987) 225-241
26.   I. M. Kennedy; C. Yam; D. C. Rapp; R. J. Santoro, Combustion and Flame 107 (4) (1996) 368-382
27.   C. McEnally; A. Schaffer; M. Long; L. Pfefferle; M. Smooke; M. Colket; R. Hall in: *Computational and experimental study of soot formation in a coflow, laminar ethylene diffusion flame*, Symposium (International) on Combustion, 1998; Elsevier: 1998; pp 1497-1505.
28.   F. Liu; S. B. Dworkin; M. J. Thomson; G. J. Smallwood, Combustion Science and Technology 184 (7-8) (2012) 966-979
29.   C. Schulz; B. F. Kock; M. Hofmann; H. Michelsen; S. Will; B. Bougie; R. Suntz; G. Smallwood, Applied Physics B 83 (3) (2006) 333-354
30.   N. Qamar; Z. Alwahabi; Q. Chan; G. Nathan; D. Roekaerts; K. King, Combustion and Flame 156 (7) (2009) 1339-1347

31.   N. Qamar; G. Nathan; Z. Alwahabi; K. King, Proceedings of the Combustion Institute 30 (1) (2005) 1493-1500

32.   J. Zerbs; K. Geigle; O. Lammel; J. Hader; R. Stirn; R. Hadef; W. Meier, Applied Physics B 96 (4) (2009) 683-694

33.   W. H. Dalzell; A. F. Sarofim, Journal of Heat Transfer 91 (1) (1968) 100-104

34.   H. Chang; T. Charalampopoulos, Proc. R. Soc. London,Ser. A 430 (1990) 577–591

35.   D. Gu; Z. Sun; G. J. Nathan; P. R. Medwell; Z. T. Alwahabi; B. B. Dally, Combustion and Flame In Press)

36.   B. Konsur; C. M. Megaridis; D. W. Griffin, Combustion and flame 116 (3) (1999) 334-347

37.   W. W. Duley; D. A. Williams, The Astrophysical Journal Letters 737 (2) (2011) L44

38.   G. Malloci; C. Joblin; G. Mulas, Chemical Physics 332 (2) (2007) 353-359

39.   F. Migliorini; K. A. Thomson; G. J. Smallwood, Applied Physics B 104 (2) (2011) 273-283

40.   S. R. Turns, An introduction to combustion, McGraw-Hill Higher Education, 2000, p.^pp. 622-643.

41.   L. S. Rothman; I. E. Gordon; A. Barbe; D. C. Benner; P. F. Bernath; M. Birk; V. Boudon; L. R. Brown; A. Campargue; J. P. Champion; K. Chance; L. H. Coudert; V. Dana; V. M. Devi; S. Fally; J. M. Flaud; R. R. Gamache; A. Goldman; D. Jacquemart; I. Kleiner; N. Lacome; W. J. Lafferty; J. Y. Mandin; S. T. Massie; S. N. Mikhailenko; C. E. Miller; N. Moazzen-Ahmadi; O. V. Naumenko; A. V. Nikitin; J. Orphal; V. I. Perevalov; A. Perrin; A. Predoi-Cross; C. P. Rinsland; M. Rotger; M. Šimečková; M. A. H. Smith; K. Sung; S. A. Tashkun; J. Tennyson; R. A. Toth; A. C. Vandaele; J. Vander Auwera, Journal of Quantitative Spectroscopy and Radiative Transfer 110 (9–10) (2009) 533-572

42.   P. Minutolo; G. Gambi; A. D'Alessio; S. Carlucci, Atmospheric Environment 33 (17) (1999) 2725-2732

43.   I. Glassman in: *Soot formation in combustion processes*, Symposium (international) on combustion, 1989; Elsevier: 1989; pp 295-311.

44.   C. S. McEnally; L. D. Pfefferle; B. Atakan; K. Kohse-Höinghaus, Progress in Energy and Combustion Science 32 (3) (2006) 247-294

45.   C. S. McEnally; D. M. Ciuparu; L. D. Pfefferle, Combustion and flame 134 (4) (2003) 339-353

46.   L. S. Rothman; C. Rinsland; A. Goldman; S. Massie; D. Edwards; J. Flaud; A. Perrin; C. Camy-Peyret; V. Dana; J.-Y. Mandin, Journal of Quantitative Spectroscopy and Radiative Transfer 60 (5) (1998) 665-710

47.   A. D'alessio; A. Di Lorenzo; A. Sarofim; F. Beretta; S. Masi; C. Venitozzi in: *Soot formation in methane-oxygen flames*, Symposium (International) on Combustion, 1975; Elsevier: 1975; pp 1427-1438.

48.   R. J. Santoro; C. R. Shaddix, Applied combustion diagnostics   (2002) 252-286

49.   R. Puri; R. J. Santoro; K. C. Smyth, Combustion and Flame 97 (2) (1994) 125-144

50.   C. W. Lautenberger; J. L. de Ris; N. A. Dembsey; J. R. Barnett; H. R. Baum, Fire Safety Journal 40 (2) (2005) 141-176

51.   A. D'Anna; J. H. Kent; R. J. Santoro, Combustion Science and Technology 179 (1-2) (2007) 355-369

52.   A. Jocher; H. Pitsch; T. Gomez; G. Legros, Proceedings of the Combustion Institute 35 (1) (2015) 889-895

Appendix 1

The correlation between the absorption of radiation through a flame along a line (BA) and that throughout a circular cross section (area BDAEB) was derived by integrating the absorption throughout the circular area.
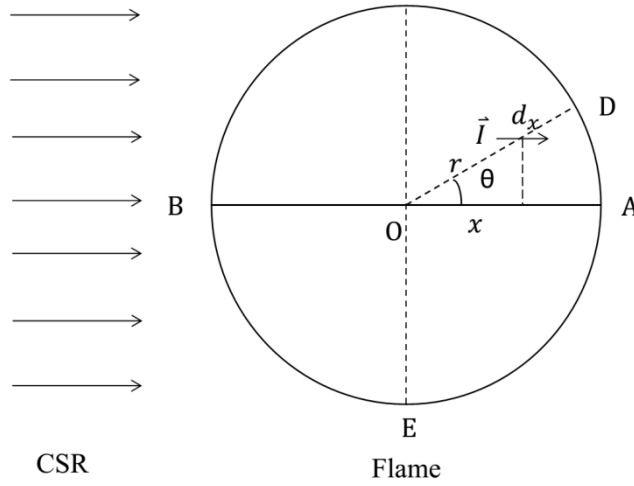

Figure A1. Diagrammatic sketch of the light absorption through a cross section of the flame at a given HAB.

Assuming the absorption α is a function of radial distance r:

$$\alpha = f(r)$$

Assuming light $\vec{I}$ comes from the x direction, then the absorption by the elements on line OD can be expressed as follows:

$$\alpha_{OD} = \int_0^{R \cdot \cos(\theta)} \alpha \, d_x = \int_0^{R \cdot \cos(\theta)} f(r) d_x$$

For the semicircle AEBA, the absorption by elements within this area is:

$$\alpha_{semi-area} = \int_{-\pi/2}^{\pi/2} d_\theta \int_0^{R \cdot \cos(\theta)} f(r) d_x$$

$$\alpha_{area} = 2 \cdot \alpha_{semi-area}$$

For centre line BA, the absorption is:

$$\alpha_{BA} = 2 \cdot \alpha_{OA} = 2 \cdot \int_0^R f(r) d_x$$

Case 1: Assuming the absorption throughout the area is constant, i.e. $\alpha = C$

$$\alpha_{semi-area} = \int_{-\pi/2}^{\pi/2} d\theta \int_{0}^{R\cdot\cos(\theta)} C d_x = \int_{-\pi/2}^{\pi/2} R \cdot C \cdot \cos(\theta) d_\theta = 2CR$$

$$\alpha_{area} = 2 \cdot \alpha_{semi-area} = 4CR$$

$$\alpha_{BA} = 2 \cdot \alpha_{OA} = 2 \cdot \int_{0}^{R} C d_x = 2CR$$

$$\frac{\alpha_{area}}{\alpha_{BA}} = 2$$

Case 2: Assuming the absorption is linear with the radial distance r, i.e. $\alpha = C - k_0 r$

$\alpha_{semi-area}$

$$= \int_{-\pi/2}^{\pi/2} d\theta \int_{0}^{R\cdot\cos(\theta)} (C - k_0 r) d_x = \int_{-\pi/2}^{\pi/2} d\theta \int_{0}^{R\cdot\cos(\theta)} (C - k_0 \frac{x}{\cos(\theta)}) d_x$$

$$= \int_{-\pi/2}^{\pi/2} \cos(\theta)(CR - \frac{k_0 R^2}{2}) d_\theta = 2(CR - \frac{k_0 R^2}{2})$$

$$\alpha_{area} = 2 \cdot \alpha_{semi-area} = 4(CR - \frac{k_0 R^2}{2})$$

$$\alpha_{BA} = 2 \cdot \alpha_{OA} = 2 \cdot \int_{0}^{R} (C - k_0 x) d_x = 2(CR - \frac{k_0 R^2}{2})$$

$$\frac{\alpha_{area}}{\alpha_{BA}} = 2$$

Case 3: Assuming the absorption is parabolic with the radial distance r, i.e. $\alpha = C - \frac{k_0 r^2}{2}$

$\alpha_{semi-area}$

$$= \int_{-\pi/2}^{\pi/2} d\theta \int_{0}^{R\cdot\cos(\theta)} (C - \frac{k_0 r^2}{2}) d_x = \int_{-\pi/2}^{\pi/2} d\theta \int_{0}^{R\cdot\cos(\theta)} (C - k_0 \frac{x^2}{2 \cdot \cos^2(\theta)}) d_x$$

$$= \int_{-\pi/2}^{\pi/2} \cos(\theta)(CR - \frac{k_0 R^3}{6}) d_\theta = 2(CR - \frac{k_0 R^3}{6})$$

$$\alpha_{area} = 2 \cdot \alpha_{semi-area} = 4(CR - \frac{k_0 R^3}{6})$$

$$\alpha_{BA} = 2 \cdot \alpha_{OA} = 2 \cdot \int_{0}^{R} \left(C - \frac{k_0 r^2}{2} \right) d_x = 2 \int_{0}^{R} \left(C - k_0 \frac{x^2}{2} \right) d_x = 2(CR - \frac{k_0 R^3}{6})$$

$$\frac{\alpha_{area}}{\alpha_{BA}} = 2$$

Appendix 2

1.   Introduction

Medwell *et al.* [1] proposed that the external radiation can interact with the flame through two mechanisms: gas phase absorption and soot absorption. This supplement aims to estimate the relative significance of these two mechanisms for the case of broadband solar irradiation.

2.   Methodology

2.1.   Absorption by gaseous species

The molecular absorption of radiation can be described by the spectral line intensity with a unit of $cm^{-1}/(molecule\ cm^{-2})$ [2]:

$$S_{\eta\eta'} = \frac{h\nu}{c}\frac{n_\eta}{N}(1 - \frac{g_\eta}{g_{\eta'}}\frac{n_{\eta'}}{n_\eta})B_{\eta\eta'}\ ,\tag{1}$$

where h is the Planck constant, c is the speed of light, ν is the frequency of radiation, $B_{\eta\eta'}$ is the Einstein coefficient for induced absorption, n_η and $n_{\eta'}$ are the populations of the lower and upper states, respectively, g_η and $g_{\eta'}$ are the state statistical weights, and N is the molecular number density. The weight includes electronic, vibrational, rotational and nuclear statistics.

The spectral line intensity ($S_{\eta\eta'}$) can be calculated for many molecules in the HITRAN database [2]. Importantly, the intensity defined in Eqn 1 is for a single molecule. Multiplying Ndx to $S_{\eta\eta'}$ gives the fraction of absorption for a light beam at frequency ν while traveling an optical distance dx at a molecular number density of N. The current study adopted this methodology to estimate the fraction of absorption for the incident radiation.

Figure A2 shows the transmittance spectra of atmospheric gases CO, N_2O, CH_4, O_2, O_3, CO_2 and H_2O ranging from 300 nm to 50000 nm, using data acquired from the HITRAN 2008 spectroscopic database [3]. It has been shown in our previous work that the spectral irradiance of the metal halide lamp is negligible beyond 1600 nm [4]. Therefore, for the current study, only absorption bands ranging 300-1600 nm are of interest. It can be seen in Figure A2 that, below 1600 nm, H_2O is the major gas phase media that absorb broadband radiation, with three absorption bands centred at 950,

1130 and 1410 nm, respectively. The absorption of the rest of the atmospheric gases is negligible below 1600 nm, except for O_3, whose absorption in the UV range is noticeably high. However, because there is presumably no O_3 in the Santoro flame for the current work, the O_3 absorption can be ignored as well. Therefore, H_2O is the only molecule of interest for the current assessment of atmospheric gases.
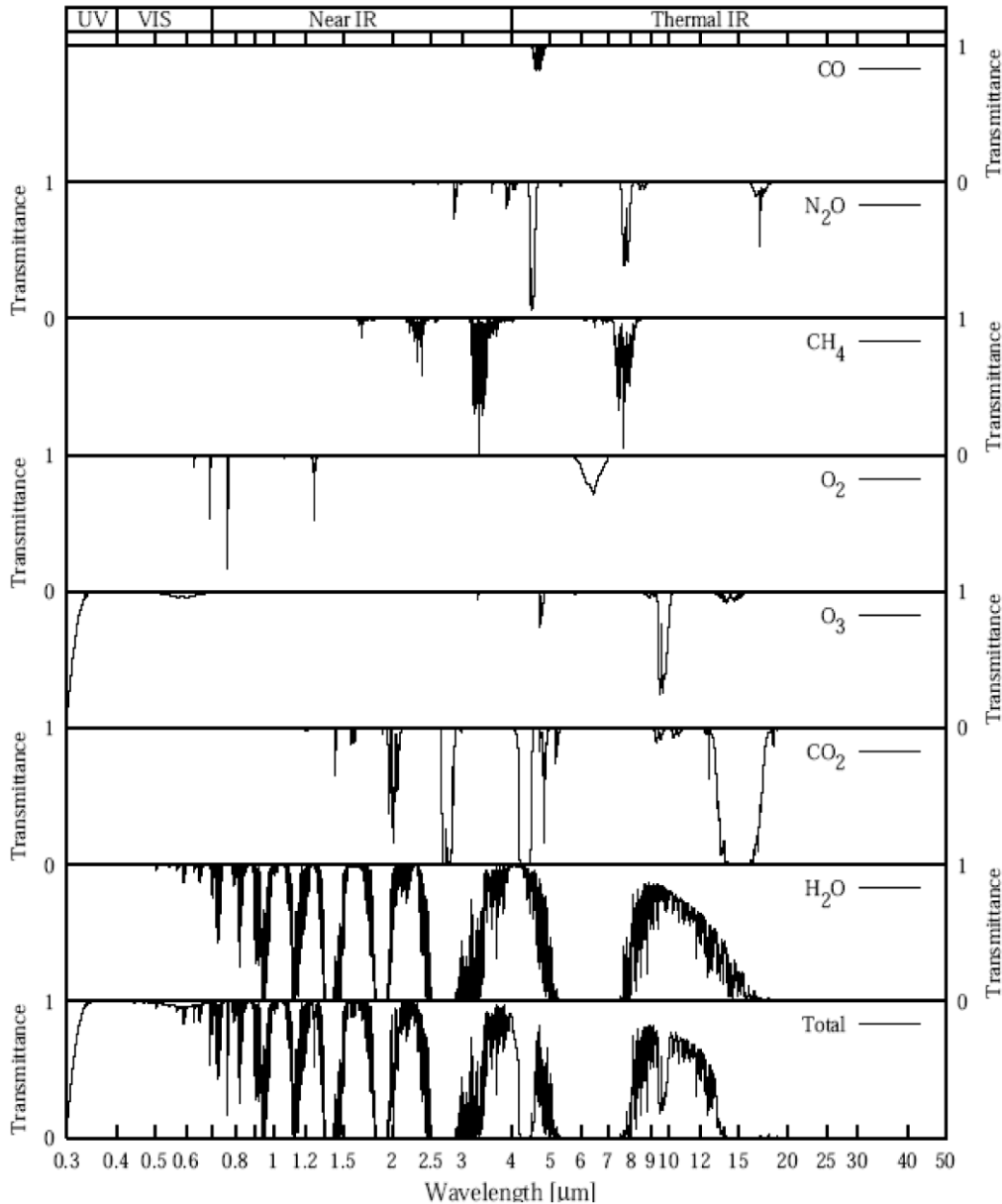

Figure A2. Transmission spectra of the major atmospheric gases [3].

In addition to the atmospheric gases, there are also flammable gas phase species in the flame such as C_2H_4, C_2H_2, A_1 to A_4 and PAH etc. Among these gases, the absorption of C_2H_4 can be considered to be negligible, because its major absorption bands range 3084-14265 nm [2], which is

outside the spectral range of the lamp. Figure A3 shows the absorption lines within the lamp spectrum of H_2O, C_2H_2, A_1 and an example form of PAH. It can be seen that, at atmospheric temperature, H_2O absorbs infrared radiation ranging from 800-1600 nm [3], C_2H_2 absorbs infrared radiation ranging from 1000-1600 nm [3, 5], benzene (A_1) absorbs UV radiation ranges 235-270 nm [6] and PAH also absorb UV radiation of different spectral range depends on their molecular composition. It can also been seen from Figure 7 of the main text that the concentration of C_2H_2, A_1 and A_4 is noticeably high at HAB<32 mm. Therefore, the absorption of these species at the upstream locations is expected to be responsible for the upstream translation of the soot inception, as is discussed in the main text.
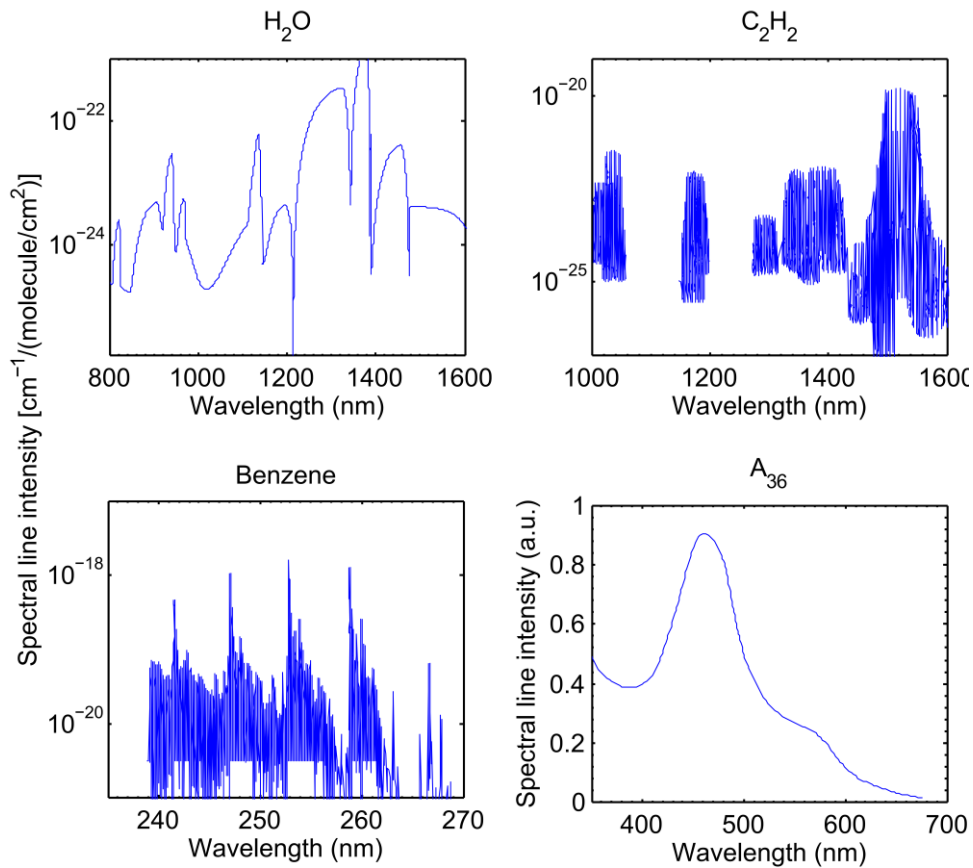

Figure A3. Spectral line intensity for the H_2O [3] and C_2H_2 [5] at 296 K, and that for benzene [6] at 293 K and A_{36} at room temperature [7, 8]. The spectral line intensity for A_{36} used arbitrary unit because the absolute unit is not available from the literature to our knowledge.

Table 1 lists the key parameters used to estimate the energy absorbed by some important molecular species. The overlap between molecular absorption bands and lamp spectrum can be employed to estimate the fraction of the lamp radiation that can potentially be absorbed by the molecules. The

spectral line intensity ($S_{\eta\eta'}$) shown in Table 1 was spectrally averaged from the data shown in Figure 12. N was estimated using the spatially averaged concentration of these molecules in the flame based on the modelling work of Liu *et al.* [9]. Multiplying $S_{\eta\eta'}$ with N, optical path length of the radiation and the absorption wavebands gives the fraction of the energy within the solar spectrum that is absorbed by this molecular species. The absorbed energy shown in the last column is estimated by multiplying the lamp radiation in the spectral absorption range with fraction of absorption.

Table A1. The molecular absorption of solar radiation in the Santoro flame. The total solar energy applied to the flame is 138W.

Molecule	Overlap between molecular absorption bands and lamp spectrum (nm)	$S_{\eta\eta'}$ [cm^{-1}/(molecule cm^{-2})]	$\int_{-R}^{R} N dx$ [molecule cm^{-2}]	Fraction of absorption $\int_{\lambda_1}^{\lambda_2} \int_{-R}^{R} N dx \times S_{\eta\eta'} \times d\lambda$	Energy absorbed (W)
H_2O	900-1500	6.91×10^{-23}	6.7×10^{17}	0.0278	0.961
C_2H_2	1000-1600	1.05×10^{-22}	1.29×10^{17}	0.0081	0.151
A_1	238-263	3.12×10^{-19}	1.80×10^{15}	0.0141	0.0005
A_4	300-700	3.94×10^{-18} *	2.85×10^{12}	0.0045	0.0025

* The absorption spectrum of A_4 is assumed to be the same with that of A_{36} as is shown in Figure A3. The order of magnitude for the spectral line intensity of A_4 is assumed to be 10^{-18} because it is currently unknown.

It can be seen from the last column of Table A1 that the absorption of gas phase species like H_2O, C_2H_2, A_1 and A_4 are expected to have limited effect on the temperature of the flame, because their absorption is estimated to be at least 1 order of magnitude lower than the overall flame absorption. Nevertheless, the absorption of C_2H_2, A_1 and A_4, despite of being minor, is expected to be the key factor driving the upstream translation of the soot formation.

It is noteworthy that we have estimated the molecular absorption based on the absorption spectra of gases at atmospheric temperature, while actual gases will be at elevated temperatures of up to flame temperature. The exact level of uncertainty associated with this approximation is unknown, but is expected to be much better than order of magnitude, so is sufficient to support the conclusion.

2.2. Absorption by Soot

The absorption of external irradiation by soot is estimated based on the beam attenuation theory, where the ratio of the attenuated beam to the incident beam intensity (I/I_0) depends on soot volume fraction, optical path length and wavelength of radiation. The extinction rate can be estimated using Bouguer's law if soot dimensions are assumed to be within the Rayleigh limit for spherical particles ($\frac{\pi d_p}{\lambda} < 0.3$) with respect to incident light source [10, 11]. Bouguer's law for light extinction can be expressed as follows [11]:

$$\frac{I}{I_0} = e^{-K_{ext}L} \quad , \tag{5}$$

where L is the optical path through the flame, K_{ext} is the extinction coefficient. This can be expressed as follows:

$$K_{ext} = \frac{6\pi E(m) \cdot f_v}{\lambda} \quad , \tag{6}$$

where $E(m)$ is a function of refractive index of soot, f_v is the soot volume fraction, λ is the wavelength of the incident light source.

For the current estimation, $E(m)$ is assumed to be 0.30, independent from wavelength and soot particle size; f_v is averaged to be 2 ppm within the flame; L is taken to be 6.5 mm averaged from all HABs. Therefore, the global attenuation rate of the flame due to soot absorption is estimated and plotted as a function of wavelength in Figure A4. This figure also plots the spectral irradiance of the metal halide lamp. The product of these two curves show that the soot absorption accounts for 8.5% of the lamp irradiance, for this case 11.7 W. This matches to within 3% the total estimated flame absorption as reported in Figure 9 of the main text.

Importantly, the current assessment estimates the total absorption of molecules and soot without accounting for the spatial distribution of species, incident radiation and hence the absorbed radiation. Additionally, the refractive index of soot is also assumed to be constant regardless of wavelength and soot size. Nevertheless, the estimation of soot absorption agrees with the

extinction measurement using 1064 nm laser beam, which shows that the absorption is 7.45% averaged from four HABs 15, 25, 35, 40 mm as is shown in Figure A4. This comparison shows that the difference between the current estimate and the laser extinction measurement is within 11%, which is sufficiently accurate to demonstrate that absorption by soot dominates over that of gas phase species.
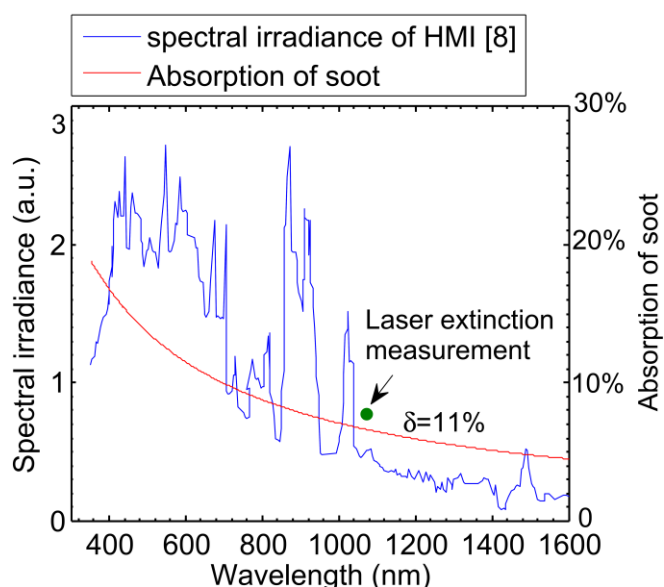

Figure A4. Radiant absorption spectrum of soot in the Santoro flame, together with the spectral irradiance of the metal halide lamp [12].

3.   Conclusion

The current assessment of global absorption of molecules and soot shows that:

The absorption of solar radiation by gas phase molecules is dominated by H_2O, which is small but significant, contributing some 8% to the total energy absorbed by the flame. The contribution of other gas phase species like O_2, CO_2 and C_2H_4 to the total energy absorbed is negligible for the current study, because there are few absorption bands of these molecules in the lamp spectrum. Soot absorption is estimated to be the dominant mechanism in this process, as it is in the same order of magnitude with the overall flame absorption.

The absorption of solar radiation by gas phase like C_2H_2, A_1 and A_4 is expected to be the key factor driving the upstream translation of the soot inception, as their absorption lines partially overlap with the lamp spectrum and their concentration in the upstream locations is significant. However, these molecular absorption is expected to have limited effect on the total radiation absorbed,

because their absorption is estimated to be at least one order of magnitude lower than the overall

flame absorption.

1.   P. R. Medwell; G. J. Nathan; Q. N. Chan; Z. T. Alwahabi; B. B. Dally, Combustion and Flame 158 (9) (2011) 1814-1821
2.   L. S. Rothman; C. Rinsland; A. Goldman; S. Massie; D. Edwards; J. Flaud; A. Perrin; C. Camy-Peyret; V. Dana; J.-Y. Mandin, Journal of Quantitative Spectroscopy and Radiative Transfer 60 (5) (1998) 665-710
3.   L. S. Rothman; I. E. Gordon; A. Barbe; D. C. Benner; P. F. Bernath; M. Birk; V. Boudon; L. R. Brown; A. Campargue; J. P. Champion; K. Chance; L. H. Coudert; V. Dana; V. M. Devi; S. Fally; J. M. Flaud; R. R. Gamache; A. Goldman; D. Jacquemart; I. Kleiner; N. Lacome; W. J. Lafferty; J. Y. Mandin; S. T. Massie; S. N. Mikhailenko; C. E. Miller; N. Moazzen-Ahmadi; O. V. Naumenko; A. V. Nikitin; J. Orphal; V. I. Perevalov; A. Perrin; A. Predoi-Cross; C. P. Rinsland; M. Rotger; M. Šimečková; M. A. H. Smith; K. Sung; S. A. Tashkun; J. Tennyson; R. A. Toth; A. C. Vandaele; J. Vander Auwera, Journal of Quantitative Spectroscopy and Radiative Transfer 110 (9–10) (2009) 533-572
4.   X. Dong; Z. W. Sun; G. J. Nathan; P. J. Ashman; D. H. Gu, Solar Energy 115 (2015) 613-620
5.   L. S. Rothman; R. Gamache; R. Tipping; C. Rinsland; M. Smith; D. C. Benner; V. M. Devi; J.-M. Flaud; C. Camy-Peyret; A. Perrin, Journal of Quantitative Spectroscopy and Radiative Transfer 48 (5) (1992) 469-507
6.   S. Fally; M. Carleer; A. C. Vandaele, Journal of Quantitative Spectroscopy and Radiative Transfer 110 (9–10) (2009) 766-782.
7.   Ž. Tomović; M. D. Watson; K. Müllen, Angewandte Chemie International Edition 43 (6) (2004) 755-758
8.   M. G. Debije; J. Piris; M. P. de Haas; J. M. Warman; Z. Tomovic; C. D. Simpson; M. D. Watson; K. Müllen, Journal of the American Chemical Society 126 (14) (2004) 4641-4645
9.   F. Liu; S. B. Dworkin; M. J. Thomson; G. J. Smallwood, Combustion Science and Technology 184 (7-8) (2012) 966-979
10.   A. D'alessio; A. Di Lorenzo; A. Sarofim; F. Beretta; S. Masi; C. Venitozzi in: *Soot formation in methane-oxygen flames*, Symposium (International) on Combustion, 1975; Elsevier: 1975; pp 1427-1438.
11.   R. J. Santoro; C. R. Shaddix, Applied combustion diagnostics (2002) 252-286
12.   *MetalL Halide Lamps and Photo Optics*, OSRAM.

CHAPTER 6

GLOBAL CHARACTERITICS OF NON-PREMIXED JET FLAMES OF HYDROGEN-HYDROCARBON BLENDED FUELS

Xue Dong[1, 2, *], Graham J. Nathan[1, 3], Saleh Mahmoud[1, 3], Peter J. Ashman[1, 2], Dahe Gu[1, 3], Bassam B. Dally[1, 3]

[a] *Centre for Energy Technology, The University of Adelaide, SA 5005, Australia*
[b] *School of Chemical Engineering, The University of Adelaide, SA 5005, Australia*
[c] *School of Mechanical Engineering, The University of Adelaide, SA 5005, Australia*

Statement of authorship

Title of Paper	Global characteristics of non-premixed jet flames of hydrogen-hydrocarbon blended fuels
Publication Status	☑ Published ☐ Accepted for Publication ☐ Submitted for Publication ☑ Publication Style
Publication Details	Combustion and Flame 162 (2015) 1326-1335

Principal Author

Name of Principal Author (Candidate)	Xue Dong		
Contribution to the Paper	Under the supervision of P. J. Ashman and G. J. Nathan, I developed the experimental methods, performed the experiments, processed the data and wrote the manuscript.		
Overall percentage (%)	55%		
Signature		Date	01/09/2015

Co-Author Contributions

By signing the Statement of Authorship, each author certifies that:

    x.   the candidate's stated contribution to the publication is accurate (as detailed above);

    xi.   permission is granted for the candidate in include the publication in the thesis; and

    xii.   the sum of all co-author contributions is equal to 100% less the candidate's stated contribution.

Name of Co-Author	Peter J. Ashman		
Contribution to the Paper	I acted as primary supervisor for the candidate, aided in developing of the experimental method and evaluating the final version of the manuscript. I give consent for Xue Dong to present this paper for examination towards the Doctorate of Philosophy.		
Signature		Date	9/9/15

Name of Co-Author	Graham J. Nathan		
Contribution to the Paper	I acted as secondary supervisor for the candidate, aided in developing of the experimental method, revising the manuscript and evaluating the final version of the manuscript. I give consent for Xue Dong to present this paper for examination towards the Doctorate of Philosophy.		
Signature		Date	10/9/15

Name of Co-Author	Saleh Mahmoud
Contribution to the Paper	I am a fellow PhD student, aided in designing the experimental facility, performing the experiments and evaluating the final version of the manuscript. I give consent for Xue Dong to present this paper for examination towards the Doctorate of Philosophy.
Signature	Date 11 / 9 / 2015

Name of Co-Author	Dahe Gu
Contribution to the Paper	I am a fellow PhD student, aided in performing the experiments and evaluating the final version of the manuscript. I give consent for Xue Dong to present this paper for examination towards the Doctorate of Philosophy.
Signature	Date 1 / 9 / 2015

Name of Co-Author	Bassam B. Dally
Contribution to the Paper	I am a professor who co-supervised the experimental campaign, aided in designing the experimental facility, revising the manuscript and evaluating the final version of the manuscript. I give consent for Xue Dong to present this paper for examination towards the Doctorate of Philosophy.
Signature	Date 10 / 9 / 15

CrossMark

Global characteristics of non-premixed jet flames of hydrogen–hydrocarbon blended fuels

Xue Dong [a,b,*], Graham J. Nathan [a,c], Saleh Mahmoud [a,c], Peter J. Ashman [a,b], Dahe Gu [a,c], Bassam B. Dally [a,c]

[a] Centre for Energy Technology, The University of Adelaide, Adelaide, SA 5005, Australia
[b] School of Chemical Engineering, The University of Adelaide, Adelaide, SA 5005, Australia
[c] School of Mechanical Engineering, The University of Adelaide, Adelaide, SA 5005, Australia

ARTICLE INFO

ABSTRACT

Blending hydrogen into hydrocarbon fuels can reduce the carbon-intensity of the fuel and extend the lean flammability limit. However, limited information is available of the global performance of attached, non-piloted hydrogen–hydrocarbon jet flames under well-defined boundary conditions. Three groups of blended fuels were investigated in the current study: Natural gas +H_2 (with H_2 volume fraction varying from 18.6% to 100%), C_2H_4 + H_2 (with H_2 volume fraction varying from 0% to 100%), and 40% C_2H_4 + 41% H_2 + 19% N_2. Measurements were performed of flame dimensions, radiant fraction, and emission indices of NO_x and CO. For flames with constant exit strain rate, the increase of hydrogen volume fraction was found to decrease the radiant fraction, decrease the global residence time and increase the NO_x emission index. For flames of the same fuel composition, a higher strain rate results in a lower radiant fraction. The NO_x production rate scales with the reciprocal of non-adiabatic flame temperature, consistent with the thermal NO_x mechanism. The CO/CO_2 ratio is determined by the competing influences of flame residence time, carbon input rate and mixing rate of the fuel and air.

© 2014 The Combustion Institute. Published by Elsevier Inc. All rights reserved.

1. Introduction

There is growing interest in the use of blended hydrogen and hydrocarbon gaseous fuels because of their complementary nature. Hydrogen can be produced from intermittent renewable energy resources, such as wind and solar, to achieve a near carbon–neutral energy source. Fossil-derived hydrocarbon fuels are usually available continuously and at a lower cost, but are non-renewable and have a high carbon-intensity. Hence it can be desirable to blend these fuels to lower the carbon-intensity of the blend relative to fossil fuels, whilst maintaining a continuous supply. In addition, blending can avoid the need to store hydrogen and reduce the risk of flashback relative to pure hydrogen [1], which will potentially lower the cost of its use. Furthermore, the addition of hydrogen to a hydrocarbon fuel will increase the flame speed and extend the lean flammability limit [2], which offers the potential to operate lean combustion technologies closer to the lean limit and thereby suppress NO_x emissions. However, the non-linear nature of turbulent combustion processes means that it is impossible to predict the properties of flames from a blended fuel on the basis

of the flames of the pure components. The addition of hydrogen to a hydrocarbon fuel also reduces soot generation, thus reducing flame emissivity. Furthermore, hydrogen has a much higher molecular diffusivity, which can result in well-known differential diffusion effects. The combination of these different effects means that direct measurements of the global properties of flames from blended fuels are needed.

Although the global performance of blended fuels has been measured previously as is shown in Table 1, significant gaps remain. Choudhuri et al. [3] measured a series of turbulent diffusion flames with a Reynolds number of 8,700, while Wu et al. [4] reported measurements of the lift-off and blow-off stability limits of pure hydrogen and hydrogen/hydrocarbon blended jet flames. However, not all of these flames were attached to the burner. Where lift-off occurs it is impossible to isolate the chemical effects due to the addition of H_2 from those of the different physical entrainment mechanisms for lifted and attached flames. Therefore, there remains a need to investigate the effect of varying the hydrogen volume fraction for flames that are all attached. The previous measurements of Turns and Myhr [5], were performed with hydrocarbon fuels surrounded by a hydrogen pilot, which is not the same as blended fuel, while the measurements of El-Gafour et al. [6] were limited to natural gas as the hydrocarbon component and

---

* Corresponding author.
  E-mail address: xue.dong@adelaide.edu.au (X. Dong).

to a maximum hydrogen volume fraction of 50%. Furthermore, no previous hydrogen–hydrocarbon flames have been investigated under constant exit strain rate, u/d, which strongly influences the axial and radial soot volume fraction profiles [7,8]. There is therefore a need to assess the influence of hydrogen blending on a series of attached, non-piloted flames at constant strain, spanning the full range of blend ratios.

It is also important to note that none of the previous global flame measurements have been performed under boundary conditions that are sufficiently well defined to enable them to be modelled unambiguously. The development and validation of a computational fluid dynamics (CFD) model requires that the inflow boundary conditions, such as the mean and RMS velocity profiles, be reported. The process of model development and validation also requires sufficient detailed in-flame measurements to be reported for the same flames, to enable the sources of radiation, notably from the presence of soot, to be linked unambiguously to the global emissions of pollutant gases and radiation. Importantly, none of the previous global measurements of flames associated with hydrogen blends have either reported the inflow boundary conditions or are linked to other detailed in-flame measurements of parameters such as temperature and soot volume fraction. The recent advances in experimental techniques suitable for application in turbulent flames [9] means that it is now possible to achieve this. For example, a series of detailed measurements of soot volume fraction and temperature have recently been undertaken for four flames of a particular blend of 40% C_2H_4 + 41% H_2 + 19% N_2 (hereafter referred to as "ENH flames"), carefully chosen to achieve attached, turbulent flames without a pilot. The first of these measurements are reported by Mahmoud et al. [10], who report joint statistics of soot volume fraction and flame temperature from simultaneous measurements of these parameters. There is therefore also a need for global measurements of flame radiation and emissions to be reported for these flames. It is also significant for such measurements to be performed with both C_2H_4 and natural gas as the hydrocarbon fuels, since C_2H_4 is the hydrocarbon fuel whose sooting characteristics are best understood, while natural gas is the gaseous fuel of greatest practical significance.

In light of the above background, the aim of the current investigation is to assess the effect of hydrogen blend ratio on the global performance of non-premixed jet flames under well-defined conditions and for a data series linked to selected flames for which detailed, in-flame data are available [10]. In particular, it aims to assess this influence both with C_2H_4 and natural gas as the hydrocarbon fuels, with hydrogen volume fraction ranging from 0% to 100% at constant exit strain rate. Since flames with constant strain rate necessarily results in varying Re, a group of ENH flames with constant Re were also measured to isolate the effects of Re.

2. Methodology

The experimental arrangement is shown in Fig. 1. A co-flow burner providing a low-velocity concentric air jet around a central fuel jet was used. The co-flowing air jet is of square cross-section (150 mm × 150 mm) generated by a fan, through flow conditioning comprising screens in a settling chamber, followed by a smooth contraction nozzle to form a uniform flow. The fuel jet was supplied by a straight tube of 385 mm length and aligned to protrude 18 mm above the top of the air jet. Three fuel nozzles were used of inner diameter 4.4 mm, 5.8 mm and 8 mm. The relative position of the flame tip and exhaust hood was adjusted to be constant at 300 mm.

Figure 2 presents the velocity profiles of the fuel jet and co-flowing air jet, as measured by a hot-wire anemometer at the burner nozzle level (18 mm above the nozzle of co-flowing air). The substitution of fuel with air for the measurement of velocity is based on the assumptions that the flow in the pipe is both iso-thermal and inert (i.e. that there are no chemical reactions or thermal gradients within the pipe). These assumptions are reasonable because the temperature of external surface of the fuel pipe was measured to be about 35 °C for our turbulent flames. It can be seen that the free-stream velocity of the co-flowing jet of air was 1.1 m/s in every case, with good flow symmetry. The exit velocity profiles for the three fuel jet cases are also reported for non-reacting conditions, measured using air. The time-averaged velocity U normalized by the central line velocity U_{cl} (hereafter referred to as mean velocity), and standard deviation of the instantaneous velocity u' normalized by time-averaged velocity U (hereafter referred to as r.m.s velocity) are plotted as a function of r/D, as is shown in Fig. 2. Also shown in Fig. 2 are the exit mean velocity profiles in comparison with the measurements of Mi et al. [17], as well with the power-law profile of $\frac{U}{U_{cl}} = \left(1 - 2 \times \frac{r}{D}\right)^{\frac{1}{n}}$, with $n = 7$ for fully developed turbulent pipe flow [18]. It can be seen that the present jet data conforms closely with both previous measurements and with the theoretical profile, although some differences were recorded between the exit profiles of the different pipes. The numerical values of these data are also reported on the ISF website [19].

The properties and specifications of the natural gas +H_2 (hereafter referred to as "NGH flames"), the C_2H_4 + H_2 blended flames (hereafter referred to as "EH flames"), and ENH flames are presented in Tables 2–4. The composition of the natural gas is shown in Table 5. Four of the ENH flames, ENH_1, ENH_2, ENH_3 (hereafter referred to as ENH_1–3)and ENH_7, were also chosen for detailed investigation by laser diagnostics, and are reported elsewhere by Mahmoud et al. [10], with the numerical values of the data reported on the ISF website. The conditions selected for the ENH flames were based on a systematic assessment of the performance of flames from different blended fuels to achieve as a high Reynolds number as possible for the limiting case in the series, whilst maintaining an attached flame.

The flow rates of fuels were measured using ABB rotameters, calibrated with an ALICAT MC-series mass flow controller to within ±2%. All flow rates were corrected to the standard condition (21.1 °C, 101.325 kPa). A wide range of flow conditions were assessed for the blended fuels, with the upper limit determined by the lift-off velocity of the flame. The hydrogen flow rate was increased from the minimum necessary to obtain an attached blended flame to the maximum, which is pure hydrogen.

The jet exit velocity reported in Tables 2–4 is the bulk mean value (based on volume flow rate and nozzle area).

2.1. Radiant intensity measurements

A Schmidt–Boelter gauge (manufactured by Medtherm Corporation) was used as the sensor to measure the total radiation from the jet diffusion flames. The heat flux sensor is covered with a sapphire window to transmit 85% nominal radiation over the range of 0.15–5 microns, with a view angle of 150° [21].

The transducer was positioned at a radial distance of 280 mm from the vertical (x) axis of the flame and traversed parallel to it with ±0.5 mm precision. Ten thousand samples were collected at 1000 Hz and averaged to obtain the radiative flux at each of 25 equi-spaced heights, starting at the nozzle exit plane (±0.5 mm) and ending at the flame tip. This was found to be sufficient for statistical convergence [22]. The measurement uncertainty depends on the increment of equal spaced sampling, with a smaller increment leading to a better approximation. However, in our case, the 25 points was deemed to be sufficient because it resolved

Table 1
A review of previously reported measurements of hydrogen–hydrocarbon flames.

Source	Condition	Jet diameter (mm)	Coflow air	Re	Fuel composition	Maximum hydrogen volume fraction (%)	Characteristics presented	Pollutant emissions measured
[3]	Turbulent jet diffusion	1, 2.3, 3.8, and 4.5	no	8,700	H_2 + natural gas	35	Flame length, pollutant emission, radiative heat loss fraction, and volumetric soot concentration	NO, NO_x, CO
[6]	Turbulent jet diffusion	3.5	0.4 m/s	4000	H_2 + natural gas	50	Lift off and blow out, flame length, flame temperature distribution, and pollutant emissions	NO, CO, O_2, CO_2
[1], [11], [12]	Laminar	2	no	150	H_2 + natural gas	100	Flame length, radiative fraction of heat release, pollutant emission	O_2, NO, NO_x, CO,CO_2, T, SVF
					H_2 + propane		indices and in-flame profiles of composition and temperature	(O, H, OH, PAH,CH,CN)
[4]	Laminar and turbulent	2	no	200–8000	H_2, H_2/C_3H_8, H_2/CO_2, C_3H_8 and H_2/Ar		Lift-off, blow-out and blow-off stability limits	
[2]	Laminar premixed	2.8	Premixed	1300	$CH_4 + H_2 + O_2$ + air	10	Separately visualize two-dimensional (2-D) distributions of net OH radical fluorescence intensities produced from CH4-O2-air and H2–O2–air combustion reactions	
[13]	Laminar diffusion flames	5	0.033	982	LPG + H_2	40	Flame length, soot free length fraction (SFLF), and emission level	NO_x, CO,CO_2
[14]	Laminar	Bunsen burner 13 ID	Premixed	1500	LPG + H_2 + air	50	Laminar burning speed, flame temperature, impingement heat transfer	NO_x emission , CO emission
[15]		Coaxial rich-lean burner	Rich mixture + lean mixture		$CH4 + H_2$ + air H_2 + air	58.3		NO and NO_2
[5]	Turbulent pilot flames	4.12	no	4000–15,000	CH_4	67	Flame length, radiant fraction, NO_x emission	CO, CO_2 and NO_x
					C_3H_8 C_2H_4 CO/H_2			
[16]	Laminar	Spark-ignition engine			H_2 + CH_4	30	Cylinder pressure and brake thermal efficiency	CO, CO_2 and HC
Current measurement	Turbulent and laminar diffusion	4.4	1.1	967–17,812	H_2 + natural gas H_2 + C_2H_4	100	Flame length, pollutant emission, radiative heat loss fraction	NO, NO_x, CO, CO_2
					$H_2 + C_2H_4 + N_2$			

the profile to within ±2%. On this basis, incorporating the ±3% uncertainty of the heat flux gauge, the overall uncertainty of radiant fraction measurement was ±5%.

2.2. Flame shape measurement

A tripod mounted camera (Canon EOS 6D) with a pixel array of 3168×4752, an A/D conversion of 14 bits and a shutter speed as high as 1/4000 s was used to freeze the transient shape of the images. The shape of each flame was averaged from 42 images; The signal to noise ratio (SNR) of each pixel cell is defined by Eq. (1).

$$SNR = \frac{\mu_{sig}}{\mu_{bg}} \qquad (1)$$

Here μ_{sig} is the pixel intensity of the signal cell, and μ_{bg} is the average pixel intensity of background.

As is shown in Fig. 3, the boundary of flame in each image is identified by the pixel cell with a SNR greater than 50. The instantaneous length of the flame from each image was defined as the distance between the burner nozzle and the most

downstream flamelet, while the width of flame is defined as the widest part of the flame, following Langman et al. [22]. The flame dimensions acquired in this way are repeatable to within ±3% uncertainty.

2.3. Global emissions measurement

Global emissions of NO, NO_x, CO and CO_2 were measured continuously for each flame using a commercially calibrated Testo 350 flue gas analyzer. A mixture of the combustion products and ambient air was sampled from the flame tip. The CO_2 concentration was measured to calculate the extent of sample dilution with air. The emission rate of CO was expressed as the CO/CO_2 ratio while the emission indices of oxides of nitrogen are presented in g/MJ fuel. The accuracy of NO and NO_x sensors is ±5 ppm (0–99 ppm), and that of CO and CO_2 is ±5% (under 2000 ppm) and ±0.3 Vol.% (under 25% CO_2) respectively. The NO_x emission in the present measurements is up to 30 ppm, and that of CO and CO_2 is up to 250 ppm and 0.07–3.5% respectively. The resolution of NO, NO_x and CO sensors is 1 ppm, and that of CO_2 is 0.01 Vol.%.
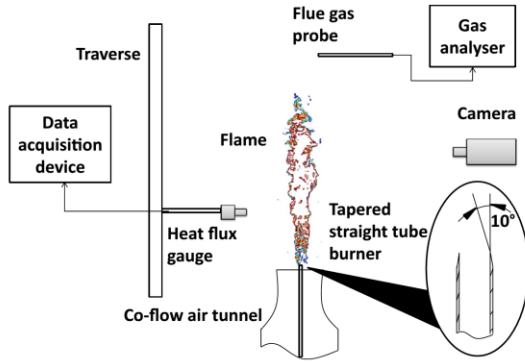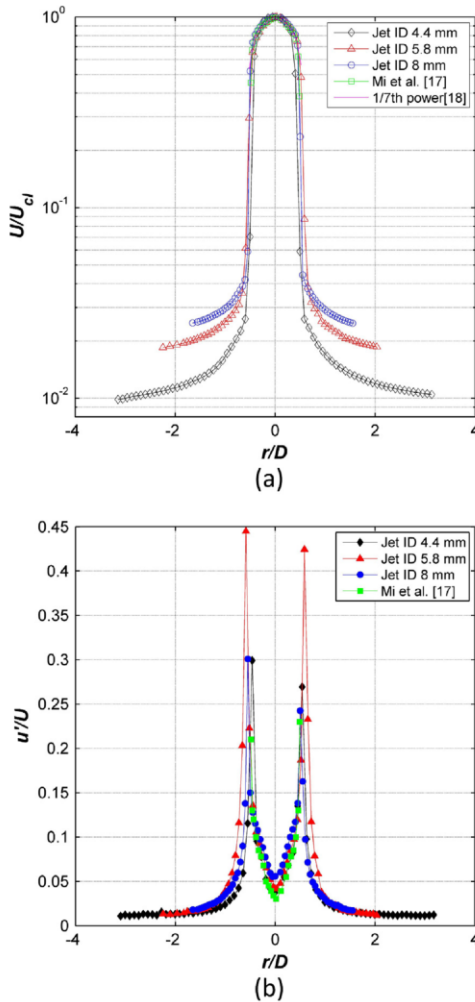
Fig. 1. Experimental arrangement.

Fig. 2. Mean (a) and r.m.s (b) velocity profiles of non-reacting flow at $x = 1$ mm above the fuel jet, with central fuel jet diameters of 4.4 mm, 5.8 mm and 8 mm respectively; Mean velocity also compares with previous measurements of Mi et al. [17], and the 1/7th power-law profile [18].

3. Results and discussion

3.1. Radiant heat flux

Figure 4a presents the axial heat flux distribution measured at a radial distance of 280 mm from the nozzle axis. The radiant fraction of the blended fuels was found to decrease with an increase in the hydrogen volume fraction, which is consistent with the expected trend that soot concentration decreases with a reduction in the C/H ratio [13]. This shows that the radiation is dominated by the presence of soot, which proceeds through the stages of inception, nucleation, growth and oxidation as the fuel is transported through the flame envelope. Radiation peaks in the range of $0.35 < x_p/L_f < 0.5$, which typically corresponds approximately to the region of maximum soot volume fraction [10]. Here x_p is the axial distance to the peak heat flux. Significantly, the value of x_p/L_f also increases as the volume fraction of hydrogen is increased. That is, the presence of hydrogen delays the soot formation and shifts the radiant peak downstream.

In contrast, the peak heat flux from the flames of 40% $C_2H_4 + 41\%$ $H_2 + 19\%$ N_2 (*ENH_1-3* and *ENH_7*), shown in Fig. 4b, was found further downstream, in the range of $0.5 < x_p/L_f < 0.8$. This is due to the presence of N_2 in the fuel mixture, which is also known to reduce the amount of soot in the flame and hence the thermal radiation. It can also be seen that x_p increases with a reduction in the exit strain rate, u/d, at constant Re. This is because a decrease in strain rate corresponds with a reduction in Fr_e, and therefore to a condition more strongly influenced by buoyancy. The non-dimensional flame length, ξ_L, defined by Becker and Yamazaki [20] was also used to quantify the effect of buoyancy. As is shown in Table 4, all *ENH flames* are in the range $2 < \xi_L < 10$, which means these flames are transitional, between the momentum- and buoyancy-driven regimes. Direct measurement of the effect of buoyancy on the structure of turbulent jet diffusion flames has been reported by Mungal et al. [23], which shows that the celerity of a combusting structure remains constant along the majority of the flame length with a value of $12 \pm 2\%$ of the jet exit velocity. This implies that the celerity is lower for buoyancy dominated flame than for a flame dominated by momentum [24]. They also noted a greater tendency of the flame-tip to separate under momentum-dominated than under buoyancy–dominated conditions [23], which is further evidence of differences in the mixing dynamics between the two regimes. On this basis, this shift in x_p seems to be associated with the transition from the momentum-dominated to the buoyancy-dominated regimes, although this influence is only one of many so that an increase of ξ_L does not necessarily shift x_p downstream for all cases.

3.2. Influence of Re and strain rate on radiant fraction

The radiation fraction χ_r is defined by the Eq. (2).

$$\chi_r = \frac{Q_r}{Q_F} = \frac{2\pi R \cdot \int_0^\infty q''(\dot{x})dx}{\dot{m} \times H\dot{H}V} \tag{2}$$

where Q_r is the total radiated power (kW), Q_F is the flame's output power (kW), R is the radial distance from the nozzle exit to the transducer, $\int_0^\infty q''(\dot{x})dx$ is the total axial radiative flux (kW/m²), $\dot{m}$ is the mass flow rate of the fuel, and $H\dot{H}V$ is the higher heating value of the fuel [22].

It can be seen from Fig. 5 that, increasing u/d from 2000 to 10,000 s^{-1} at constant Re results in a reduction in χ_r by approximately 50%. While this trend is to be expected, no measurements of this trend have been available previously. Overall, the three data sets (Re = 8860, Re = 11,900 and Re = 15,200) are consistent with χ_r

Table 2
Details of the NGH flames, with a free stream co-flow velocity of 1.1 m/s.

Flame code	Jet diameter (mm)	Mean jet exit velocity (m/s)	Total density (kg/m³)	Total viscosity (kg/m/s)	Total thermal input (kW)	Natural gas/mix %	H_2/mix %	Strain rate (±2%) u/d (s⁻¹)	Reynolds number $Re = \rho u d/\nu$	Fr_e[a] u^2/gd
NGH_01	4.4	34.69	0.551	9.74E−06	15.44	81.4	18.6	7.75E+03	8.63E+03	2.79E+04
NGH_02	4.4	34.79	0.47	9.93E−06	13.76	67.1	32.9	7.75 E+03	7.24E+03	2.81E+04
NGH_03	4.4	34.28	0.378	1.02E−05	11.64	50.9	49.1	7.75 E+03	5.61E+03	2.73E+04
NGH_04	4.4	33.79	0.289	1.04E−05	9.63	35.1	64.9	7.75 E+03	4.14E+03	2.65E+04
NGH_05	4.4	33.01	0.194	1.04E−05	7.49	18.3	81.7	7.75 E+03	2.71E+03	2.53E+04
NGH_06	4.4	22.76	0.573	9.69E−06	10.44	85.3	14.7	5.26 E+03	5.92E+03	1.20E+04
NGH_07	4.4	22.75	0.482	9.90E−06	9.16	69.2	30.8	5.26 E+03	4.87E+03	1.20E+04
NGH_08	4.4	23.57	0.374	1.02E−05	7.95	50.2	49.8	5.26 E+03	3.81E+03	1.29E+04
NGH_09	4.4	23.34	0.283	1.04E−05	6.58	34.2	65.8	5.26 E+03	2.81E+03	1.26E+04
NGH_10	4.4	23.35	0.188	1.04E−05	5.22	17.4	82.6	5.26 E+03	1.87E+03	1.26E+04

[a] $Fr_e = u^2/gd$ is the exit Froude Number based on cold fuel properties.

Table 3
Details of EH flames, with a free stream co-flow velocity of 1.1 m/s.

Flame code	Jet diameter (mm)	Mean jet exit velocity (m/s)	Total density (kg/m³)	Total viscosity (kg/m/s)	Total thermal input (kW)	C_2H_4/mix %	H_2/mix %	Strain Rate (±2%) u/d (s⁻¹)	Re number $Re = \rho u d/\nu$	Fr_e u^2/gd
EH_01	4.4	33.37	0.805	9.95E−06	21.7	65.7	34.3	7.56E+03	1.19E+04	2.58E+04
EH_02	4.4	32.44	0.614	1.02E−05	16.88	48.1	51.8	7.56E+03	8.59E+03	2.44E+04
EH_03	4.4	34.25	0.45	1.04E−05	13.99	33.1	66.9	7.56E+03	6.53E+03	2.72E+04
EH_04	4.4	33.48	0.28	1.04E−05	9.79	17.4	82.6	7.56E+03	3.97E+03	2.60E+04
EH_05	4.4	32.71	0.09	9.00E−06	5.35	0	100	7.56E+03	1.44E+03	2.48E+04
EH_06	4.4	47.69	0.794	9.97E−06	30.66	64.7	35.3	1.11E+04	1.67E+04	5.27E+04
EH_07	4.4	48.29	0.632	1.02E−05	25.7	49.8	50.2	1.11E+04	1.32E+04	5.41E+04
EH_08	4.4	49.2	0.455	1.04E−05	20.26	33.5	66.5	1.11E+04	9.48E+03	5.61E+04
EH_09	4.4	49.3	0.282	1.04E−05	14.52	17.7	82.3	1.11E+04	5.91E+03	5.64E+04
EH_10	4.4	49.34	0.09	9.00E−06	8.07	0	100	1.11E+04	2.17E+03	5.65E+04
EH_11	4.4	22.1	0.787	9.98E−06	14.1	64.1	35.9	5.17E+03	7.67E+03	1.13E+04
EH_12	4.4	22.77	0.631	1.02E−05	12.11	49.8	50.2	5.17E+03	6.21E+03	1.20E+04
EH_13	4.4	23.25	0.439	1.04E−05	9.33	32.1	67.9	5.17E+03	4.33E+03	1.25E+04
EH_14	4.4	22.99	0.285	1.04E−05	6.81	17.9	82.1	5.17E+03	2.78E+03	1.23E+04
EH_15	4.4	22.91	0.09	9.00E−06	3.75	0	100	5.17E+03	1.01E+03	1.22E+04
EH_16	4.4	15.86	1.178	9.51E−06	15.86	100	0	3.99E+03	9.56E+03	7.14E+03
EH_17	4.4	16.91	0.885	9.85E−06	16.91	73.1	26.9	5.45E+03	9.49E+03	1.34E+04
EH_18	4.4	17.72	0.75	1.00E−05	17.72	60.7	39.3	6.57E+03	9.52E+03	1.94E+04
EH_19	4.4	18.72	0.635	1.02E−05	18.72	50.1	49.9	7.96E+03	9.61E+03	2.85E+04
EH_20	4.4	22.15	0.431	1.04E−05	22.15	31.3	68.7	1.27E+04	1.02E+04	7.28E+04
EH_21	4.4	23.8	0.379	1.04E−05	23.8	26.5	73.5	1.50E+04	1.06E+04	1.01E+05
EH_22	8	13.08	1.178	9.51E−06	39.09	100	0	1.67E+03	1.30E+04	2.18E+03
EH_23	8	13.59	1.022	9.68E−06	35.85	85.6	14.4	1.67E+03	1.15E+04	2.36E+03
EH_24	8	13.56	0.902	9.83E−06	32.09	74.6	25.4	1.67E+03	9.95E+03	2.34E+03
EH_25	8	13.28	0.621	1.02E−05	23.04	48.8	51.2	1.67E+03	6.47E+03	2.25E+03
EH_26	8	13.6	0.367	1.04E−05	15.82	25.4	74.6	1.67E+03	3.83E+03	2.36E+03
EH_27	8	13.44	0.236	1.02E−05	11.67	13.4	86.6	1.67E+03	2.47E+03	2.30E+03
EH_28	8	13.24	0.09	9.00E−06	7.16	0	100	1.67E+03	1.06E+03	2.23E+03

Table 4
Details of ENH flames, with an exit fuel density of 0.725 kg/m³, an exit fuel viscosity of 1.20×10^{-5} kg/m/s, and a free stream co-flow velocity of 1.1 m/s.

Flame code	Jet Diameter (mm)	Mean jet exit velocity (m/s)	Total thermal input (kW)	C_2H_4/mix (±2%) %	H_2/mix (±2%) %	Strain Rate (±2%) u/d(s⁻¹)	Re number (±2%) $Re = \rho u d/\nu$	Fr_e u^2/gd	Flame length L_f (mm)	ξ_L
ENH_1	4.4	56.73	23.88	40	41	1.29E+04	1.52E+04	7.46E+04	667	2.24
ENH_2	5.8	42.4	31.49	40	41	7.50E+03	1.52E+04	3.16E+04	825	2.8
ENH_3	8	31.48	43.87	40	41	3.93E+03	1.52E+04	1.26E+04	1050	3.52
ENH_4	4.4	45.15	19.13	40	41	1.03E+04	1.19E+04	4.73E+04	636	2.49
ENH_5	5.8	33.41	24.57	40	41	5.76E+03	1.19E+04	1.96E+04	785	3.12
ENH_6	8	23.84	34.35	40	41	2.98E+03	1.19E+04	7.25E+03	957	3.84
ENH_7	4.4	33.69	14.37	40	41	7.50E+03	8.86E+03	2.63E+04	612	2.91
ENH_8	5.8	25.35	18.66	40	41	4.37E+03	8.86E+03	1.13E+04	760	3.63
ENH_9	8	17.91	25.05	40	41	2.24E+03	8.86E+03	4.09E+03	850	4.13

*$\xi_L = g^{1/3}L_f/((\rho_0/\rho_\infty)^{1/3}u^{2/3}d^{2/3})$ is the non-dimensional flame length, used to assess the effect of buoyancy for a flame with visible length L_f [20].

Table 5
Composition of natural gas from the supplier.

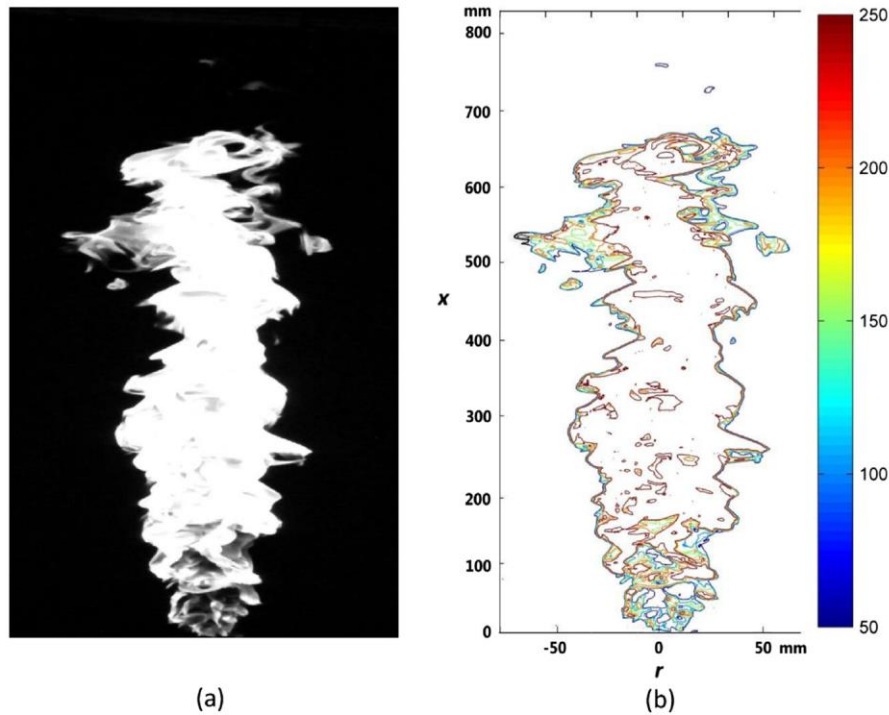| Composition	C_3H_8	$i\text{-}C_4H_{10}$	$n\text{-}C_4H_{10}$	N_2	CO_2	Ethane	CH_4
Percent by volume %	0.2099	0.0278	0.0399	1.1830	0.5447	1.1048	96.89

Fig. 3. Instantaneous image of Flame *EH_01* (a), and its corresponding pixel intensity contour (b).

showing a clear dependence on strain rate, but no apparent dependence on Re at constant strain rate with the error bars accounted for.

3.3. Influence of hydrogen addition on radiant fraction

Figure 6 presents the dependence of χ_r on the volume fraction of hydrogen for the blended ethylene and natural gas flames. Also presented are the previous measurements by Turns and Myhr [5] who employed similar fuels, but with the hydrogen introduced into an annular pilot instead of as a blend. Interestingly, the present flames exhibit a consistent trend with those of Turns and Myhr, in which χ_r is found to decrease with the addition of hydrogen. In addition, the slopes in the two data sets are also similar. However, there is a significant offset in the values of the two measurements even with the same flow rate of pure ethylene, with the measured values of χ_r being higher for Turns and Myhr's data than for the present data. This cannot be attributed either to the influence of u/d or to Re, since the total flow rates of fuel and jet diameters for the two experiments are quite similar. Rather, the dominant cause for these differences is expected to be the role of the pilot, which will inhibit the entrainment of air into the fuel jet near to the base of the flame. In addition, a further possible contributing factor to these differences is that the radiant fraction measurements by Turns' were undertaken with the heat flux measured at a single point at half of the flame length [5], while the present data employs a full axial profile of radiant heat flux. Hence, overall, the present data are considered to be consistent with these previous measurements.

It can also be seen from Fig. 6 that an increase in u/d results in a decrease in χ_r as expected. The increase in strain rate is known to decrease soot volume fraction, both for laminar flames [26] and turbulent flames [8]. For *EH* blended fuels, this dependence of χ_r on hydrogen volume fraction (x_v) exhibits two distinct regimes.

For blends in which x_v is less than about 30%, the flames are ethylene dominated and the radiation fraction decreases only weakly with an increase in x_v. However, in the hydrogen dominated regime, i.e. $x_v > 70\%$, χ_r decreases strongly with a further increase in x_v.

An inverse correlation between χ_r and x_v is also found in the *NGH flames*, although the absolute values of χ_r are much lower than those of the *EH flames*. Unlike the *EH flames*, these *NGH flames* do not exhibit two distinct regimes, most probably because of the lower sooting propensity of natural gas relative to ethylene. Since sooting propensity depends not only on fuel type, but also on the scale of a flame and on the mixing characteristics of a burner [27], care should be taken in seeking to extrapolate these data to other conditions, although the presence of two regimes may well apply to flames with relatively high sooting propensity.

3.4. Influence of hydrogen addition on flame length

Results from the current study demonstrate that the normalized flame length decreases with an increase in the H_2/mix ratio at constant strain rate, which is consistent with previous studies [1,6]. It also increases with increasing the Re as was found by Turns and Myhr [5]. It can be seen from Fig. 7 that the normalized flame length is comparable to Turns and Myhr's results where the input of fuel is similar. However, in contrast to their trend, the normalized flame length of the current *EH flames* decreases with increasing x_v. This is because flame length is determined mainly by the air–fuel ratio. While less air is required to burn the same volume of fuel with the addition of hydrogen in the present flames, more air is required for Turns and Myhr's [5] flames with the addition of hydrogen, because their H_2 was increased at constant hydrocarbon flow rate. That is, increasing the flow-rate to the hydrogen pilot for Turns and Myhr's flames [5] increases the flow of combustion products

Fig. 5. Radiant fraction as a function of strain rate at different Re for the present *ENH* flames.
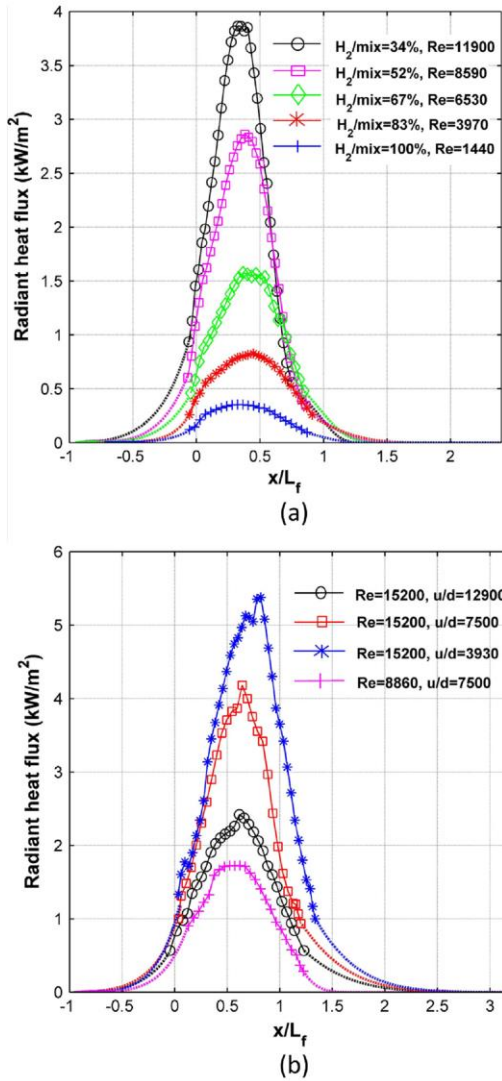

Fig. 4. Radiant heat flux distribution along the normalized flame length of ethylene–hydrogen blended flames *EH_01-EH_05* (a), and four different conditions with a fixed blend of ethylene, nitrogen and hydrogen for flames *ENH_1–3 and ENH_7* (b). *x* is the axial distance above burner. Radiant heat flux was measured at a radial distance of 280 mm. Symbols are experimental data, dashed lines are extrapolated profiles in the axial direction following the trend reported by Gore and Faeth [25]. This assumes an exponential function at both ends of the profile with the heat flux approaching 0 at x/d = 365 and −136 respectively.

Fig. 6. Radiant fraction as a function of molar ratio of hydrogen in the blended fuel for the present non-piloted *EH* and *NGH* flames in a co-flow. Also plotted is the ethylene and methane flames with hydrogen pilot of Turns and Myhr [5].

around the hydrocarbon flame, which can be expected to inhibit the entrainment of oxygen into the hydrocarbon flame, increasing the flame length.

3.5. Influence of hydrogen addition on global residence time

The global residence time (τ_G) of a flame is calculated using Eq. (3), following Turns and Myhr [5].

$$\tau_G = \frac{\rho_f W_f^2 L_f f_s}{3\rho_o d^2 u} \tag{3}$$

Here ρ_f, W_f and L_f are the flame density, width and length, f_s is the mass fraction of the fuel; ρ_0 is the density of the fuel, d and u are jet diameter and jet exit velocity of fuel, respectively.

101

Figure 8 presents the dependence of τ_G on x_v for the series of data-sets. It can be seen that this dependence is relatively weak, although some trends are evident. For the case where x_v is increased at constant exit strain rate, a small increase in hydrogen volume fraction results in little change in τ_G, although a further increase results in a shorter flame and a decrease in τ_G. However, there is a slight reverse in the trend where x_v approaches 100% for flames with relatively high strain rate. This is because the decrease of fuel density exceeds the decrease of flame volume in this regime. In addition, for the *EH flames*, a higher jet exit strain rate leads to a shorter residence time, which indicates that higher flow velocity of the fuel increases the mixing rate.

The global residence time for current *NGH flames* corresponds well with Turns and Myhr's measurement. However, the present *EH flames* have a significantly lower residence time than those of Turns and Myhr's [5]. This is attributable to the same reason described above for their higher radiant fraction.

3.6. Pollutant emissions

Emission indices for NO_x was calculated using Eq. (4) .

$$EI_{NOx} = \frac{x_{NOx}}{(x_{CO} + x_{CO_2} - x_{CO_{2amb}})} \times \left(\frac{n_C \times MW_{NOx}}{MW_f \times HHV_f} \right) \qquad (4)$$

where x_{NOx} is the mole fraction of NO_x, x_{CO}, x_{CO_2} are the measured mole fraction of CO and CO_2; $x_{CO_{2amb}}$ is the CO_2 concentration in ambient air; n_c is the number of carbon atoms per mole of fuel, MW_{NOx} is molecular weight of NO_x; MW_f and HHV_f are the molecular weight and higher heating value of the fuel (MJ/kg), respectively. Note that emission indices for $x_v = 100\%$ were not calculated because Eq. (4) does not apply to non-carbon fuels. EI_{NOx} (g/MJ fuel) is plotted in Fig. 9 as a function of hydrogen volume fraction.

Consistant with the NO_x emissions reported by Turns and Myhr [5], Fig. 9 shows that the NO_x emissions tend to increase with the hydrogen volume fraction except for where $x_v < 30\%$. This is consistent with the hydrogen addition causing the higher heating Value for fuels. In addition, the overall trend of NO_x emission is counter to the trend for the radiant fraction and hydrogen/mix ratio. That is, the addition of hydrogen increases the temperature of the flame for both fuels, although for slightly different reasons. For the case of ethylene, whose adiabatic flame temperature is only 11 K lower than for hydrogen, the biggest influence is the decrease in the radiant fraction. For the case of natural gas, whose adiabatic flame temperature is 155 K less than H_2, this effect is more significant than the influence on radiant fraction, since natural gas has a lower sooting propensity than C_2H_4. Furthermore, the addition of hydrogen also increases the concentration of the radical pool (H, OH, O) as discussed by Choudhuri et al. [11], which together enhances the NO formation through the thermal route. In contrast, an increase in the hydrogen fraction decreases the formation of CH, which decreases the NO destruction through the Fenimore mechanism [11]. The net effect of these influences is that the NO emission increases as hydrogen concentration increases in the fuel mixture [3].

Figure 10 presents the NO_x production rate, as calculated by normalizing the NO_x emission index with τ_G, as a function of inverse temperature following the method used by Turns and Myhr. The non-adiabatic temperature for a stoichiometric mixture was calculated by incorporating radiant fraction into the NASA chemical equilibrium code. Consistent both with the results of Turns and Myhr [5] and Newbold et al. [28], the NO_x emission rate is seen to decrease with the reciprocal of non-adiabatic flame temperature, which is expected, because most of the NO_x is formed by the thermal mechanism. The present data from all the flame conditions exhibit a comparable level of agreement with the $1/T$
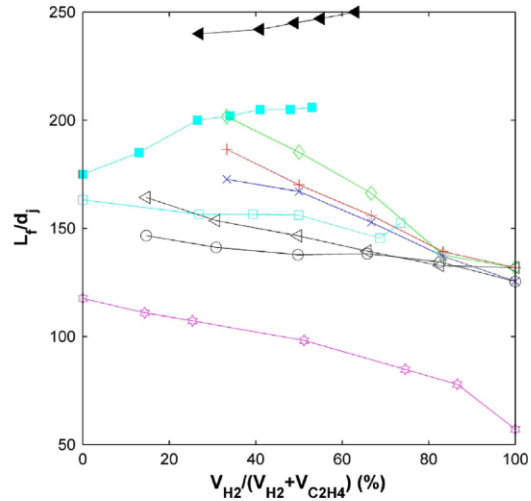

Fig. 7. Normalized flame length L_f/d_j of *EH* and *NGH* flames compared with Turns and Myhr's measurement [5]. Refer to Fig. 6 for legend.

scaling for thermal NO_x production derived by Turns and Myhr [5]. This provides strong evidence for the dominance of the thermal NO_x emission mechanism for these blended fuels.

Figure 10 also shows that the *ENH flames* exhibit a Re dependence. While flames with Re = 8500 and 11,525 show a similar relationship between NO_x emission rate and the reciprocal of flame temperature, that for Re = 15,000 exhibits a slightly higher NO_x emission rate than the $1/T$ scaling. These additional dependencies, together with the significant departures from the $1/T$ scaling, are to be expected given the well-known complexity of NO_x generation mechanisms.

The ratio of CO/CO_2 is plotted as a measure of incomplete combustion in Fig. 11. It can be seen that the CO/CO_2 ratio is very sensitive to the strain rate, with *EH flames* of lower strain rate
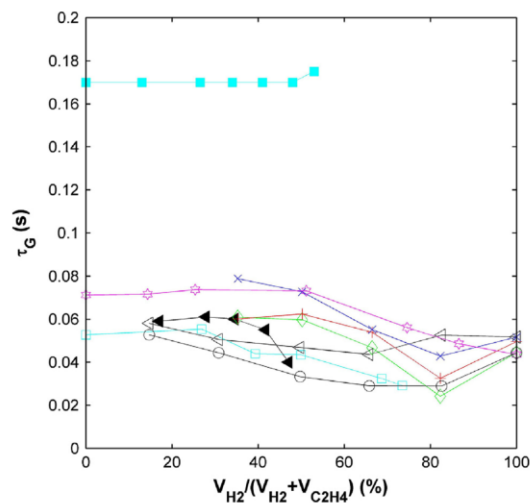

Fig. 8. Global residence time τ_G as a function of hydrogen volume fraction in blended fuels, compared with Turns and Myhr's [5] results. Refer to Fig. 6 for legend.
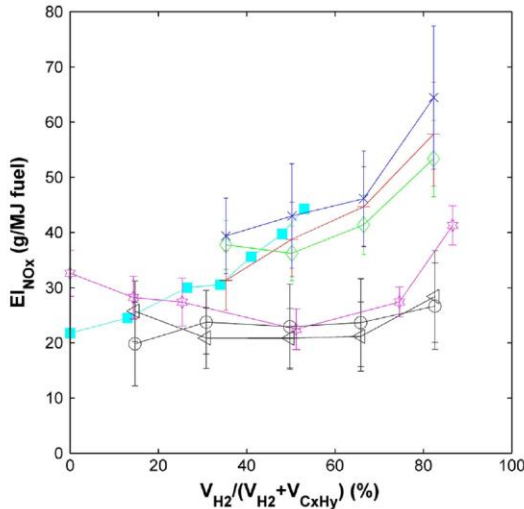
Fig. 9. NO_x emission index, EI_{NOx} (g/MJ fuel), as a function of hydrogen volume fraction in the current *EH* and *NGH flames*, together with previous measurements of Turns and Myhr's [5] E/H flames. Refer to Fig. 6 for legend.

Fig. 11. CO/CO_2 ratio as a function of hydrogen volume fraction in blended fuels.

exhibiting a completely different trend from those with a higher strain rate. The value of CO/CO_2 is approximately independent of x_v for the low strain rate case, while it increases with x_v for the high strain rate case. This implies that the lower strain rate allows

sufficient residence time for CO to be oxidized, while for the higher strain cases, an increase in x_v cause a decrease in τ_G. A decrease in τ_G is known to inhibit the completion of CO oxidation process [29]. Similarly, the apparent discrepancy in the dependence of CO/CO_2 ratio on strain for the *NGH flames*, in which a lower strain rate results in higher CO/CO_2 ratio, can be explained by the same phenomenon. It can be seen in Fig. 8 that the *NGH flames* with a lower strain rate exhibits a shorter global residence time.

Figure 12 shows that the CO/CO_2 ratio for *ENH flames* of constant Re decreases with an increase in the exit strain rate. This is because increasing strain rate at constant Re results in a decrease in the input rate of fuel, and hence a reduced carbon input, which significantly decreases the CO/CO_2 ratio even though global residence is shorter for *ENH flames* with higher strain rate. Besides, for the same fuel composition, the CO/CO_2 ratio decreases with an increase in Re. This is because, as was discussed before, despite the higher carbon input rate for larger Re, the longer global residence
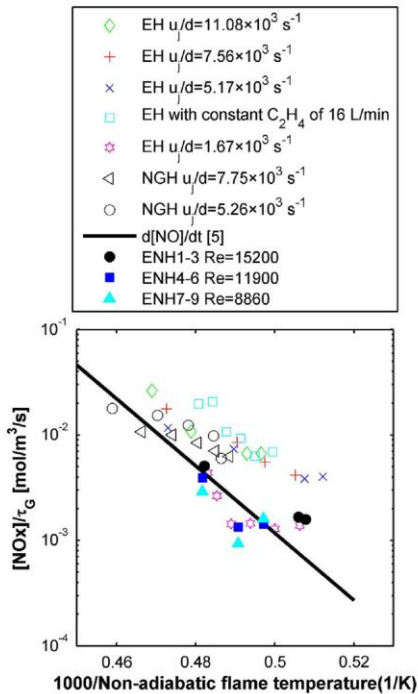

Fig. 10. The NO_x production rate (mole/m³ fuel/s) as a function of the inverse non-adiabatic flame temperature for the *EH*, *NGH* and *ENH flames*, following the time temperature scaling of Turns and Myhr [5]. The solid line represents the theoretical NO production rate for the thermal mechanism.
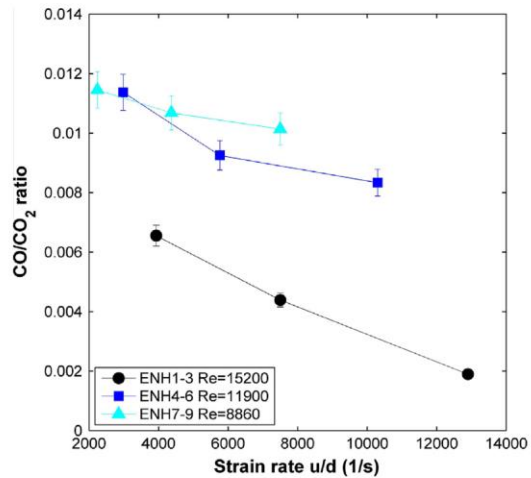

Fig. 12. CO/CO_2 ratio as a function of strain rate for *ENH flames*.

time and higher mixing rate of more turbulent flames enhances the CO oxidation, which results in a lower CO/CO_2 ratio.

4. Conclusions

This paper has assessed the influence of the blend ratio of hydrogen–hydrocarbon fuels on the global performance of non-premixed jet flames and has reported their exit velocity profiles for non-reacting flows to make them well-defined. The key findings from this work are as follows:

1. The radiant fraction decreases with the addition of hydrogen as expected, due to a reduction in the presence of soot. This implies that hydrogen blending is likely to be deleterious to heat transfer in those applications dominated by radiant heat transfer. For the same fuel composition, increasing the strain rate at constant Reynolds number decreases the radiant fraction, while variation in the Reynolds number at constant strain rate does not have a significant influence on radiant fraction.
2. The heat flux distribution is sensitive to the hydrogen fraction, with a complex and non-monotonic dependence of the position of the peak with respect to normalized flame length at constant volume flow rate of fuel (and hence constant exit strain rate). The peak in the normalized profile translates downstream with an initial increase in hydrogen fraction, but then translates upstream again for pure hydrogen. This is attributable to the combined influences of an increase in hydrogen fraction acting both to inhibit soot formation and to shorten the flame.
3. The NO_x emissions from a flame tends to increase with the hydrogen fraction in the fuel, pointing to the need for additional NO_x control measures when hydrogen is added to the fuel. This increase is attributed to the combined influences of an increase in flame temperature due to the higher adiabatic flame temperature, lower radiant fraction and to the reduction in the CH radial pool. The NO_x production rate scales reasonably well with the reciprocal of non-adiabatic flame temperature, suggesting that the NO_x emissions are dominated by the thermal NO_x route. For an increase in strain rate at constant fuel composition, the NO_x is controlled by the competing influences of radiant fraction and global residence time. Hence thermal NO_x control strategies are likely to be most effective.
4. The CO/CO_2 ratio is determined by the competing impacts of flame residence time and carbon input rate and mixing rate of flames. It is independent of hydrogen ratio at low strain rats, but increases with hydrogen addition at higher strain rates.

References

[1] A.R. Choudhuri, S. Gollahalli, Int. J. Hydrogen Energy 25 (5) (2000) 451–462.
[2] A. Katoh, H. Oyama, K. Kitagawa, A.K. Gupta, Combust. Sci. Technol. 178 (12) (2006) 2061–2074.
[3] A.R. Choudhuri, S. Gollahalli, Int. J. Hydrogen Energy 28 (4) (2003) 445–454.
[4] Y. Wu, Y. Lu, I. Al-Rahbi, G. Kalghatgi, Int. J. Hydrogen Energy 34 (14) (2009) 5940–5945.
[5] S.R. Turns, F.H. Myhr, Combust. Flame 87 (3) (1991) 319–335.
[6] S. El-Ghafour, A. El-dein, A. Aref, Int. J. Hydrogen Energy 35 (6) (2010) 2556–2565.
[7] J. Kent, S. Bastin, Combust. Flame 56 (1) (1984) 29–42.
[8] N. Qamar, G.J. Nathan, Z.T. Alwahabi, K.D. King, Proc. Combust. Inst. 30 (1) (2005) 1493–1500.
[9] G. Nathan, P.A.M. Kalt, Z.T. Alwahabi, B.B. Dally, P.R. Medwell, Q.N. Chan, Prog. Energy Combust. Sci. 38 (1) (2012) 41–61.
[10] S. Mahmoud, Nathan, G.J., Medwell, P.R., Dally, B.B., Alwahabi, Z.T., Proceedings of the Combustion Institute, vol. 35, accepted. (2015).
[11] A.R. Choudhuri, S.R. Gollahalli, Int. J. Hydrogen Energy 25 (11) (2000) 1119–1127.
[12] A.R. Choudhuri, S. Gollahalli, Int. J. Hydrogen Energy 29 (12) (2004) 1293–1302.
[13] P. Kumar, D. Mishra, Int. J. Hydrogen Energy 33 (1) (2008) 225–231.
[14] H. Zhen, C. Cheung, C. Leung, Y. Choy, Int. J. Hydrogen Energy 37 (14) (2012) 10947–10955.
[15] T. Shudo, K. Omori, O. Hiyama, Int. J. Hydrogen Energy 33 (17) (2008) 4689–4693.
[16] N. Kahraman, B. Ceper, S.O. Akansu, K. Aydin, Int. J. Hydrogen Energy 34 (2) (2009) 1026–1034.
[17] J. Mi, D.S. Nobes, G.J. Nathan, J. Fluid Mech. 432 (2001) 91–125.
[18] H. Yamaguchi, Engineering fluid mechanics, Springer, Dordrecht, Netherlands, 2008, p.^pp.
[19] International Sooting Flame (ISF) Workshop. http://www.adelaide.edu.au/cet/isfworkshop/data-sets/turbulent/.
[20] H. Becker, S. Yamazaki, Combust. Flame 33 (1978) 123–149.
[21] M. Corporation, In: 64 series Heat Flux Transducers, Huntsville, Alabama, 1995.
[22] A. Langman, G.J. Nathan, J. Mi, P.J. Ashman, Proc. Combust. Inst. 31 (1) (2007) 1599–1607.
[23] M. Mungal, P. Karasso, A. Lozano, Combust. Sci. Technol. 76 (4–6) (1991) 165–185.
[24] G. Newbold, G. Nathan, R. Luxton, Combust. Sci. Technol. 126 (1–6) (1997) 71–95.
[25] J. Gore, G. Faeth, In: Structure and spectral radiation properties of turbulent ethylene/air diffusion flames, Symposium (International) on Combustion, Elsevier 1988 (1988) 1521–1531.
[26] M.E. Decroix, W.L. Roberts, Combust. Sci. Technol. 160 (1) (2000) 165–189.
[27] G. Nathan, J. Mi, Z.T. Alwahabi, G. Newbold, D.S. Nobes, Prog. Energy Combust. Sci. 32 (5) (2006) 496–538.
[28] G. Newbold, G.J. Nathan, D.S. Nobes, S. Turns, Proc. Combust. Inst. 28 (1) (2000) 481–487.
[29] R. Yetter, F. Dryer, H. Rabitz, Combust. Sci. Technol. 79 (1–3) (1991) 97–128.

CHAPTER 7

SECONDARY CONCENTRATORS TO ACHIEVE HIGH FLUX RADIATION WITH METHAL HALIDE SOLAR SIMULATORS

Xue Dong[1], Graham J. Nathan[2], Zhiwei Sun[2], Peter J. Ashman[1], Dahe Gu[2]

[1]Centre for Energy Technology, Schools of Chemical Engineering & [2]Mechanical Engineering, The University of Adelaide, Adelaide, SA 5005, Australia

Statement of authorship

Title of Paper	Secondary concentrators to achieve high flux radiation with methal halide solar simulators
Publication Status	☐ Published ☐ Accepted for Publication ☑ Submitted for Publication ☐ Publication Style
Publication Details	Journal of Solar Energy Engineering

Principal Author

Name of Principal Author (Candidate)	Xue Dong		
Contribution to the Paper	Under the supervision of P. J. Ashman and G. J. Nathan and Z. W. Sun, I developed the experimental and modelling methods, performed the experiments and simulation, processed the data and wrote the manuscript.		
Overall percentage (%)	55%		
Signature		Date	09/09/2015

Co-Author Contributions

By signing the Statement of Authorship, each author certifies that:

xiii.   the candidate's stated contribution to the publication is accurate (as detailed above);

xiv.   permission is granted for the candidate in include the publication in the thesis; and

xv.   the sum of all co-author contributions is equal to 100% less the candidate's stated contribution.

Name of Co-Author	Peter J. Ashman		
Contribution to the Paper	I acted as primary supervisor for the candidate, aided in evaluating the modelling approach and revising the manuscript. I give consent for Xue Dong to present this paper for examination towards the Doctorate of Philosophy.		
Signature		Date	9/9/15

Name of Co-Author	Graham J. Nathan		
Contribution to the Paper	I acted as secondary supervisor for the candidate, aided in developing of the experimental method, evaluating the modelling approach and revising the manuscript. I give consent for Xue Dong to present this paper for examination towards the Doctorate of Philosophy		
Signature		Date	10/9/15

Name of Co-Author	Zhiwei Sun
Contribution to the Paper	I am a post-doc who aided in evaluating the modelling approach and revising the manuscript. I give consent for Xue Dong to present this paper for examination towards the Doctorate of Philosophy.
Signature	Date 01/09/2015

Name of Co-Author	Dahe Gu
Contribution to the Paper	I am a fellow PhD student, aided in performing the experiments and evaluated the final version of the manuscript. I give consent for Xue Dong to present this paper for examination towards the Doctorate of Philosophy.
Signature	Date 11/9/2015

CHAPTER 8

CONCLUSIONS

8.1 Conclusions

The thesis advances the knowledge of the influence of concentrated solar radiation on sooty flames. Its first major contribution is establishing an experimentally validated ray-tracing model that accurately predicts the concentrated heat flux from the solar simulator, and using this model, new design and optimization of solar simulators were performed. While this ray-tracing model is developed for metal halide lamps, the methodology is applicable more generally to solar simulators employing other types of discharge arc lamps. The second major contribution is that the time-resolved spectra of solar simulators employing metal halide and xenon arc lamps were measured using the same spectrometer for the first time to allow for direct comparison, which provides significant information to applications in reactors with short residence time. The third major contribution is that the first measurement of the influence of concentrated solar radiation on the soot volume fraction and temperature of a flame was performed, which pushed forward the existing understanding of the interaction between broadband solar radiation and a sooty flame. The following sections outline the specific conclusions drawn from the various parts of this study.

8.1.1 Concentric multilayer model of the arc in high intensity discharge lamps for solar simulators with experimental validation

A single-cylinder model of the arc from the metal halide lamps, whose arc length is 23 mm, is too simplistic to provide reliable calculations of heat flux from a solar simulator. That is, even with the best case, which corresponds to an assumed arc diameter of 11mm diameter, the predicted peak flux is 4.5% lower and the half-with is 52 % greater than the measured values. Hence a more complex model is required for accurate prediction of the heat flux from these lamps. The simulated heat flux at the focal plane is sensitive to the length and diameter of the arc in a single layer arc model, so that a smaller diameter and shorter length of the cylindrical arc results in a higher peak flux, shorter half-width and higher total flux at the target with a small aperture. While the calculations obtained by assuming the arc as an uniformly radiant volume source yield better agreement than the single layer model, the calculated flux falls outside the error bars toward the outer half of the focal zone. In addition, the calculated flux is sensitive to the assumed diameter of the cylindrical volume, for which there is no absolute definition. The limitations of this model can be explained by comparison of the measured and predicted line of sight radiation from the arc, which show that the real arc does not exhibit uniform flux density.

A model employing concentric multi-layered cylinders or spheres gives somewhat improved accuracy but nevertheless fails to provide good agreement with the measured heat flux. This is because the cyclical nature or the arc results in a shape that differs significantly from either a cylinder or a sphere during certain phases of the cycle.

Simulations obtained with a compound model of cylinders and monopole

spheres and dipole spheres were found to give the best agreement with the measured data of the models evaluated here. The best cases falls within the error bar of the experiment for peak flux, and the departure of the half-width from the measured value is within 11%. The difference in heat flux between the measurement and simulation is less than 13% within an area of 92 mm diameter. In addition, when the concentric layers are spaced sufficiently closely to resolve the profile of the arc, which here corresponds to 9 layers, the simulated results become insensitive to the way in which the arc source is stratified. The radiation source beyond a diameter of 13 mm does not make significant contribution to the maximum heat flux.

The measured lamp-to-lamp variation in the mean radiant intensity was found to be 7.2% for the metal halide lamp HMI6000 assessed in our laboratory. However, these details will depend upon the quality of the power supply. In addition, the radiation distribution of the arc is somewhat lamp-specific, so that the present measurements cannot be expected to necessarily translate exactly to other models or types of lamp. That is, in-situ measurements of the arc for different lamps will lead to the most accurate predictions, although the proposed modelling approach is likely to be applicable.

8.1.2 Time-resolved spectra of solar simulators employing metal halide and xenon arc lamps

It was found that the integrated deviation of the time-averaged spectrum of metal halide lamp matches that of the solar spectrum 3.4 times better than does the xenon arc lamp, mainly due to the strong radiation peaks in the 800-900 nm range from xenon arc lamp. The deviation of the spectrum from metal halide lamp (I_{lamp}-I_{sun})/I_{sun} is less than a factor of 2 for all wavelengths; while that of xenon arc lamp is up to a factor of 7 in the 800-900 nm range. This trend is consistent with

previous understanding from manufacturer's data, although the present relative comparison is expected to be more accurate since it was performed with identical equipment. Some differences between the present measurements and those of the manufacturers were found, as is expected, due to slight differences in power supply, manufacturing details and the measuring technique. However, such differences are second order compared with differences in the lamp type.

The time-resolved measurements of the radiation intensity of solar simulators has revealed that the radiant intensity from metal halide lamp oscillates at a frequency of 100 Hz, which is twice the frequency of the AC power supply, while that of xenon arc lamp is around 300 Hz. In addition, the amplitude of the oscillation of the radiation intensity from the metal halide lamp is about 60% of its peak value, while that from the xenon arc lamp is around 9%. The difference in the amplitude of fluctuations in radiation intensity is due to the difference in the type of power supply. Hence too, while the xenon arc lamp offers a steadier radiant output than the metal halide lamp, neither lamp achieves a truly steady-state output.

The spectrum from the xenon arc lamp is more stable than that for the metal halide lamp due to its use of a DC power supply. The fluctuation in intensity of the broadband radiation from the xenon arc lamp is only approximately 9% relative to its peak value. However, the spectrum from the metal halide lamp shows that the intensity of spectral irradiance gradually increases from 0 to π, and then reverses over the phase range from π to 2π. Overall, light in the range 400 - 700 nm dominates the broadband radiation from the solar simulator with the metal halide lamp.

The application of concentrators can have a significant influence on the spectrum of the radiation from the lamp in selected bands, with reductions in

certain wavelength by up to 10% for the elliptical reflector only and to 20% for that with both the elliptical and conical concentrators. Hence care must be taken in assuming the lamp spectrum is the same as that from the concentrator.

8.1.3 The influence of high flux radiation from a concentrated solar simulator on a sooty flame: assessed via soot concentration and flame temperature measurements

The fv is higher in the flame with CSR by 40% - 50 % at downstream location (HAB > 30 mm), especially in the fuel rich side, although there is no visible change to the length and width of the flame. The overall soot volume in the flame is increased by 55% by the simulated CSR. In addition, the soot inception was translated further upstream by 6.2% of the flame length with radiation. The consumption rate of soot in the axial direction is almost the same for the case with the simulated CSR and that without. While the consumption rate of soot in the radial direction is higher for the case with the simulated CSR, by an average value of 7% from HAB = 20 mm downstream.

Possible mechanisms are: Soot absorption tends to dominate the interactions between CSR and a flame. Furthermore, an increase in f_v caused by the absorbed irradiation will further increase f_v and thus lead to further absorption of CSR. Meanwhile, PAH and other molecular species also absorbs CSR, which are expected to be the causes of the upstream translation of the point of soot inception. With the increase of soot concentration, the flame temperature is determined by two competing mechanisms: i.e. increased soot absorption of CSR and increased radiant loss from soot. The increased rate of soot consumption is expected to be attributed to the increased flame temperature.

8.1.4 Global characteristics of non-premixed jet flames of hydrogen-hydrocarbon blended fuels

The key findings from this work are as follows:

The radiant fraction decreases with the addition of hydrogen as expected, due to a reduction in the presence of soot. This implies that hydrogen blending is likely to be deleterious to heat transfer in those applications dominated by radiant heat transfer. For the same fuel composition, increasing the strain rate at constant Reynolds number decreases the radiant fraction, while variation in the Reynolds number at constant strain rate does not have a significant influence on radiant fraction.

The heat flux distribution is sensitive to the hydrogen fraction, with a complex and non-monotonic dependence of the position of the peak with respect to normalized flame length at constant volume flow rate of fuel (and hence constant exit strain rate). The peak in the normalized profile translates downstream with an initial increase in hydrogen fraction, but then translates upstream again for pure hydrogen. This is attributable to the combined influences of an increase in hydrogen fraction acting both to inhibit soot formation and to shorten the flame.

The NO_x emissions from a flame tends to increase with the hydrogen fraction in the fuel, pointing to the need for additional NOx control measures when hydrogen is added to the fuel. This increase is attributed to the combined influences of an increase in flame temperature due to the higher adiabatic flame temperature, lower radiant fraction and to the reduction in the CH radial pool. The NO_x production rate scales reasonably well with the reciprocal of non-adiabatic flame temperature, suggesting that the NO_x emissions are dominated by the thermal NO_x route. For an increase in strain rate at constant fuel composition, the NO_x is controlled by the competing influences of radiant fraction and global

residence time. Hence thermal NOx control strategies are likely to be most effective.

The CO/CO$_2$ ratio is determined by the competing impacts of flame residence time and carbon input rate and mixing rate of flames. It is independent of hydrogen ratio at low strain rats, but increases with hydrogen addition at higher strain rates.

8.1.5 Secondary concentrators to achieve high flux radiation from metal halide solar simulators

The use of a large, conical secondary concentrator near to the focal plane can increase the concentration ratio significantly, although this occurs at the expense of a reduction in the transfer efficiency of the system. For example, the addition of the secondary concentrator to the single metal halide lamp system can increase the peak flux by 294% and increase the average flux by up to 93 % within a target of 100 mm diameter, with a corresponding reduction in power by 15%. Similarly, the conical secondary concentrator for a seven-lamp system can increase the peak flux by 87.3% and increase the average flux by up to 100% within the same area, with a corresponding reduction in total power by 48%. The increase can be higher with a smaller outlet diameter d, but this occurs at the cost of decreased radiant energy in the target area. The optimized half angle of secondary concentrator for the single lamp system is 10°-11°. The performance of the secondary concentrator for a seven-lamp system optimized at a length of 600 mm and a half angle of 24.5°. The optimized half angle of the secondary concentrator is closely related with the angle defined by the outmost rim of the elliptical reflector to the focal point. The concentration of the primary reflector is sufficiently good that further increases in reflector length over the 600 mm results in negligible additional benefit.

The use of a tertiary back reflector further increases concentration and reduces the

trade-off in transfer efficiency. For example, with the aforementioned seven-lamp system with the secondary concentrator, the use of a tertiary concentrator results in a further increase of 24.9% for peak flux and 21.7% for average flux within a target of 100 mm, resulting an average flux of 0.7 MW/m^2 within the volume of $100 \times 100 \times 100$ mm^3.

The concentrated heat flux is sensitive to the surface reflectance of the conical secondary concentrator, with both the peak and the average fluxes decrease linearly/quadratically with the surface reflectance. Heat flux concentrated by the tertiary back reflector is of lower sensitivity to reflectance compared with that for the secondary concentrator, due to the lower contribution of the conical back reflector to the concentrated flux.

The presence of the secondary concentrator reduces the sensitivity of the heat flux at the focal plane to misalignment between the elliptical reflector and the arc. However, this reduction is more significant for the single lamp system than for the seven lamp system. These results highlight the significance of the accuracy of the alignment during the operation of the solar simulators.

8.2 Recommendations for future work

This thesis advances the knowledge of the influence of concentrated solar radiation on combustion. However, more studies are required to further understand the mechanisms involved in the interaction between high flux solar radiation and sooty flames. These are presented here:

1. Measurement of heat flux from multiple-lamp system. This is because, although the geometry of the concentrators has been optimized and the resultant heat flux from multiple-lamp systems has been predicted using a Monte-Carlo ray-tracing model, the experimental results are always desirable for testing the validity of the ray-tracing simulation for multiple lamps system, and to further improve the model.

2. Isolating the spectral effect of concentrated solar radiation on combustion by introducing high flux laser radiation of different wavelengths into the flame. This will help to better understand the mechanism of the interaction between species in the flame and radiation of difference wavebands. This is because, it is expected that although the absorption of soot is broadband, that of other species is more wavelength selective. However, based on the current measurement employing the high-flux broadband radiation, the spectral effect of the high-flux radiation on a sooty flame cannot be isolated.

3. The measurement of more species/parameters in the flame with and without CSR would be desirable. For example, the distribution of OH will help to identify the change (if any) of the flame oxidation layers; and/or the measurement of the soot sizing, e.g. through time-resolved LII, will be important information to identify whether CSR will crush soot into smaller particles.

4. Assessing the effect of the intensity of concentrated solar radiation on combustion by varying the intensity of the incident radiation on flames, to investigate whether the influence of CSR on flame is progressive or there is a threshold for the impact to take place.

5. Measurement of radiant fraction of the flame with and without the CSR to quantify the difference of radiation from the flame. This will be significantly useful to relate this research finding to industrial applications, because radiation is the major form of heat transfer in furnaces and kilns.

6. The current work would also be more industrial related if the fuels were expanded from ethylene to methane or such solid fuels as coal or biomass. This investigation may need to be undertaken alongside with the development of advanced diagnostic techniques for combustion of solid fuels.

7. Modelling the flame under external radiation can help to identify the key species responsible for the interaction between solar radiation and flames, and the relative significance of their contributions. Modelling the hydrogen-hydrocarbon blended fuels will also be useful to isolate the effect of soot volume fraction and temperature on the radiant fraction and pollutant emissions of these flames.

APPENDIX A

A HIGH-FLUX SOLAR SIMULATOR SYSTEM FOR INVESTIGATING THE INFLUENCE OF CONCENTRATED SOLAR RADIATION ON TURBULENT REACTING FLOWS

Xue Dong[1], Peter J. Ashman[1], Graham J. Nathan[2]

Schools of Chemical Engineering[1] & Mechanical Engineering[2],
Centre for Energy Technology
The University of Adelaide, Adelaide, South Australia, SA5000, Australia

Dong, X., Ashman, P.J. and Nathan, G.J. (2012) A high-flux solar simulator system for investigating the influence of concentrated solar radiation on turbulent reacting flows. In Proceedings of the 50th Annual Conference of the Australian Solar Energy Society held in Melbourne, December 2012, pp.1-14.

APPENDIX B

INFLUENCE OF SIMULATED SOLAR RADIATION ON THE SOOT VOLUME FRACTION IN LAMINAR SOOTY FLAMES

Xue Dong[1, 2, *], Graham J. Nathan[1, 3], Zhiwei Sun[1, 3], Dahe Gu[1,3], Peter J. Ashman[1, 2], Zeyad Alwahabi[1,2], Bassam Dally[1,3]

[1]Centre for Energy Technology, Schools of [2]Chemical Engineering and [3]Mechanical Engineering, The University of Adelaide, SA 5005, Australia

Dong, X., Nathan, G.J., Sun, Z., Gu, D., Ashman, P.J., Alwahabi1, Z. and Dally, B. (2015) Influence of simulated solar radiation on the soot volume fraction in laminar sooty flames. In *10th Asia-Pacific Conference on Combustion, ASPACC 2015,* Beijing, China, July 19-22 2015, 6 pgs.

APPENDIX C

GLOBAL CHARACTERISTICS OF HYDROGEN-HYDROCARBON BLENDED FUELS TURBULENT DIFFUSION FLAMES

Xue Dong[1]*, Peter J. Ashman[1], Graham J. Nathan[2]

Centre for Energy Technology, Schools of [1]Chemical Engineering & [2]Mechanical Engineering,
The University of Adelaide, Adelaide, South Australia, SA 5000, Australia

Dong, X., Ashman, P.J. and Nathan, G.J. (2013) Global characteristics of hydrogen-hydrocarbon blended fuels turbulent diffusion flames. In M. Zhu, Y. Ma, Y. Yu, H. Vuthaluru, Z. Zhang and D. Zhang (eds.) *Proceedings of the Australian Combustion Symposium*, Perth, WA, November 6-8, 2013, pp. 267-270.